technische universität
dortmund

Optical Excitation and Detection of High-Frequency Coherent Phonons and Magnons

Dissertation

zur Erlangung des akademischen Grades

Doktor der Naturwissenshaften

(Dr.rer.nat.)

vorgelegt

der Fakultät Physik

der Technischen Universität Dortmund

von

Michal Kobecki

Dortmund, 2022

Datum der Einreichung: Dortmund, 9. August 2022

Datum der Disputation: Dortmund, 20. Oktober 2022

Prüfungskommision:

Prof. Dr. Manfred Bayer

Prof. Dr. Mirko Cinchetti

Prof. Dr. Heinrich Päs

Dr. Gerald Schmidt

Abstract

The goal of this work is to obtain better control over all-optical excitation and detection of high-frequency collective excitations, in particular - phonons and magnons. Phonons- a collective movement of atoms in the lattice, and magnons- excitations of a spin system in magnetically ordered materials, recently became the prospective alternative to electrons in quantum computing or in general, information technology. In the scope of this thesis, we present a novel approach to the resonant excitation of fundamental magnon mode in a thin ferromagnetic film of Iron-Gallium alloy, as well as enhanced detection sensitivity of propagating coherent phonon wave packet exploiting giant photo-elasticity of exciton-polaritons in GaAs/AlAs superlattice. Additionally, a possible way to miniaturize the all-optical set-ups for manipulation of collective excitations is proposed by implementing a passively mode-locked semiconductor laser diode.

The measurements focused on increasing the detection sensitivity of coherent phonons were done in the time domain with a standard pump-probe set-up with a mechanical delay line. The coherent phonon wave packet was generated in the Al film deposited at the back of the sample and then it propagated towards the superlattice at the front. The probe beam energy was tailored to match the exciton resonance of the superlattice and the Time Domain Brillouin Signal was obtained revealing giant photo-elasticity of exciton-polaritons. The signals show three orders of magnitude increase in detection sensitivity compared to standard probing away from the resonance. Obtained results pave the way for the quantum sensitivity of coherent phonon detection.

Resonant excitation and detection of the fundamental magnon mode in the ferromagnetic film were performed by the Asynchronous Optical Sampling method. The sample was placed in the external magnetic field at room temperature. It is shown that by tuning the magnetic field and matching the magnon frequency with the 10GHz excitation repetition rate of the laser we can obtain a 12-fold enhancement of magnetization precession amplitude detected by the magneto-optical Kerr effect. The demonstrated principle can be exploited in various nano-devices operating at GHz frequency ranges.

Finally, as proof of the principle, a passively mode-locked semiconductor laser diode is used to conduct pump-probe experiments on exciting and detecting phonon echo in the thin aluminum film at room temperature. We hope it is the first step toward out-of-lab applications of all-optical pump-probe set-ups.

Ziel dieser Arbeit ist es, eine bessere Kontrolle über die rein optische Anregung und den Nachweis von hochfrequenten kollektiven Anregungen, insbesondere Phononen und Magnonen, zu erlangen. Phononen - eine kollektive Bewegung von Atomen im Kristallgitter - und Magnonen - Anregungen eines Spinsystems in magnetisch geordneten Materialien - sind in letzter Zeit zu einer vielversprechenden Alternative zu Elektronen im Quantencomputing oder allgemeiner in der Informatatik/Informationsverarbeitung geworden. Im Rahmen dieser Arbeit wird eine neuartiger Ansatz zur resonanten Anregung der fundamentalen Magnon-Mode in einem dünnen ferromagnetischen Film aus einer Eisen-Gallium-Legierung, sowie eine verbesserte Nachweisempfindlichkeit von sich ausbreitenden kohärenten Phononenwellenpaketen unter Ausnutzung der gigantischen Photoelastizität von Exziton-Polaritonen im GaAs/AlAs-Übergitter, präsentiert. Darüber hinaus wird eine Möglichkeit zur Miniaturisierung rein optischer Aufbauten zur Manipulation kollektiver Anregungen durch den Einsatz einer passiv modengekoppelten Halbleiterlaserdiode vorgestellt.

Die zeitaufgelösten Messungen, zur Erhöhung der Nachweisempfindlichkeit für kohärente Phononen, wurden mit einem Standard-Pump-Probe-Aufbau mit einer mechanischen Verzögerungsstrecke durchgeführtDas kohärente Phononenwellenpaket wurde in der Al-Schicht auf der Rückseite der Probe erzeugt und breitete sich dann in Richtung des Übergitters auf der Vorderseite aus. Die Energie des Abtaststrahls (Probe) wurde auf die Exzitonenresonanz des Übergitters abgestimmt. Das erhaltene Time Domain Brillouin Signal wurde in Hinblick auf die gigantische Photoelastizität der Exziton-Polaritonen untersucht. (oder: Das erhaltene Time Domain Brillouin Signal zeigt die gigantische Photoelastizität der Exziton-Polaritonen.) Die Signale zeigen eine um drei Größenordnungen gesteigerte Nachweisempfindlichkeit im Vergleich zu Standarduntersuchungen abseits der Exzitonresonanz. Die erzielten Ergebnisse ebnen den Weg für eine Quantengenaue Empfindlichkeit der kohärenten Phononendetektion.

Die resonante Anregung sowie der Nachweis der fundamentalen Magnon-Mode im ferromagnetischen Film, wurde mit der Methode der asynchronen optischen Abtastung durchgeführt. Die Probe wurde bei Raumtemperatur in ein äußeres Magnetfeld gebracht. Es wird gezeigt, dass durch eine Abstimmung des Magnetfelds und eine Anpassung der Magnonenfrequenz an die 10-GHz-Anregungswiederholrate des Lasers, eine 12-fache Steigerung der Amplitude der Magnetisierungspräzession erreicht werden kann. Dies wird durch den magneto-optischen Kerr-Effekt nachgewiesen. Das demonstrierte Prinzip hat ein Anwednungspotential für verschiedenen, im GHz-Frequenzbereich arbeitende, Nanobauteile.

Als Machbarkeitsdemonstration wurde mittels einer passiv modengekoppelten Halbleiterlaserdiode, Pump-Probe-Experimente zur Anregung und zum Nachweis von Phononenechos in dünnen Aluminiumschichten bei Raumtemperatur durchgeführt. Dies könnte der erste Schritt in Richtung einer Realisierung rein optischer Pump-Probe-Aufbauten außerhalb des Laborsmaßstabs sein.

Contents

1

Introduction

The rapid expansion of information technology and its growing importance has driven constant interest in the miniaturization of computing devices and increased processing speeds with reduced energy consumption. Currently, we are at the limit of compactness and efficiency of the electron-based structures, this is why new fields like quantum computing are emerging and alternatives to the electrons are sought.

Prospective candidates for the role of energy and information carriers are phonons and magnons – collective excitations of the crystal lattice and magnetic order respectively. The concept of quasi-particles and collective excitations was proposed by Lev Landau in 1930. Unlike electrons and photons, their scientific discoveries didn't immediately find broad applications in information technology within the last century and only lately efforts are taken to obtain control over collective excitations in nano-scale and the GHz and THz frequency regimes, comparable in size and speed to modern electronics or nano-scale quantum devices. Their wave nature may prove useful as an alternative approach to computing without Ohmic losses and logic circuits based on nonlinear effects and wave interference, potentially operating with a significantly smaller footprint than their electronic counterparts.

The concept of phonons dates back to 1932 when I. Tamm proposed it for the first time. It is a collective movement of atoms or particles in elastically arranged condensed matter. It owes its name to a Greek word – '*phonē* 'meaning voice or sound because low-frequency phonons between 20Hz and 20kHz are essentially vibrations of the medium that our ear can detect. The electromagnetic acoustic transducers can provide phonons in the MHz regime. To achieve excitation of the coherent acoustic phonon wave packet with the frequencies in GHz regime and nano-meter wavelengths requires a source of excitation with specific characteristics. It has to provide the localization of the excitation in space and time. The development of ultrafast pulsed lasers made it possible to exploit the sub-picosecond light pulses for this purpose (*1, 2*). Localization is achieved spatially by a laser spot area and the energy deposition length of the material used as a source of the coherent phonon wave packet. Temporally it is limited by the duration of a laser pulse and the time of photo-acoustic conversion. In metal transducers, it is possible to excite coherent phonon wave packets in a form of the strain pulse with frequencies in the sub-THz regime, with picosecond durations and nanometer wavelengths (*3*). This size is comparable with the current size of nano-quantum devices and frequencies in the range of modern data transmission and processing (*4*). Effective excitation and high sensitivity detection of phonons as well as controlling their interaction with

electrons and photons may pave the way for new applications in a wide range of technologies like nano-electronics, energy harvesting, nano-mechanics, imaging, and quantum technologies.

Magnons similarly to phonons were predicted almost one hundred years ago, by F. Bloch as a collective excitation of electrons' spin system. Exploiting the magnetic order of solids has a long history preceding even understanding of its quantum nature and it already has found many important applications in our lives, starting from compasses and ending with commonly used hard disc drives (HDD). This encouraged further studies on magnetic order and its collective excitations- magnons, which can be consider as a collective, precessional motion of magnetic moments driven by exchange interaction. Similar to electric currents, currents based on magnons can be used to process and transport information. In order to be competitive, they have to have frequencies comparable with modern data transmission and processing as well as wavelengths in the nanoscale regime. Exciting effectively magnetization dynamics in GHz and THz frequency range and high precession amplitude is a challenge for current studies. Manipulation of the magnetic order can be obtained by different means, the common way of magnon excitation used to be a monochromatic microwave with ferromagnetic resonance matching frequency (*5*). Due to the limitations of methods exploiting electronic current for the generation of magnons, an alternative method was developed- excitation by ultra-short laser pulses for control of the magnetization(*6-10*). Spatial-temporal localization provided by laser pulse allows broadband excitation of magnons in terms of frequency and wave vectors. High repetition rate lasers on the other hand may be used for resonant excitation of spectrally narrow magnons with a high amplitude of precession. Since the discovery of ultrafast demagnetization at the end of the XXth century by a single laser pulse, the optical modulation of magnetic order became a topic of interest and competitive technique in the fields of magnonics and spintronics, with the prospect of finding applications in information technology or quantum computation.

The optical manipulation and detection of collective excitations require advanced laser systems with parameters, up to recently – reserved only for complex and rather large devices. It is quite a serious obstacle in the way to miniaturization and implementation of these techniques, however lately the development in the semiconductor laser field has allowed the designing of compact laser diodes with characteristics comparable to their bulky and complex counterparts (*11, 12*). The concept of semiconductor lasers dates back to the 1960', but initially, it was operational only in cryogenic temperatures and it took a long time to become efficient and functional in room temperatures. However, achieved compactness, efficiency and price made it the most popular type of laser ever produced, finding

applications in numerous fields like sensing, medicine, and information technology. The stable pulsed operation remains a challenge for the community, but up-to-date passively mode-locked laser diodes (MLLD) provide already pulses with a duration below 1ps, high repetition rates in GHz regime (*13*), and average powers up to 200mW (*14*) as well as a wide range of wavelengths, which is sufficient for the generation and detection collective excitations. It makes it a promising tool for implementing optical modulation of collective excitations on a micro-scale and possibly further on-chip integration.

In the scope of this thesis, I present pump-probe optical excitation and detection of coherent phonons and magnons with high frequencies in the sub-THz regime and possible direction for future miniaturization of these techniques by implementing semiconductor passively mode-locked laser diode (MLLD). In Chapter 2 a technical introduction to the pump-probe technique is given as well as theoretical background on optical excitation and detection of phonons and magnons. Chapters 3, 4, and 5 contain. original work. Chapter 3, on exploiting giant photo-elasticity of exciton-polariton resonance in a short period GaAs/AlAs superlattice (SL) for the detection of high-frequency phonons with quantum sensitivity. In Chapter 4 a proposal of resonant excitation of narrow-line, high-frequency magnons in Ga-Fe ferromagnetic alloy in the external magnetic field is presented. In Chapter 5 as proof of principle, a semiconductor laser diode in a pump-probe set up for excitation and detection of the phonon echo in Al thin film was implemented. Conclusions of the main results and a possible outlook are given in Chapter 6.

2

Technical and theoretical background

The main goal of the experiments conducted in the scope of this thesis is all-optical excitation and time-resolved detection of high-frequency collective excitations, namely phonons and magnons. Ultra-fast modulation and detection of system dynamics can be done optically by the pump-probe technique. Typically, a pulsed laser source is used with a pulse duration below 1 picosecond and a repetition rate ranging from kHz to GHz depending on the goal of the studies. The beam is split into two paths, called pump and probe. The pump pulses are meant to disturb the system out of equilibrium providing excitation of the system. The role of the probe is to detect induced changes in optical properties of the studied system by measuring changes in transmission, reflectivity, or the polarization of light. By changing the time interval between pump and probe, one can scan between arrival of the pump pulses and reconstruct the temporal evolution of the signal, providing information about the dynamic response of the system(*15*). This technique allows one to characterize collective excitations behaviour in the GHz range with sub-picosecond time resolution. In this chapter, the technical background on the all-optical pump-probe technique for excitation and detection of phonons and magnons is presented as well as a general description of the physics behind it.

2.1 Pump-probe technique with a mechanical delay line and a Lock-in Amplifier detection

The scheme of the classical pump-probe setup is presented in Fig.2.1. An important aspect of the experimental setup is a realization of the delay of the probe with respect to the pump and a detection of a weakly modulated signal. In traditional pump-probe setups, a change in the time interval between pump and probe is done by a mechanical delay line. The range of the delay line's displacement defines the measurement's time window and its increment determines the time resolution. With the time delay $\Delta t = 2d/c$, where c is the speed of light and d is the displacement of the delay line, we get that sub-picosecond resolution available for a change in the optical path below 300 μm, which is not a challenge for modern mechanical delay lines. To retrieve the dynamics of the studied system we detect changes in the probe beam. Signal modulation in the experiments performed in the scope of this thesis is between 10^{-2} and 10^{-7}. In order to achieve a satisfactory signal-to-noise ratio, certain steps have to be taken. Firstly, the mechanical delay sets the pump at a certain time before probe pulse arrival, and averaged acquisition of the signal is done. Subsequently, the delay line changes the time interval and the next averaged signal

point is taken. Alternatively, the movement of a delay line can be continuous and averaging taken over the whole time window. In such a case, the time resolution is set by the integration time and velocity of a delay line. Often averaging is not enough for the detection of the signals below the initial noise level coming from the experimental set-up and the environment. To decrease the noise level of the laser, a reference signal can be measured and a differential signal is taken eliminating the fluctuations of the light source. To decrease the noise of the environment, Lock-in amplification is introduced, which can extract signal changes down to a level significantly smaller than the initial noise level. It is done by frequency modulation of the signal. The pump beam is modulated with a set frequency (higher than environmental frequencies, and lower than laser repetition rate and frequencies of the phenomena under study). Usually, it is done with the mechanical chopper or acousto-optic modulator. Afterward received signal is demodulated- filtered and amplified by Lock-in Amplifier. All noise that is not carried with the modulated frequency gets filtered out. This technique together with a reference beam and multiple averaging allows measuring very subtle changes in the probe signal, decreasing the noise below 10^{-6} level.

Fig. 2.1 Working principle of mechanically delayed pump-probe setup with a lock-in amplifier.

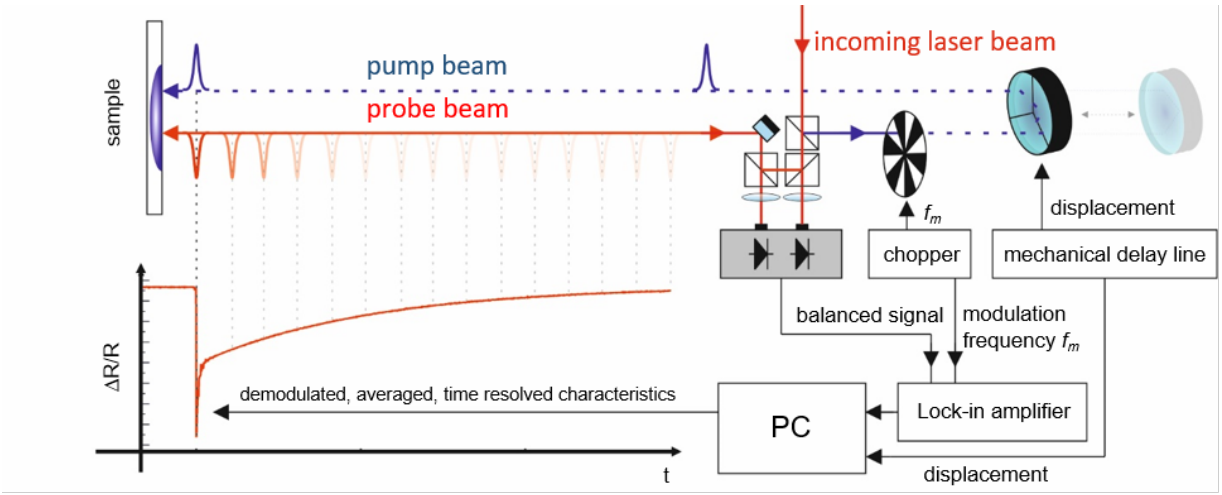

Despite all the efforts to maintain a high signal-to-noise ratio, the mechanical aspect of moving parts generates certain challenges in maintaining the alignment and stability of such a setup. Moreover, the time of such signal acquisition which is depending on a number of averages, the time resolution, and range, can get extremely long, which, apart from its inconvenience, can result in losing alignment, or change in environmental conditions. In recent years nouvelle technique of pump-probe measurements was introduced to meet these challenges. It is called Asynchronous Optical Sampling (ASOPS)(*16*) .

2.2 Asynchronous Optical Sampling (ASOPS) technique

ASOPS method was developed at the beginning of the XXI century (*16*) and successfully implemented in the field of time-resolved measurements(*17-19*). Its main advantage is that it needs no moving parts and also increases the speed of measurements. Measuring reflectivity changes down to 10^{-6} requires only a few seconds(*20*). It is realized in a way that two laser sources are synchronized with each other and differ slightly in the repetition rate. One is referred to as the master and its repetition rate f_m remains constant, the other one is the slave and its repetition rate f_s is adjusted by small changes of resonator length realized in a closed feedback loop. For stability of the measurement system, one shall use the probe beam as the master, while the pump is serving as a slave. Synchronization of the lasers can be done both optically obtained with nonlinear optical photo-diode triggered when master and slave pulses overlap or electrically with independent feedback loops for each resonator(*18, 21*). The change of the slave laser frequency results in a fixed time step ΔT, scanning between pump and probe pulse arrival, shown graphically in Fig.2.2. The number of slave pulses arriving in between arrivals of the master pulses is determined by the ratio between master frequency and the offset frequency f_o:

$$N = \frac{f_m}{f_o}$$

Where $f_o = |f_m - f_s|$. Therefore, the time step is specified by the time between master pulses τ_m divided by the number of pulses N between them:

$$\Delta T = \tau_m / N = \frac{1}{f_m} \cdot \frac{f_o}{f_m} = \frac{f_o}{f_m^2}$$

The whole operation is happening in corresponding real-life time between a set of pulses resulting in a trigger event when they overlap. The time τ_c is defined as the number of probe master pulses we need to scan the full-time range, multiplied by the time duration between them. In case we use the probe as a master laser ($f_m = f_{probe}$) :

$$\tau_c = N \cdot \tau_m = \frac{f_m}{f_o} \cdot \frac{1}{f_m} = \frac{1}{f_o}$$

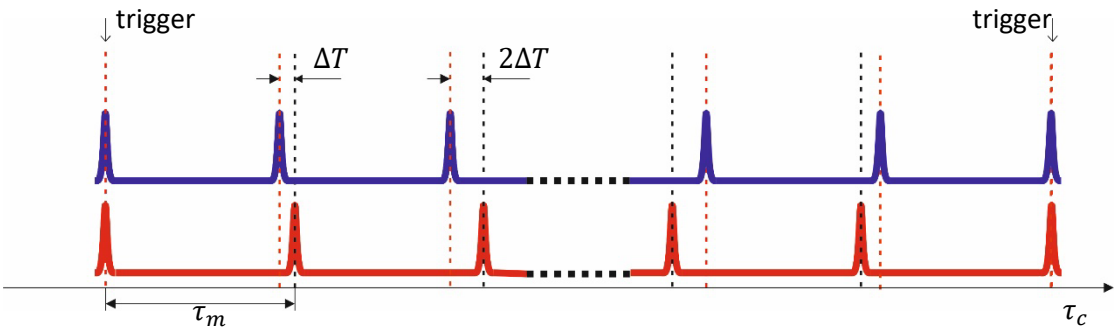

Fig. 2.2 ASOPS operation principle. Probe signal marked in red (bottom one) being master and pump signal serving as slave marked in blue (top one). A small difference in frequency being offset frequency f_o provides a shift between two signals ΔT.

2.2.1 Variant frequency ASOPS system.

In the scope of this thesis, as already mentioned, we study high-frequency physical phenomena with frequencies in the GHz range. For resonant excitation of magnons, a 10 GHz laser is used. For the probe, however, it is convenient to use a 1GHz frequency, which corresponds with the bandwidth available for conventional electronics used in the set-up. Although we use two lasers with different frequencies, the principle of work remains the same. Offset frequency f_o, a number of points between master laser pulses N and time step ΔT values hold. It is so, because they are related with only one laser – master laser, which in our case is a probe of 1GHz (see Fig.2.3). The real-life corresponding time is not changing as well. One thing, that is changing is the fact that $f_m = f_{probe}$, since the pump comes ten times more often, the overlap of two pulses will happen also ten times more often (τ_t). During one τ_c we will observe 10 periods of the pump. Further, they may be folded and used for averaging.

For the set-up with 1GHz probe master laser, 10GHz pump slave laser, and 2kHz offset frequency we end up with the following characteristics:

$$N = \frac{f_m}{f_o} = 5 \cdot 10^5$$

$$\Delta T = \tau_m / N = \frac{1}{f_m} \cdot \frac{f_o}{f_m} = \frac{f_o}{f_m^2} = \frac{2kHz}{1GHz \cdot 1GHz} = 2\ fs$$

$$\tau_{pump} = 100ps \quad \tau_m = 1\ ns$$

$$\tau_t = \frac{\tau_c}{10} = N \cdot \frac{\tau_m}{10} = \frac{500\mu s}{10} = 50\ \mu s$$

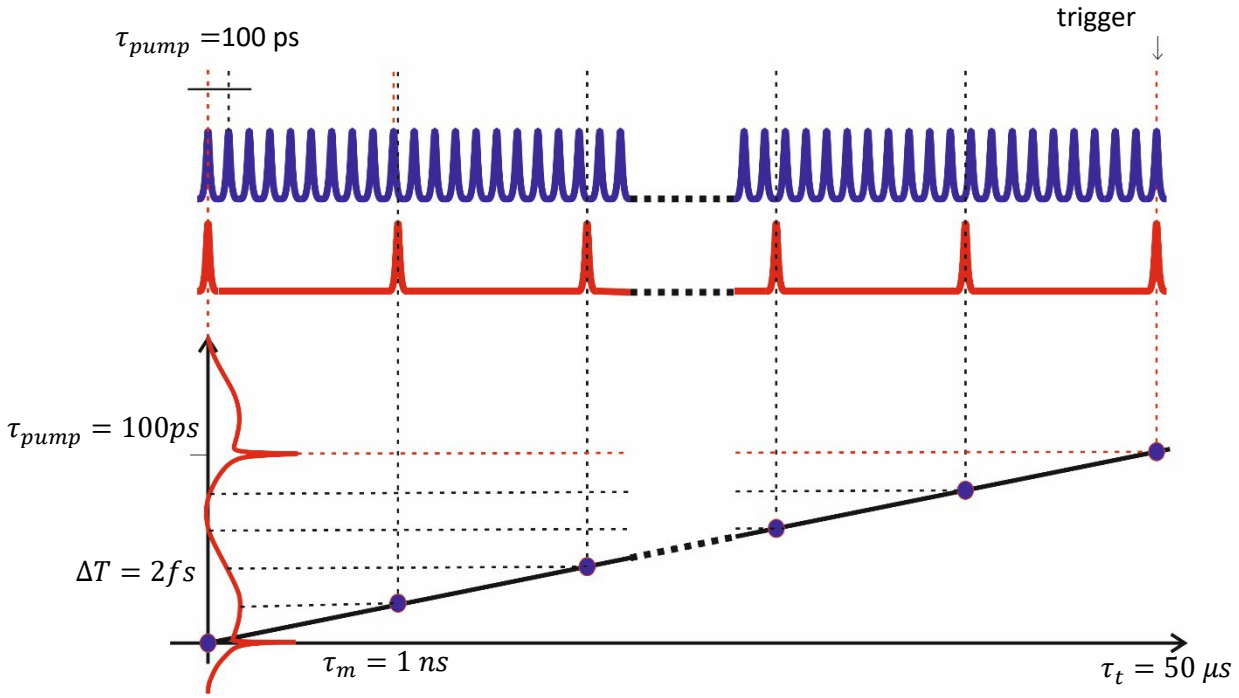

Fig. 2.3 Variant frequency ASOPS working principle. Between one probe pulse, we observe ten pump pulses. Though it would be beneficial to use all of them, it would significantly increase the costs and complexity of the detection part of the set-up. Nevertheless, during τ_c =500μs real-life time corresponding measurement time for probe master laser, we can observe 10 periods τ_t =50μs of the pump and fold it for further averaging.

The time of measurements depends on a number of averages necessary to obtain the desired signal-to-noise ratio and offset frequency which sets a single acquisition time τ_c. The time step of the measurements is also determined by the ASOPS offset frequency, however other parameters like duration of the pulse or jitter of the time base related to the bandwidth of detection electronics, including the diode are dominant in setting effective time resolution which is usually in the sub-picosecond range. In set-up exploited in the scope of this thesis, temporal resolution was at 50 fs level.

2.3 Ultrafast optical excitation of high frequency coherent acoustic phonons in a metallic film

One of the most popular methods of ultra-short coherent acoustic phonon wave packet generation is based on the absorption of a sub-picosecond laser pulse by a metal transducer. This technique was developed in the '80s in the group of H. J. Maris at Brown University (*1, 22, 23*). Further development of the excitation geometries and material properties as well as an understanding of physical mechanisms standing behind the generation of coherent phonon wave packets allowed to control of their parameters and implementation of the technique in many fields like biology, medicine, and solid-state physics. The laser pulse with a duration significantly shorter than the time of the energy deposition processes responsible for launching the coherent phonon wave packet arrives at the surface of the metal transducer. The gradient of thermal stress in the film launches a picosecond acoustic pulse, which is propagating away from the surface. Let us consider a metal film with reflectivity R hit by the laser pulse with energy equal to Q, deposited on the area A of the laser spot. Then the energy of the pulse is transferred via electrons to the lattice and its deposition $W(z)$ per unit volume will be distributed in z direction normal to the surface in the following way:

$$W(z) = C\Delta T(z) = \frac{S}{\zeta}\exp\left(-\frac{z}{\zeta}\right) \tag{2.1}$$

where C is specific heat per unit volume, $S = \frac{(1-R)Q}{A}$ and ζ is penetration depth. If the excited area *A* has a diameter significantly larger than penetration depth ζ, we can assume that the rapid thermalization leads to the thermal stress $\sigma_{thermal}$, dependent only on the z-axis:

$$\sigma_{thermal} = -3B\beta\Delta T(z) \tag{2.2}$$

where B is the bulk modulus and β linear expansion coefficient of the medium. Since we assume the motion only in the z-direction, elasticity equations connecting displacementu_z, stress σ_z and strain η_z take the following form:

$$\sigma_z = 3\frac{1-\upsilon}{1+\upsilon}B\eta_z - 3B\beta\Delta T(z) \tag{2.3}$$

$$\rho\frac{\delta^2 u_z}{dt^2} = \frac{\delta\sigma_z}{dz} = \left(3\frac{1-\upsilon}{1+\upsilon}B\eta_z - 3B\beta\Delta T(z)\right)\frac{\delta}{dz} \tag{2.4}$$

where υ is Poisson's ratio. Initial conditions consider zero strain everywhere ($\eta_z = 0$) and the stress vanishing at the transducer surface ($\sigma(0) = 0$). The elasticity equations provide two solutions, one being static strain at the surface of the medium and the second one being the strain pulse propagating away from the initially heated region at the surface and it is defined as:

$$\eta(z,t) = \eta_0 \cdot \exp\left(-\frac{|z-vt|}{\zeta}\right) sgn(z-vt) \tag{2.5}$$

$$\eta_0 = \frac{3SB\beta}{2C\zeta v^2} \tag{2.6}$$

It is localized at $z = vt$ and propagates with the speed of sound $v^2 = 3\frac{1-\upsilon}{1+\upsilon}\frac{B}{\rho}$ where ρ is density. The instantaneous energy transfer $W(z)$ defined in Eq.2.1 as well as the assumption that temperature distribution has a simple exponential shape, dependent only on the penetration depth of light in the material is a simplified interpretation. To describe the process of coherent phonons wave packet generation more accurately, one needs to take into account several relaxation processes which lead to more complex temperature evolution responsible for a final spatial-temporal profile of the strain pulse. The energy deposition dynamics and transient distribution of temperature of the lattice T_l are governed by thermal and electron diffusion and can be described by a two-temperature model. We consider two reservoirs of the energy – electrons and the lattice. The temporal and spatial evolution of electron temperature T_e and lattice temperature T_l can be obtained from two coupled partial differential equations:

$$C_e\frac{\delta T_e}{\delta t} = \frac{\delta}{\delta z}\left(\kappa\frac{\delta T_e}{\delta z}\right) - g(T_e - T_l) + \frac{1}{\zeta}S(t)\exp\left(-\frac{z}{\zeta}\right) \tag{2.7}$$

$$C_l\frac{\delta T_l}{\delta t} = g(T_e - T_l) \tag{2.8}$$

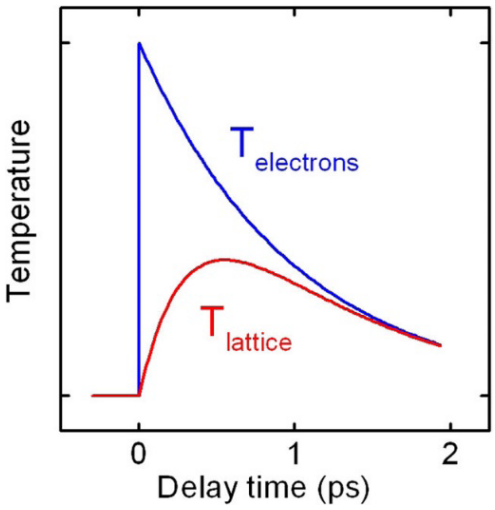

Fig. 2.4 The two-temperature model showing typical time evolution of electron and lattice temperature in metals like Al, Ni, Cr, Cu, Au. The arrival of laser pulse at time t=0 is followed by rapid increase of electron temperature followed by the lattice temperature. After few ps temperatures of both reservoirs equalize. (1)

where C_e and C_l are the heat capacity per unit volume of the electron reservoir and the lattice respectively, κ is thermal conductivity and g is the electron-phonon coupling parameter. The laser pulse, due to the high frequency of light, is not heating the lattice directly, it couples however with the electrons via deposited energy of the pump pulse described by the term $\frac{1}{\zeta}S(t)\exp\left(-\frac{z}{\zeta}\right)$. After the arrival of an ultra-short laser pulse, the relatively low heat capacity electrons initially absorb photon energy. It is due to the electron heat capacity being two orders of magnitude smaller than the heat capacity of the lattice $C_e{\sim}0.01C_l$ (*24*). This gives the fast rise of the electron temperature that $T_e \gg T_l$. The exemplary temporal evolution of T_e and T_l is presented in Fig.2.4.

As electrons relax the energy is transferred to the lattice, until eventually $T_e = T_l$. The time of the energy relaxation for the electrons is $\tau_e = C_e/g$ (which for metals is approx. ~1 ps (*24*)). The non-equilibrium electrons diffuse and give away their energy to the lattice at the distance of $z_e = (\kappa/g)^{1/2}$. In materials with high electron-phonon coupling constant g ($\sim 200 - 500 \cdot 10^{15}\ \mathrm{Wm^{-3}K^{-1}}$) like Cr or Ni, electrons give away the energy to the lattice within short distances comparable with the absorption length of light $\zeta{\sim}5\ nm - 20\ nm$ (*3, 25*), however in some cases, they have a significant contribution to the strain profile. In noble metals or aluminium with a low electron-phonon coupling constant ($\sim 20 - 60 \cdot 10^{15}\ \mathrm{Wm^{-3}K^{-1}}$) the electrons can travel to distances of ~100 nm, which is significantly further than the absorption length of light (*25*). This gives a rise to a temperature gradient distributed over a larger distance, which results in broadening and smoothing of the pulse leaving the excitation area. Once electrons have deposited their energy into the lattice, lattice temperature continues to change due to thermal diffusion. This happens within time $\tau_{th} = \zeta^2/D_{th}$ (where $D_{th} = \kappa/C_l$ is thermal diffusivity) and distance $z_{th} = \left(\frac{D_{th}\zeta}{\nu}\right)^{1/2}$. If the time is larger than the time of the longitudinal

acoustic propagation time across penetration depth $\tau_{th} = \zeta/v$, and the diffusion distance is larger than ζ, then it has to be taken into account. Non-equilibrium electrons and thermal diffusion have an impact on the final special-temporal shape of the strain pulse and therefore, its frequency spectrum is determined by the above-discussed parameters varying for different metals. In the case of aluminum used for picosecond strain generation in the scope of this thesis, the electron diffusion length is larger and diffusion time is shorter than the electron-phonon coupling mechanism, while thermal diffusion is slower and takes place within the absorption length of light, giving less contribution to the final shape of the generated strain pulse (see Fig.2.5)(*25*). Eventually, we get a coherent phonon wave packet in the form of a strain pulse propagating away from the surface which shape can be approximated by including the electron diffusion mechanism into Eq. 2.5 :

$$\eta(z,t) = \eta_0 \frac{\zeta}{z_e} \cdot \exp\left(-\frac{|z-vt|}{z_e}\right) sgn(z-vt) \tag{2.9}$$

The strain pulse is smoothed and broadened by the factor of $\frac{z_e}{\zeta}$. Therefore, in the frequency domain which can be obtained from the Fourier transform of temporal shape, the spectrum shifts towards lower frequencies. Detailed qualitative and quantitative influences of both mechanisms in various metals can be found in Ref (*2, 3, 24, 25*).

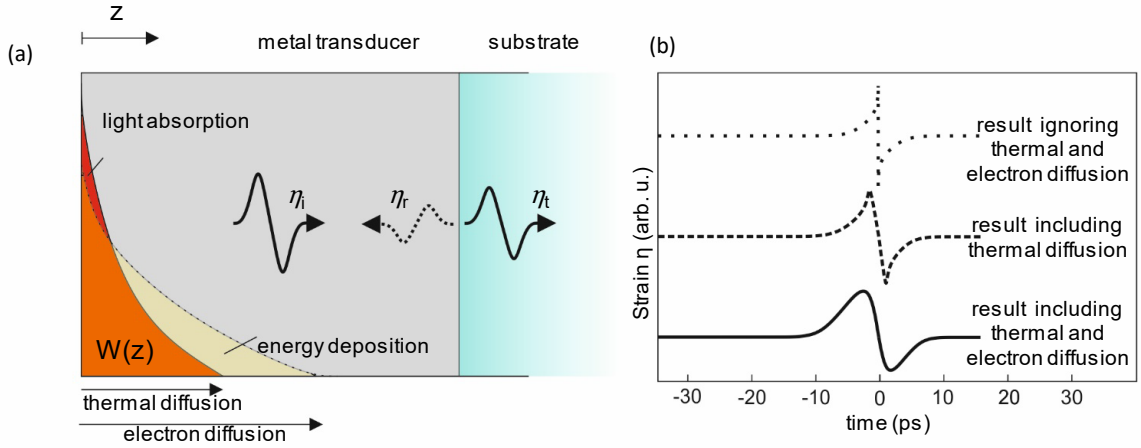

Fig. 2.5 (a) Schematic of the strain pulse generation process: a laser pulse is absorbed at the surface (red area) by the electrons, the energy deposition is altered by the electron diffusion (yellow area) and less influenced by thermal diffusion. Then a bipolar strain pulse (η_i) leaves the surface region and propagates to the interface with the substrate of the sample, where part of it gets reflected (η_r) and part is transmitted further (η_t). (b) strain pulse profile simulation results, top: according to Eq.2.5, middle: result including thermal diffusion, and bottom: result taking into consideration both thermal and electron diffusion.

After propagation through the transducer, at the interface with the substrate, the pulse is partly reflected and partly transmitted, according to the reflection and transmission coefficients r and t:

$$r = \frac{Z_{substrate} - Z_{transducer}}{Z_{substrate} + Z_{transducer}}, \qquad t = \frac{2 \cdot Z_{substrate}}{Z_{substrate} + Z_{transducer}},$$

Where Z is the acoustic impedance of the material. It is beneficial to choose materials with a similar acoustic impedance in order to maximize the amplitude of the injected acoustic pulse. Finally, the pulse propagates into the sample with the sound velocity dependent on the material.

2.4 Detection of GHz-frequency phonons

In the scope of this thesis, the pump-probe technique was implemented for the generation and detection of coherent phonons. Various signals can be obtained depending on the material and the probe wavelength used in the experiment. If the probe light doesn't penetrate the sample, one can study phonon-induced changes in reflectivity ΔR of the material on the surface and directly below it, within absorption depth. The reflectivity is described as follows:

$$\Delta R(t) = \int_0^\infty f(z)\Delta\varepsilon(\eta)dz \tag{2.10}$$

where $f(z)$ is the sensitivity function that determines overlap with the strain induced changes in the dielectric permittivity $\Delta\varepsilon(\eta)$ that contributes to the change of the reflectivity and depends on the material and probe beam interaction (*22*). Due to the short distance of the detection of the phonon wave packet, it is possible to resolve a wide spectrum of the frequencies arriving at the surface of the transducer. In such way one can detect among others, the phonon echo of the coherent phonon wave packet in a form of the acoustic pulse previously launched at the surface. The way of generation and detection such acoustic pulse is presented in Fig.2.6a and the time resolved reflectivity change is presented in Fig.2.6b.

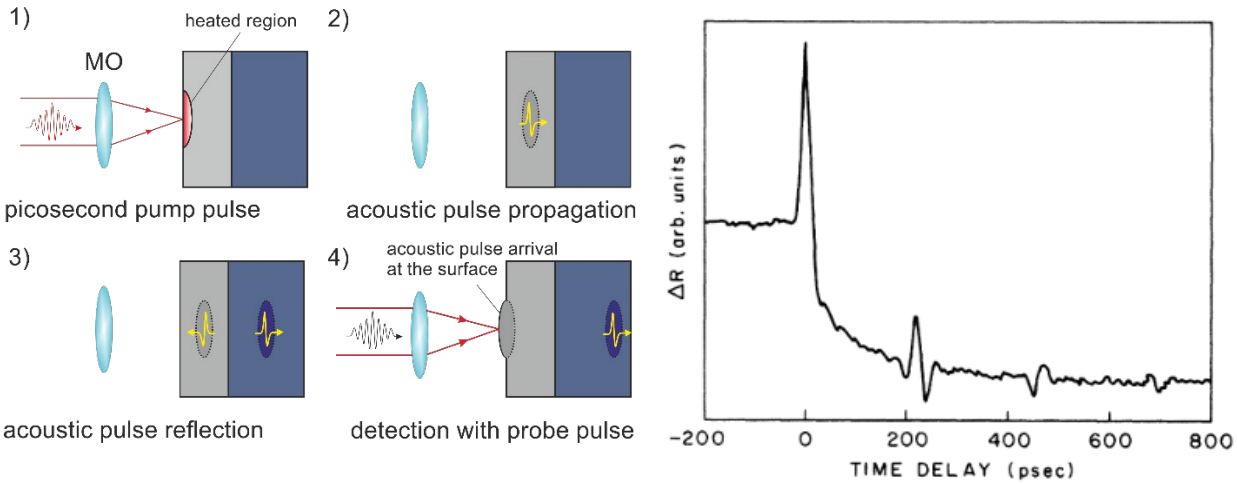

Fig. 2.6 Left: the example of the phonon echo experiment, right: phonon induced changes of surface reflectivity, one can see the pulse arrival at t=0 and phonon echoes detected at t=220, 440, 660ps (22).

For detection of high frequency propagating phonons in a transparent sample, in the scope of this thesis a technique called Time Domain Brillouin Scattering (TDBS) is used. The technique initially referred to as picosecond acoustic interferometry (*26, 27*) proved to be advantageous for studying the acoustic and optical properties of transparent materials by transient measurements. Detection is done by a probe laser pulse interaction with a part of the coherent phonon wave packet spectrum that fulfills the conservation law for photon-phonon interaction, that is the Brillouin scattering condition, which is $q = 2k$, where q is phonon vector and k is photon vector. Information about the propagating acoustic pulse is obtained by measuring transient relative changes in the intensity of the reflected probe beam - ΔR in the time domain (see Fig.2.7b). The probe pulse reflected from the surface interferes with the beam scattered from the propagating phonon wave packet (see Fig.2.7a). These beams interfere constructively or destructively depending on the position of the acoustic pulse, the phase difference changes linearly in time causing sinusoidal variations in the signal amplitude at a frequency called Brillouin frequency, which depends on the wavelength of the probe λ, refractive index n, and the speed of sound v in the medium: $f_B = \frac{2nv}{\lambda}$ (see Fig.2.7b).

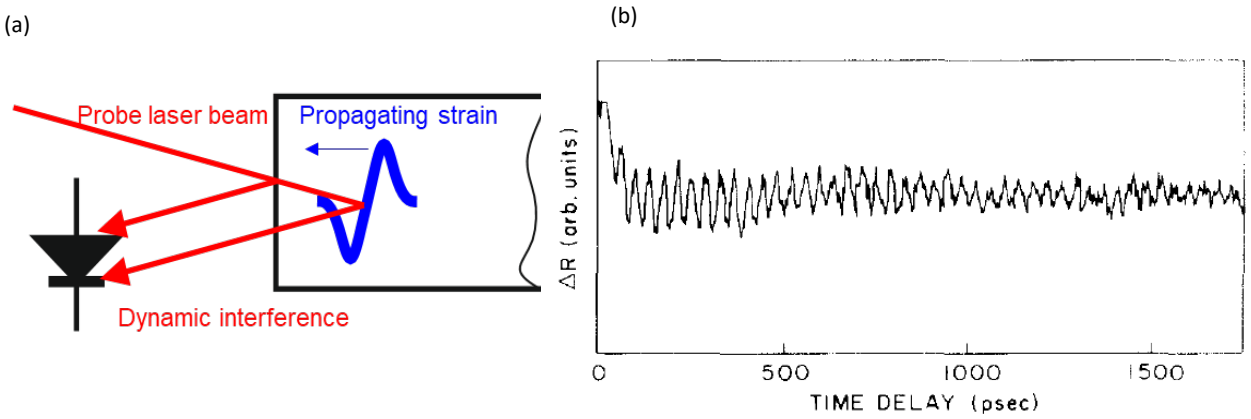

Fig. 2.7(a) the principle of Time Domain Brillouin Scattering, the laser beam reflected from the surface interferes with the beam scattered from the coherent phonon wave packet propagating inside the sample. (b) dynamical change of scattered light phase provides constructive and destructive interference resulting in a periodic signal with Brillouin frequency and amplitude depending photo-elastic parameter (24).

The reflectivity change happens due to a change in the optical parameters of the sample caused by propagating strain and is detected by the probe electromagnetic wave. The change in reflectivity ΔR, which governs the TDBS signal, can be described as follows:

$$\Delta R(t) = R \int_0^\infty \Delta\varepsilon(\eta) e^{2ik_1 z} dz \qquad (2.11)$$

Where R denotes the reflection coefficient at the interface between the environment and the sample and k_1 is a wave vector of the probe in the medium. The integral defines coupling between the phonon-induced changes in dielectric permittivity and the probe beam electromagnetic wave, which determines the sensitivity and therefore, intensity of the beam scattered from the propagating strain. In the simplest case when strain pulse in the linear regime is propagating through the low varying dispersive medium, $\Delta\varepsilon(\eta)$ can be defined as (*28*):

$$\Delta\varepsilon(\eta) = {\varepsilon_0}^2 p\eta(t,z) \tag{2.12}$$

Where p is a linear photo-elastic parameter. In the case of GaAs used in the scope of this thesis the photo-elastic parameter depends on the crystallographic direction and its value is $p < 1$ (*29*). In contrast to the surface detection due to the transient probing, we detect only a part of the frequency spectrum of the coherent phonon wave packet around f_B that couples with the probe beam.

Though the technique was developed initially to perform acoustic in-depth profiling and possible analysis of material acousto-optical properties (refractive index, sound velocity, or acoustic impedance), in the scope of this thesis a slightly reversed approach is taken. The parameters of the material are chosen in a way that provides a high sensitivity of phonon detection. In Chapter 3 experiments performed in GaAs/AlAs superlattice with the probe beam energy in the vicinity of an exciton resonance are presented, which provides an enhanced photo-elastic effect resulting in the increased sensitivity for detection of discrete numbers of high-frequency acoustic phonons propagating through the sample. In Chapter 5 an implementation of a semiconductor laser for excitation and detection of the phonon echo is presented.

2.5 Ultrafast optical excitation of high-frequency coherent magnons in a metallic film

Optically modulated heating can be used for generating magnons- collective excitations of magnetic order in magnetically ordered materials like ferromagnets. In homogeneously magnetized media we can define a macroscopic magnetic moment m_0. Since the magnetic moment of an atom is strongly related to the orbital motion of electrons, it contains an angular momentum L. The angular momentum is proportional to the magnetic moment. The constant of proportionality γ is called gyromagnetic ratio and the relation is defined as:

$$m_0 = \gamma L \tag{2.13}$$

The torque acting on a magnetic moment in external magnetic field B is

$$T = m_0 \times B \tag{2.14}$$

The change in angular momentum and change of magnetic moment in time in an external magnetic field is as follows:

$$\frac{dL}{dt} = \frac{d}{dt}\frac{m_0}{\gamma} = \gamma L \times B \tag{2.15}$$

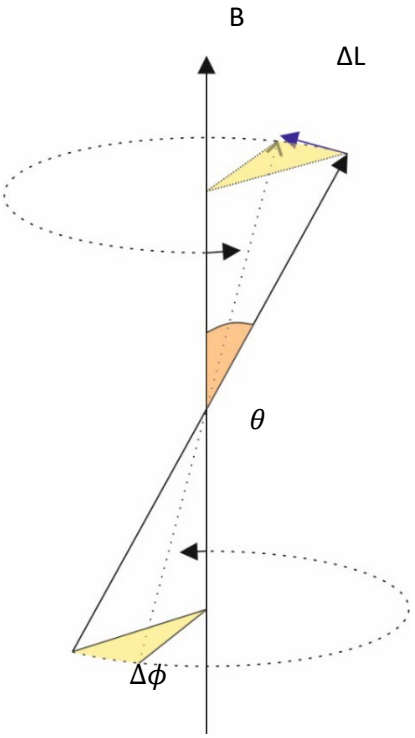

Fig. 2.8 Larmor precession

When we consider an infinitely small increment of t the angular momentum will change by ΔL, resulting in a change of angle equal to:

$$\Delta\phi = \frac{\Delta L}{Lsin\theta}, \tag{2.16}$$

by implementing Eq. 2.15 into Eq. 2.16 one gets:

$$\frac{d\phi}{dt} = \frac{1}{Lsin\theta}\frac{dL}{dt} = \frac{\gamma L \times B}{Lsin\theta} = \frac{\gamma LBsin\theta}{Lsin\theta} = |\gamma B|. \tag{2.17}$$

Since the change of angle over time is angular frequency one can write $\omega_L = |\gamma B|$. Where ω_L is called Larmor precession frequency, which is directly related to the strength of the external magnetic field and the gyromagnetic ratio of the system. It is however an isolated case and lossless approximation which is rarely a case in real systems. In the case

of complex systems like ferromagnetic nanostructures, modulation of magnetic order becomes a many body problem which is hard to deal with. Instead of many single magnetic moments we consider a collective normalized magnetization vector $m = M/M_0$ placed in effective magnetic field B_{eff} which takes into account all contributing factors, like crystallographic anisotropy, shape anisotropy, boundary conditions as well as an external magnetic field. In such a case by combining Eq. 2.9 and 2.10, the precession of the magnetization vector can be expressed as the following Landau-Lifshitz equation:

$$\frac{dm}{dt} = \gamma(m \times B_{eff}) \tag{2.18}$$

To fully describe the precessional motion of the magnetization towards the equilibrium in presence of a static external magnetic field one has to take into account the damping of the system. The trajectory of the magnetic precession with damping is presented in Fig.2.9. Mechanisms responsible for the damping include intrinsic spin-orbit coupling, two magnon scattering, eddy currents or material inhomogeneities (*30, 31*). Phenomenologically, the loss is introduced into the equation of motion as a component perpendicular to the external magnetic field and directed towards it. The equation of motion then takes the form of the Landau-Lifshitz-Gilbert equation:

$$\frac{dm}{dt} = \gamma(m \times B_{eff}) + \alpha\left(m \times \frac{dm}{dt}\right) \tag{2.19}$$

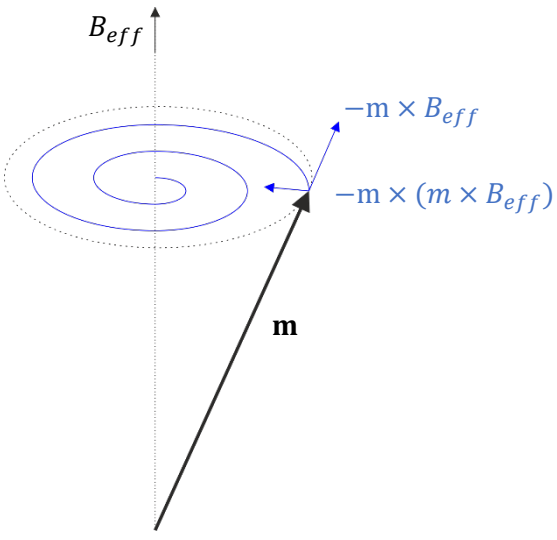

Fig. 2.9 Damped magnetization precession around effective magnetic field Beff

The damping term is governed by a phenomenological unitless Gilbert damping parameter α of the material. The effective magnetic field is defined as follows: $\mathrm{B_{eff}} = -\nabla_{\mathrm{m}} F_{\mathrm{M}}(\mathrm{m}, t)$, where the F_{M} is the normalized free energy density. The parameters contributing to the effective magnetic field B_{eff} apart of external magnetic field B_{ext} are sample dependent. In thin ferromagnetic films, the contributing parameters are magnetocrystalline and shape anisotropy. In Iron and some of its alloys, as FeGa studied in this thesis, due to its body-centered crystal structure (Fig.2.10a) and the spin-orbit interaction, magnetocrystalline anisotropy has three 4-fold symmetry axis along principal crystallographic directions, these axes for Iron are aligned with the easy axis of the body-centered magnetization, where the free energy density (Eq.2.20) has its minimum (Fig.2.10b). The energy density is a function of even powers of the m direction:

$$F_{cubic} = K_1\left(m_x^2 m_y^2 + m_z^2 m_y^2 + m_x^2 m_z^2\right) + K_2\left(m_x^2 m_y^2 m_z^2\right), \tag{2.20}$$

and its alternative form with azimuthal angle φ and polar angle θ:

$$F_{cubic} = \frac{1}{4}K_1(sin^2 2\theta + sin^4\theta sin^2 2\varphi) + \frac{1}{16}K_2(sin^2\,\theta + sin^4 2\theta sin^2 2\varphi) \tag{2.21}$$

In some materials or in thin films considered in the scope of this thesis, uniaxial anisotropy is present (*32, 33*). In thin films in plane uniaxial anisotropy is present and it is defined by uniaxial anisotropy constant K_u (*34*). This contributes to the overall crystallographic anisotropy of the free energy density, taking the form of a sum of cubic and uniaxial parts:

$$F_{an} = \frac{1}{4}K_1(sin^2 2\theta + sin^4\theta sin^2 2\varphi) + \frac{1}{16}K_2(sin^2\,\theta + sin^4 2\theta sin^2 2\varphi) + K_{u1}sin^2\,\varphi + K_{u2}sin^4\,\varphi \tag{2.22}$$

Additional contribution to free energy distribution comes from shape anisotropy originating from dipole-dipole interaction and in thin films can be defined as:

$$F_d = B_d m_z^2 \tag{2.23}$$

where $B_d = \frac{\mu_0 M_0}{2}$ is the scalar demagnetizing field.

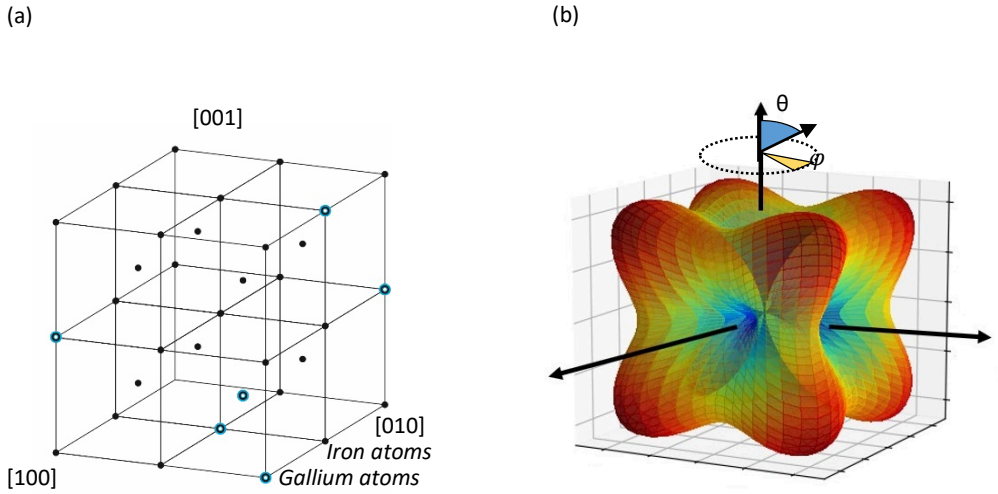

Fig. 2.10 (a) Crystallographic structure of GaFe alloy, (b) representation of cubic anisotropy free energy density distribution (35).

Considering together external magnetic field, cubic and uniaxial anisotropy as well as shape anisotropy one may define normalized free energy density in the following way (*35*):

$$F_M(m) = -(\mathrm{m} \cdot \mathrm{B}_{ext}) + B_d m_z^2 + K_1\left(m_x^2 m_y^2 + m_z^2 m_y^2 + m_x^2 m_z^2\right) - K_u(m \cdot s)^2 \qquad (2.24)$$

where the first term is the Zeeman energy, the second term is with shape anisotropy of the sample and the following two terms describe the cubic and uniaxial magnetocrystalline anisotropy with respective coefficients $K_1$and K_u, with the unit vector s along the uniaxial anisotropy easy axis. (Further terms in uniaxial and cubic anisotropy can be omitted). In the chosen coordinate system, the *x*, *y*, and *z* axes correspond to the main crystallographic directions [100], [010], and [001] (normal to the layer plane), respectively. At equilibrium, the value of gyromagnetic ratio γ_0 and B_{eff} determines the fundamental magnon frequency, while its direction sets the equilibrium orientation of the magnetization. In contrast to the Larmore frequency of isolated magnetic moment precession, the magnetic system with complex, non-spherical free energy density distribution has a frequency-dependent second derivatives of the free energy density $F_{\theta\theta}$ and $F_{\phi\phi}$ on polar angle θ and in-plane azimuthal angle φ. The angles are counted from the normal to the layer plane and from the [100] crystallographic direction, respectively. The frequency of the ground mode (uniform magnetization precession with $q = 0$) is given by the expression:

$$f = \frac{\gamma}{2\pi}\sqrt{F_{\varphi\varphi}F_{\theta\theta}} \qquad (2.25)$$

In the case of ferromagnetic materials this frequency is in the GHz range (*36*). The magnetization

precession is induced by temperature modulation that changes B_{eff} through temperature-depend parameters of free energy density F_M: M_0, K_1 and K_u. In the temperature range of our studies, their dependence is linear. Depending on the way we deposit the energy in the film, we can excite uniform precession of magnetization when temperature modulation is uniform throughout the film, and when the gradient of temperature is present, it is possible to excites multiple standing modes as well launch spin waves- magnons with a non-zero k vector(*37*).

The temperature modulation plays the main role in the generation of coherent magnons in our studies of ferromagnetic thin films. It is possible to approximate complex processes of laser pulse energy deposition in the sample by a single model that contains three energy reservoirs – electrons, lattice, and spins. The three-temperature model presented in Fig.2.11 describes the temporal evolution of the system temperature by three coupled differential equations (*10*):

$$\frac{C_e d(T_e)}{dt} = -G_e((T_e - T_l) - G_{es}((T_e - T_s) + S(t) \quad (2.26)$$

$$\frac{C_s d(T_s)}{dt} = -G_{es}((T_s - T_e) - G_{sl}((T_s - T_l) \quad (2.27)$$

$$\frac{C_l d(T_l)}{dt} = -G_{el}((T_l - T_e) - G_{sl}((T_l - T_s) \quad (2.28)$$

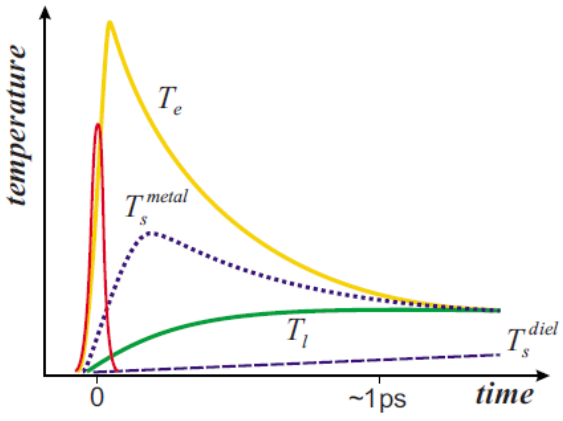

Fig. 2.11 The three-temperature model showing the schematic time evolution of electron, lattice, and spin temperature (11). After the pulse arrival at t=0, the electron system absorbs the energy and its temperature raises instantaneously followed by the lattice and the spin temperature. In the case of metals with strong coupling spin temperature increases much faster than lattice temperature or spin temperature in weakly coupled dielectrics.

Where G is the coupling between reservoirs, C is heat capacity and T is an effective temperature of the corresponding system. The G coefficient is rather a phenomenological parameter and doesn't provide information on the nature of the interaction. However, it tells us how strong a particular link is, in metals

electron-spin coupling is stronger than electron-phonon coupling providing spin temperature dynamics in the sub-picosecond range (*10*) . Depending on heat capacity, the temperature of the systems can differ drastically, electrons get 'hot' almost instantaneously, while it takes approximately 1ps in metals to transfer the heat to the lattice. The ultrafast demagnetization and general dynamics of the spin system, and their coupling with the photon and electron reservoir is a topic of many studies (*38-40*) . However, in the scope of this thesis, we can simplify the problem and assume a very fast (below 1ps) shift of $\mathrm{B}_{\mathrm{eff}}$ followed by the magnetization precession in the GHz frequency regime(*10*).

2.6 Detection of GHz-frequency coherent magnons by the Magneto-Optical Kerr Effect

For detection of the high-frequency coherent magnons in the scope of this work, the magneto-optical effect is used. It was discovered back in XIXth century by showing that light passing through the material in a magnetic field was changing its polarization plane. This phenomenon is called a Faraday effect, which one may observe in transparent samples. In the experiments presented in the scope of this thesis, magneto-optical Kerr effect is exploited which results with a change of probe beam polarization after being reflected from the magnetized sample. The effect is connected with the spin-orbit coupling phenomenon and for exact treatment, one needs to use perturbation theory. However, it can be simplified to the problem of wave optics. Magnetized sample give different energy contribution to the right-handed circular polarization and different to the left-handed polarization, therefore they have different refractive index. A linearly polarized light which can be consider as superposition of two circular polarizations is reflected from the sample, but due to the phase delay between circular polarizations, the linear polarization plane rotates. When in the pump-probe experiment, the pump pulse heats the sample, the net magnetization moment starts to precess around the new equilibrium changed via temperature-dependent parameters of a magnetocrystalline anisotropy. It results with a dynamic change of the reflected probe beam polarization plane. Polarization plane rotation can be detected by separating orthogonal polarization of the beam by Wollaston prism and directing them at balanced photo-diodes which will give an oscillatory signal following the change of particular magnetization component. Kerr effect measurements can be performed in various geometries with respect to the direction of the detected component of the magnetic moment (Fig.2.12). When one measures the transverse component (TMOKE), no overlap of wave vector of the probe beam and magnetization is present, and only a change

in total reflectivity can be detected. Under significant angle detecting longitudinal component is possible (LMOKE). In the scope of this thesis, however, the Polar MOKE (PMOKE) is used, where we detect Kerr rotation angle $\delta\theta_K$ proportional to the out-of-plane magnetization component modulation.

$$\delta\theta_K \propto \delta m_z(t)$$

In case of a normal incidence detection with probe beam that has finite absorption length ζ, detected component of magnetization precession is governed by coupling interval:

$$\delta m_z(t) = \int_0^\infty \delta m_z(z,t) e^{-z/\zeta} dz$$

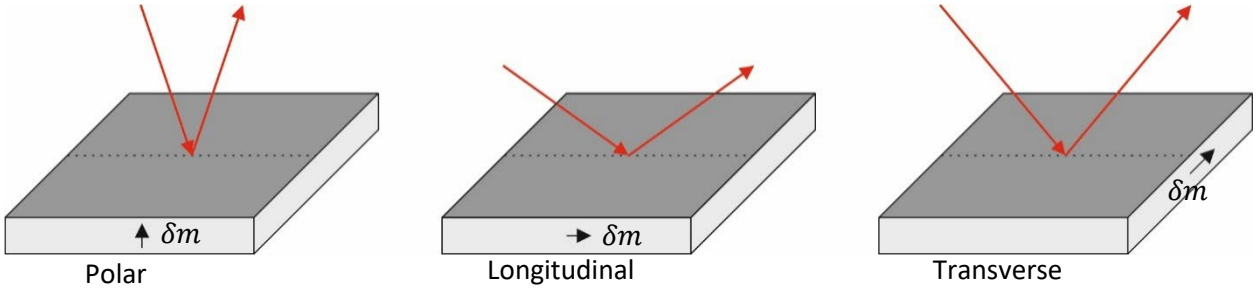

Fig. 2.12 Geometries of the detection of the surface magneto-optical Kerr effect:

PMOKE- detection of magnetization parallel to the incidence plane and perpendicular to the surface.

LMOKE- detection of magnetization parallel to incidence plane and parallel to the surface.

TMOKE- detection of magnetization perpendicular to incidence plane and parallel to the surface.

3

Giant photo-elastic effect in the vicinity of exciton resonance in a GaAs/AlAs superlattice for detection of coherent phonons.

In past years, localized phonons were successfully excited and detected with suspended nanostructures reaching quantum sensitivity (*41-46*). Recently significant progress was also made in the efficient generation and detection of the phonons in the non-suspended optomechanical nano-cavities(*47-51*). However, the detection sensitivity of propagating coherent phonons in sub-THz regime, which might become a logistic element of quantum computing networks (*52-54*) remained so far insufficient to count single phonons. In the scope of this thesis, it is shown that it is possible to reach the quantum sensitivity of propagating phonon detection in non-cavity nanostructures. Based on previous studies, a short-period semiconductor superlattice (SL) (*55-57*) is proposed, in which probe photons and SL excitons, when in resonance, form an ensemble analogous to exciton-polaritons in bulk semiconductors which exhibits giant-photoelasticity. The giant photo-elastic effect is used to enhance TDBS signals for detection of finite number of propagating coherent phonons (*58*).

The initial experiment helped us to characterize the exciton resonance of the SL by analyzing the reflectivity spectrum of the studied sample measured with a halogen lamp and a spectrometer. Subsequently, a standard pump-probe experiment was performed for excitation and detection of coherent phonons propagating through the sample. The fs probe pulse is used with spectrum width significantly exceeding the SL exciton resonance. The analysis of Time Domain Brillouin Scattering (TDBS) signals obtained for a wide range of pump powers provided information about frequency specrum of detected phonons and the identification of linear and non-linear regimes of coherent phonon wave packet propagation, helpful in following experiments. The main part of this chapter focus on invastigating the influence of giant photoelasticity of exciton resonance on sensitivity of the coherent phonon detection. Applying the spectrally narrow probe pulses in the vicinity of the resonance show that exciton-polariton possesses giant photoelasticity and provides TDBS signals with amplitude three orders of magnitude higher than when probing away from the resonance. Such detection sensitivity of optical reflectivity change in a pump-probe technique appears prospective for distinguishing of single quanta of phonons propagating through a medium in a form of the acoustic pulse.

Additionally, TDBS signals were measured with various excitation pump power and performed initial analisys of interaction between propagating coherent phonons wave packet of various amplitudes with probe pulse in the vicinity of exciton-polariton resonance of the SL. Presented data shows saturation of detected signal amplitude as well as energy blue-shift of probe beam reflected from the strain pulse propagating towards the surface and red-shift while reflected from the strain pulse propagating back towards the substrate.

Performed experiments and analysis lay the ground for further investigation of giant photo-elasticity of exciton-polariton resonance in semiconductor superlattices and exploiting it for detection of coherent phonons with quantum sensitivity as well as studies of propagating high amplitude coherent phonon wave packets.

3.1 Sample

The GaAs/AlAs SL structure was grown by the molecular beam epitaxy on a semi-insulating (100) GaAs substrate. In a chamber with pressure 4.3×10^{-8} mBar, 30 double layers were deposited at the temperature of 610°C, with a deposition rate of 0.19 nm/s for GaAs and 0.1nm/s for AlAs. The substrate was rotated and heated at the platform for uniform deposition. The studied superlattice consists of 30 periods of GaAs and AlAs layers with thicknesses of 12 and 14.2 nm, respectively. Additionally, a single 10 nm QW of $Ga_{0.95}In_{0.5}As$ was grown 200nm below the SL structure. Direct energy gap for AlAs is E_{g1}=3,13 eV and for GaAs E_{g2}=1,52 eV (at 4K), while lattice constants are 566pm and 565pm respectively (*59*) . Due to the above parameters potential well is relatively deep and there is no strain stored in the nanostructure. After fabrication, the substrate was polished down to 100 µm thickness and an Al film of 100 nm thickness was deposited on its backside by magnetron sputtering. The structure of the specimen is presented in Fig.3.1.

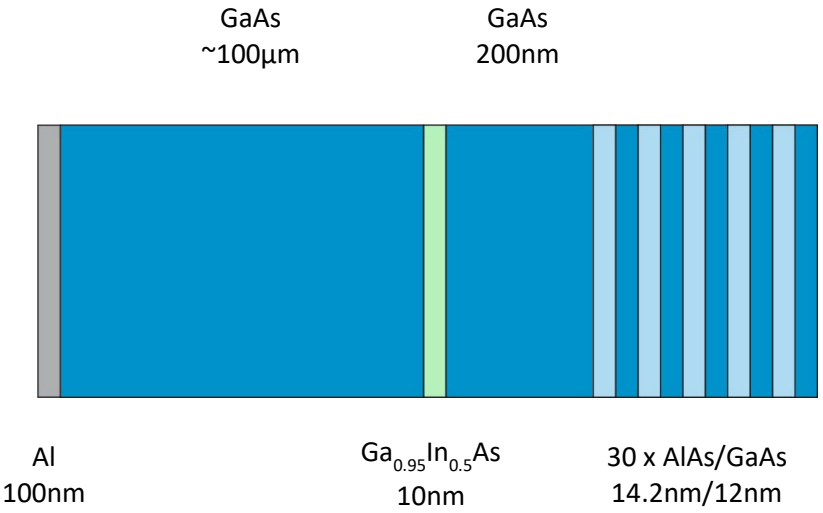

Fig. 3.1 Schematics of the sample consisting of a 30-period superlattice of AlAs(14.2nm)/GaAs (12nm) deposited on GaAs substrate of 100µm thickness. 200nm below the structure GaInAs QW was grown. On the back of the sample, 100nm aluminium film was deposited for the excitation of phonons.

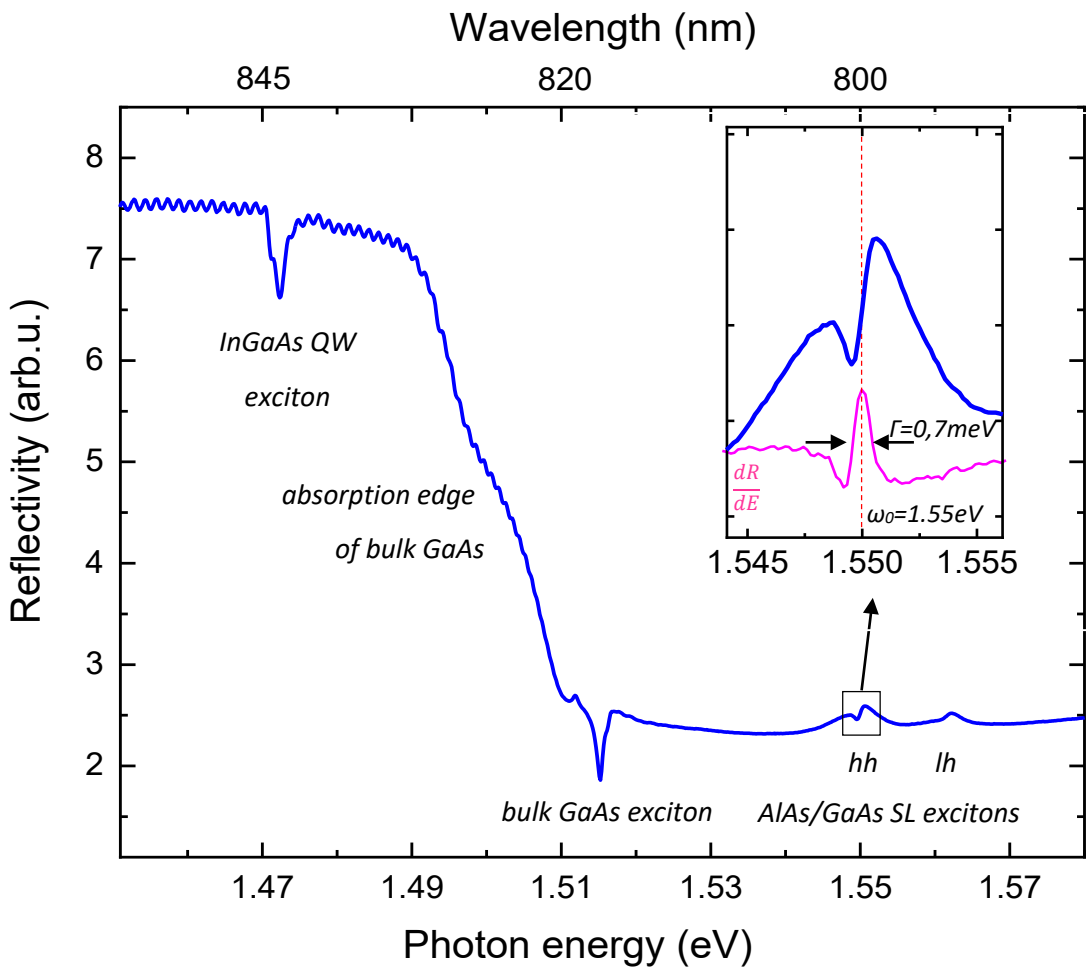

Fig. 3.2 Reflectivity spectrum of the sample with visible exciton peak of InGaAs deposited below the SL, absorption edge of bulk GaAs and its excitonic resonance, and heavy hole and light hole exciton resonances of the GaAs/AlAs superlattice, which is shown in the inset, together with the derivative of reflectivity signal revealing the width of the resonance.

In order to characterize the band structure and dielectric properties of the sample at the temperature of 5K, reflectivity measurements were done. Spectrally broad light from a halogen lamp was directed at the sample and reflection was collected and analyzed by Acton spectrometer from Prinston Instruments with the following parameters: 600 Groves per millimeter, 632 nm blaze wavelength, and 0.5m focal length. The reflectivity spectrum of the sample in the range between 1.45 eV and 1.58 eV is presented in Fig.3.2. One can observe a steep absorption edge of bulk GaAs between 1.49-1.51 eV (820-830nm). Clear exciton peak coming from InGaAs QW is visible at 842nm (1.472 eV), followed by the bulk GaAs exciton peak at 1.515 eV (818 nm), which is in agreement with data available in the literature (*60, 61*). At 1.55 eV (800

nm) one can distinguish heavy hole exciton resonance of GaAs/AlAs superlattice followed by the light hole exciton resonance at 1.563 eV (793 nm). The position of these peaks is governed by the width and depth of the potential well. If one would consider infinite potential QW, the shift from bulk exciton resonance would be defined by quantization energy equation:

$$E_Q = \frac{\hbar^2\pi^2}{2m_{e,h}l^2} \cdot \frac{1}{n^2}, \qquad n = 1,2,3 \ldots \tag{3.1}$$

where $m_{e,h}$ is the effective mass of an electron or a hole, l is the width of the QW and $\hbar$ is a Planck constant. For GaAs QW of 12 nm width, assuming that the effective mass of an electron is 0.067 and effective mass of a hole 0.34 (*62*), then quantization energy for a ground electron bound state is equal:

$$E_{Qe} = \frac{\hbar^2\pi^2}{2m_e l^2} \approx 39meV \tag{3.2}$$

and analogically for a hole:

$$E_{Qh} = \frac{\hbar^2\pi^2}{2m_h l^2} \approx 7meV. \tag{3.3}$$

In systems like SL, where the potential of the well is finite, energy levels are modified and the number of bound states is limited. By solving Schrödinger equations for finite quantum well and matching wave functions to appropriate boundary conditions, one can obtain more accurate values of QW energy levels of holes and electrons, which are shifted closer to the energy gap. In Fig.3.2, one can see that exciton resonance of bulk GaAs centered at 1.515 eV and heavy hole (hh) SL exciton resonance positioned at 1.55 eV are separated by 35meV which is in good agreement with theoretical considerations. The SL exciton resonance presented in the inset of Fig.3.2 is governed by the effective dielectric function discussed in detail further in this chapter. The width of the resonance is governed by parameter $\Gamma = 0.7\ \mathrm{meV}$ - the decay rate of the exciton-polariton, also shown in the inset of Fig.3.2. In the vicinity of the superlattice exciton resonance, further studies of exciton-polariton interaction with coherent phonon wave packet will be presented in this chapter.

3.2 Experimental technique

For excitation of coherent phonons wave packet and detection of their interaction with probe beam in the vicinity of exciton-polariton resonance in SL structure, the pump-probe experimental setup presented in Fig 3.3a is used. Both pump and probe pulses are generated by regenerative amplifier system (RegA9000 manufactured by Coherent) with the following laser parameters: 100 kHz repetition rate, the average power of 300 mW, 200 fs pulse duration, and central wavelength at 800 nm (1.55 eV), centered at the position of the exciton resonance of the investigated sample. The laser beam is split by the beam splitter (BS1) on two paths: pump and probe. The pump beam is focused down to a 55 µm diameter spot on an aluminium transducer deposited at the back of the sample placed in flow helium cryostat. The sample chamber is cooled down to 5 K by the constant flow of helium. Optically induced heating of the metal causes the expansion of the lattice at the surface of the transducer and generation of the coherent phonons to wave packet in a form of a strain pulse propagating through the substrate towards the examined SL structure (see Fig.3.3b). Details of the optical generation of coherent phonon wave packet are explained in Chapter 2. The probe beam is delayed by a fixed delay line by 20 ns respectively to the pump, which is the time corresponding to the travel time of the strain pulse through the 100 µm GaAs substrate. The probe is focused at sample front with deposited SL down to 50 µm diameter spot. Coherent phonons are detected by the Time Domain Brillouin Scattering (TDBS) signal (see Chapter 2), which is obtained by the measurement of reflectivity change $\Delta R(t)$ by a balanced photoreceiver manufactured by Newport, model Nirvana 2007 (BDR). The time window and resolution are provided by an automated variable mechanical delay line installed into the optical path of the pump beam. The signal-to-noise ratio is improved by lock-in detection using a 10-MHz Zurich Instruments Lock-in Amplifier synchronized with a mechanical chopper modulating the pump beam with the frequency of 1.2 kHz. Additionally, a visualization scheme (VS) is implemented for the convenient realization of overlap of pump and probe.

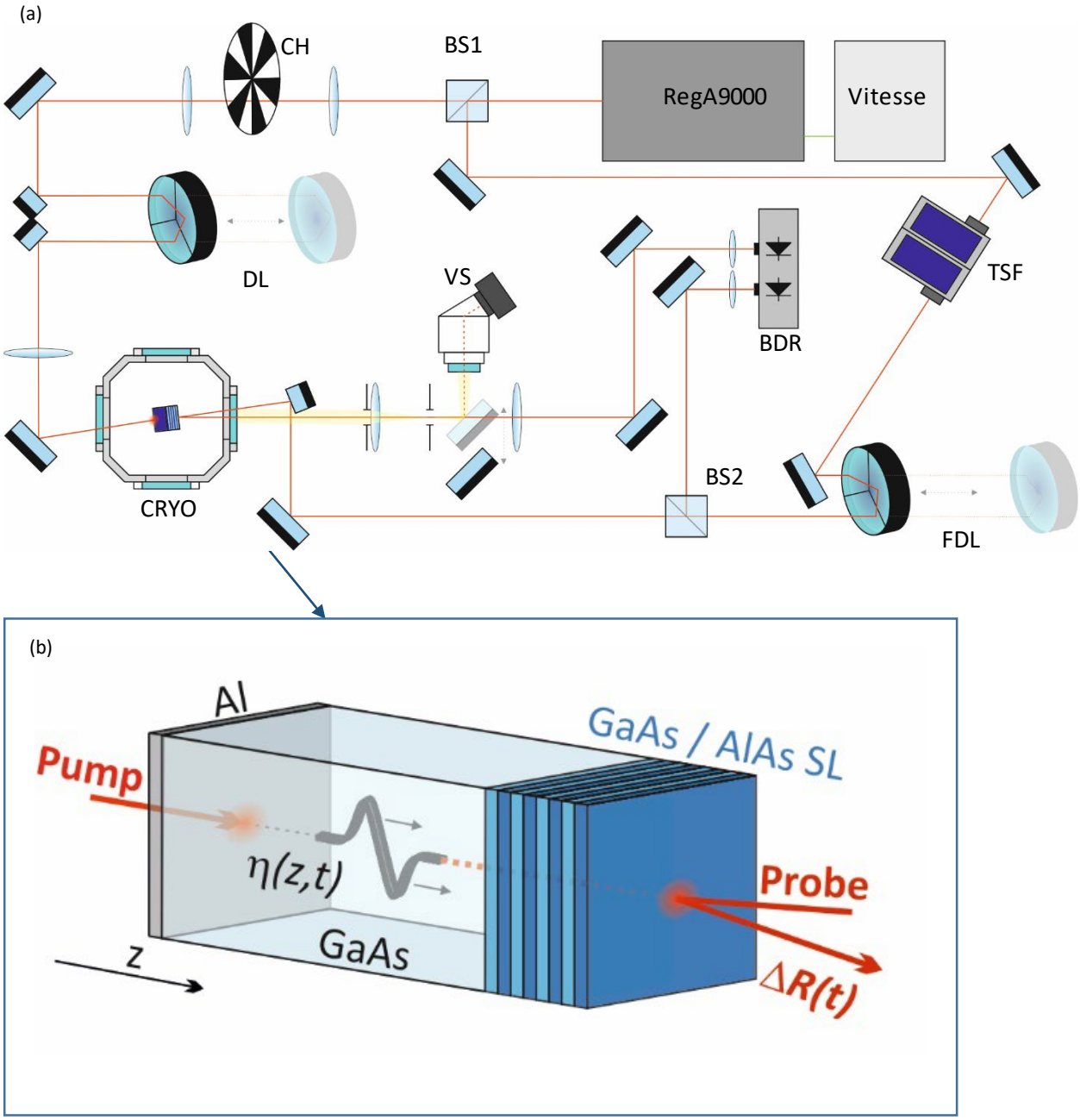

Fig. 3.3 (a) Experimental pump-probe setup based on the mechanical delay of the pump beam. BS1 – beam splitter, CH- chopper, DL – pump pulse delay line, CRYO- cryostat, TSF – tunable spectral filter, FDL – fixed delay line for probe, BS2 – beam splitter, VS- visualization scheme containing a movable mirror, microscope objective and CCD camera, BDR- balanced detector.

(b) Schematic of excitation and detection of propagating strain pulse in the GaAs/AlAs superlattice deposited on GaAs substrate. Pulse is generated at the backside of the sample by heating and expanding 100nm Al transducer, then it is launched into the 1 μm GaAs substrate and travels towards the surface. It is detected by dynamic interference of beams reflected from the surfaces of the sample and the strain itself providing a change in reflected light intensity.

The central wavelength of the probe pulse and its spectral width are controlled by a variable liquid crystal filter (Varispec). Additionally, a set of neutral density filters is introduced to normalize and control probe fluence. For initial measurements without a spectral filter, the probe beam directly from the laser is used. The probe pulse presented in Fig.3.4b spectral width is 20 meV ($\tau_{probe} = 200$ fs) and covers fully exciton-polariton resonance of the SL. For wavelength dependence measurements in the vicinity of resonance, the probe pulse is narrowed down to 1.4 meV ($\tau_{probe} = 1.3$ ps) and its intensity is normalized. A comparison of the filtered and normalized probe pulse with exciton resonance is presented in Fig.3.4a. The initial spectrum of the probe and normalized filtered probe spectrum is shown in Fig.3.4b.

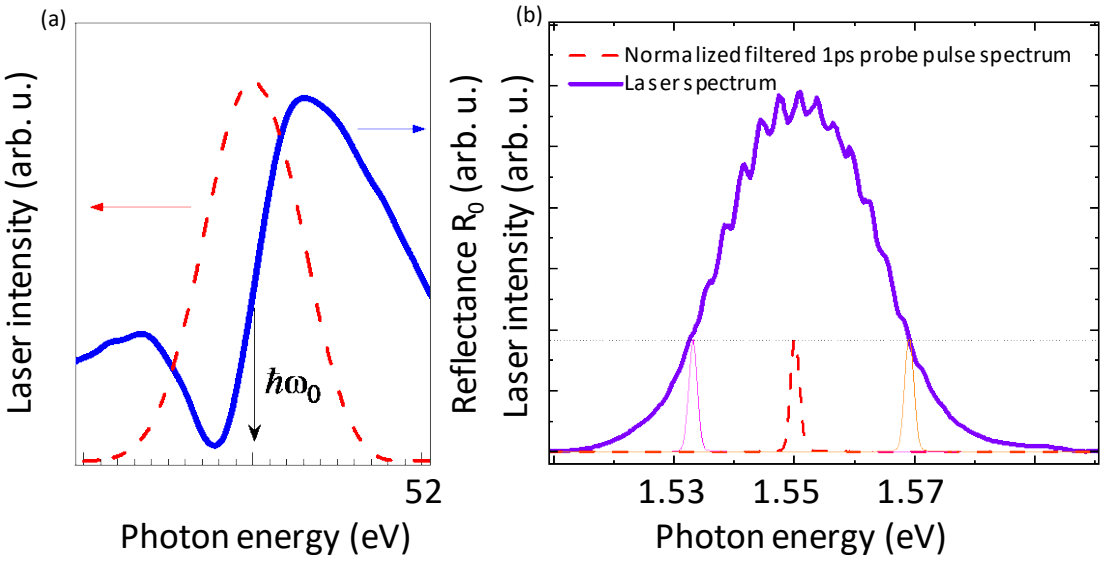

Fig. 3.4 (a) Reflectance spectrum of the sample (blue) in the vicinity of exciton resonance taken from Fig. 3.2 inset, put together with 1.35ps probe pulse spectrum (red dashed), (b) initial laser spectrum of 200fs probe pulse (purple) put together with the filtered and normalized spectrum of exemplary probe pulses of 1.35ps in the full range of photon energies from 1.53eV up to 1.57eV.

3.3 Detection of coherent phonons with the fs probe pulse

Initial pump-probe measurements of phonon interaction with the exciton-polariton in semiconductor SL were performed without a spectral filter. The probe spectrum fully covers the exciton resonance spectrum of the SL (see Fig.3.4). It lays however away from the exciton resonance for GaAs substrate (1.44 eV). Measured data has oscillatory nature which is known from time-domain Brillouin scattering (TDBS) signals (*22, 27, 63*). In the experiment, various excitation densities of the pump ranging from $J = 0.3\ \mathrm{mJ/cm^2}$ up to $J = 30\ \mathrm{mJ/cm^2}$ were used. The structure of the signal obtained with $J = 2.5\ \mathrm{mJ/cm^2}$ shown in Fig.3.5 shows enhancement of interaction between phonons and photons in the superlattice compared to the interaction in bulk GaAs substrate. One can see phonons in the substrate propagating towards the surface, manifested by low amplitude oscillations, then reaching the SL at $t = -150$ ps. Oscillations with high amplitude correspond to the time of phonons propagating through the SL in the time interval between -150 ps<*t*<150 ps. At $t = 0$ strain pulse gets reflected from the surface and propagates back towards the substrate. The enhancement comes from the fact that the probe beam spectrum is covering exciton-polariton resonance of SL where the modulation of reflectivity ΔR by propagating phonons that change refractive index is more pronounced. The signal amplitude rise on its way to the surface and its decay on the way back is caused by absorption of the probe beam, which for given material and wavelength is governed by absorption coefficient which for GaAs is $\alpha \approx 10^4\ \mathrm{cm^{-1}}$ (*64*). By using Beer-Lambert law, we can estimate the intensity of light that penetrates the sample and it is given by following equation: $I(z) = e^{-\alpha z}$. In structured layered samples like SL, signal consist of contribution from photo-elastic effect and contribution coming from the displacement of the material interfaces caused by strain. Since total reflectivity consists of reflections from all surfaces, when one of them is

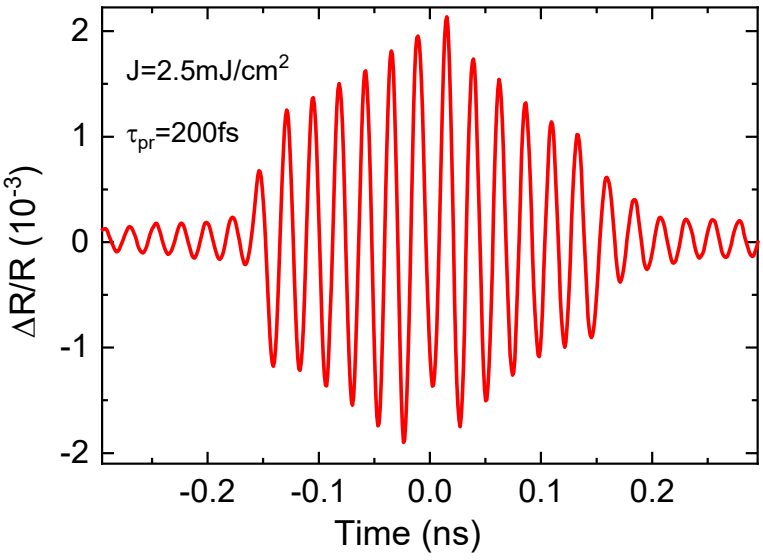

Fig. 3.5 TDBS signal for linear regime excitation density (2mJ/cm²). Experimental data.

shifted, the phase shift of the reflected beam from this interface changes its contribution to the signal. These two mechanisms are mutually dependent, since SL properties depend on the position of the interfaces, but their contribution significance depends on the probe wavelength, material properties and design of the nanostructure. In the case of measurements performed with 800 nm probe in the GaAs/AlAs SL, the photo-elastic effect is more pronounced than the interference effect originating from the surface displacements. It is due to matching refractive indexes of the materials and negligible contribution to the signal of the reflections from individual interfaces while phonons propagate through it. Therefore, further, we focus only on the photo-elastic effect.

The comprehensive studies of propagating phonon wave packet interaction with exciton-polariton resonance in SL using various pump fluence values J were performed. Results of the measurements are presented in Fig.3.7a. The detected TDBS signals are presented in Fig 3.5 and Fig.3.7a. The dominant frequency of measured oscillations, governed by the selection rule for TDBS discussed in Chapter 2, where q is phonon vector and k is photon vector.

$$q = 2k = \frac{2 \cdot 2\pi n}{\lambda} \approx 5.2 \cdot 10^7 m^{-1} \tag{3.4}$$

$$f_B = \frac{qv}{2\pi} \approx 42GHz \tag{3.5}$$

where the refractive index of GaAs is $n = 3.3$, $\lambda = 800$ nm is the wavelength of the probe in a vacuum and $v = 5000$ m/s is a sound velocity with which coherent phonon wave packet propagates. In linear regime, the increase of pump fluence J cause the increase of the amplitude η_0 of coherent phonons wave packet in a form of the bipolar strain pulse. Increased amplitude of a strain results with a broader spectrum of excited phonons and higher amplitude of the oscillations (see Fig.3.6).

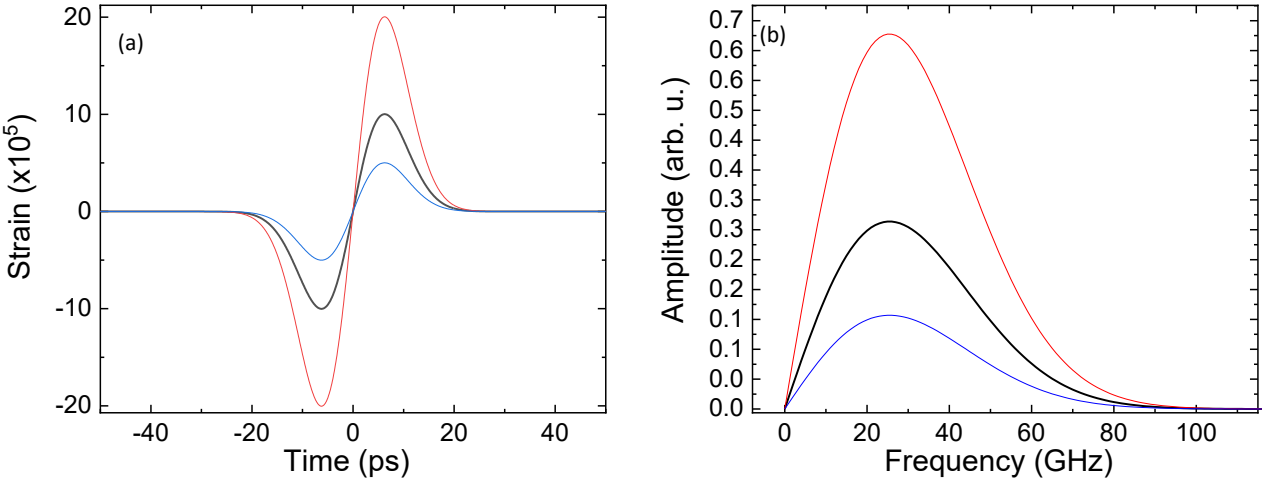

Fig. 3.6 (a) Simulated bipolar strain pulse for various excitation densities J, (b) corresponding frequency spectrum obtained by Fourier transform of the temporal dependence.

The shape of the strain pulse and its spectral components depend on the excitation density and material used for transducer as well as linear and non-linear properties of the material in which it propagates and the distance the pulse travels. Due to periodicity of the SL the phonon dispersion relation is folded, therefore, in the signal one can observe multiple frequencies with the same wave vector q. Fourier transform of the signal detected for pump fluence of $J = 2.5\ \mathrm{mJ/cm^2}$ together with folded dispersion relation for studied SL (*65*) is presented in Fig.3.7c.

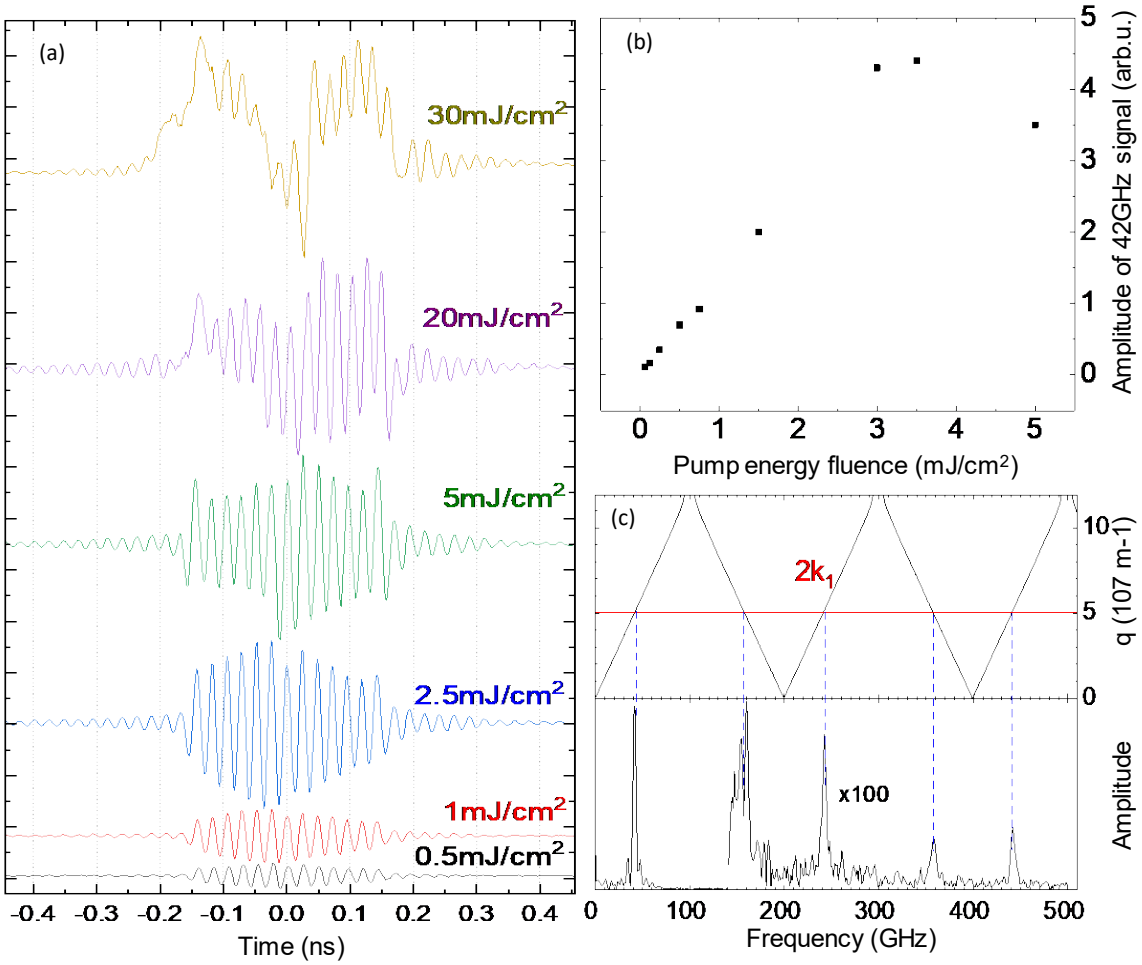

Fig. 3.7 (a) TDBS signals for various pump energy fluence detected with 200fs probe pulses with 15nm spectral width. (b) Amplitude of f_B =42GHz signal dependence of pump energy fluence, showing linear response up to 3mJ/cm^2. (c) Fourier transform of 2.5mJ/cm^2 TDBS signal showing detected frequencies up to 500GHz of propagating phonon wave packet, which corresponds to calculated dispersion relation of folded phonons in studied superlattice.

Fourier transform of ΔR demonstrates a pronounced signal at $f_B \approx 42\mathrm{GHz}$ and weak spectral lines for frequencies up to 450GHz. For low values of pump fluence between $J = 0.3\ \mathrm{mJ/cm^2}$and $J = 3\ \mathrm{mJ/cm^2}$ one can observe a linear increase of the amplitude of the signal with a frequency of 42GHz presented in Fig.4.7b. For higher pump fluencies above $J = 3\ \mathrm{mJ/cm^2}$, after travelling through 100μm GaAs substrate, coherent phonon wave packet propagates in a nonlinear regime. The negative part of the strain pulse travels faster than the positive one, forming the N-shaped pulse and the acoustic solitons travelling faster than the speed of sound v mentioned above (*66, 67*). The higher the initial strain amplitude gets the more pronounced effect of broadening of the propagating coherent wave packet is, as well as broadening of the spectrum. It explains why for the highest excitation density $J = 30\ \mathrm{mJ/cm^2}$ one can see the arrival of the pulse at SL happens 50ps earlier than it does for linear regime propagation of the strain pulse. It also explains the rise of the signal amplitude at Brillouin frequency in function of pump energy fluence presented in Fig.3.7b. However, it does not explain why above the threshold around $J = 3\ \mathrm{mJ/cm^2}$ the amplitude of the f_B drops and the shape of the signal spectral components change. The assumption is, that broadening of the exciton-polariton resonance by phonon wave packet lays the ground for it. The measurements with the probe beam covering fully the exciton resonance allowed setting the linear regime for phonon interaction with exciton-polariton in the studied sample. For the linear case, we can very accurately predict the properties of the acoustic pulse we launch into the sample and what characteristics the TDBS signal it will have, this gives ground to study probe spectral dependence in the vicinity of exciton resonance, which will be described in the next chapter.

3.4 Detection of coherent phonons with the ps probe pulse

After the measurements with probe beam fully covering exciton-polariton resonance and establishing a linear and non-linear regime for propagation of coherent phonons wave packet, conclusions are that the main mechanism governing TDBS reflectivity signal is related to the exciton-polariton resonance. In order to study its contribution to obtained signal, the probe pulse was spectrally narrowed with a liquid crystal spectral filter achieving spectral line of 0.7 nm (1.4 meV), which allows scanning over the exciton resonance of the SL using probe photon energies between 1.544 eV and 1.556 eV with the step of 0.25 nm (~0.5 meV). The energy fluence of the probe was kept below 300nJ/cm^2 in order to avoid non-linear excitation effects (*68*). Exemplary signals presented in Fig.3.8a show the propagation of the strain pulse through the SL, starting at approx. $t = -150$ ps, being reflected from the surface at $t = 0$ and afterwards propagating back towards the substrate. Energy fluence of the pump, exciting phonon wave packet was $J = 0.5\ \mathrm{mJ/cm2}$, which results with exciting coherent phonon wave packet in form of the bipolar strain pulse. It is seen that the amplitude of the signal grows substantially while approaching exciton resonance at 1.55 eV. Signals can be carefully analyzed by fitting decaying sine function with parameters characteristic for TDBS signals: f_B-frequency of the oscillations, p_B - phase of the oscillations, A_B - amplitude of the oscillations, and τ_B^{-1}- decay rate. Dependences of these parameters on photon energy are presented in panels b-e in Fig.3.8. Open symbols represent analysis performed for phonons propagating toward the free surface (anti-Stokes) and filled symbols for phonons propagating backward (Stokes). The amplitude A_B of the oscillations presented in Fig.3.8b is rising symmetrically while closer to the exciton-polariton resonance and has its maximum at 1.55 eV. Similar behaviour is visible for decay parameter τ_B^{-1} in Fig3.8e, which is related to the absorption coefficient being highest at the resonance. On the other hand, the dependence of phase p_B (Fig.3.8c) and frequency f_B (Fig.3.8d) is asymmetric, which indicates that TDBS scattering in the vicinity of exciton-polariton is governed by its interaction with the phonon wave packet. Amplitude A_B of the TDBS signal, when probing with energy equal to resonance energy is $\frac{\Delta R}{R} \approx 10^{-2}$. For used pump fluence, $J = 0.5\ \mathrm{mJ/cm^2}$ the amplitude of strain pulse is expected to be $\eta_0 \approx 10^{-5}$, in previous studies performed in GaAs away from exciton resonance TDBS signal has an amplitude of approx. $\frac{\Delta R}{R} \approx 10^{-5}$ (*65, 69*). It means that in the present experiment we observe giant photo-elasticity of exciton-polariton and exceptionally high sensitivity to propagating coherent phonon wave packet being 3 orders of magnitude higher than in standard experiment.

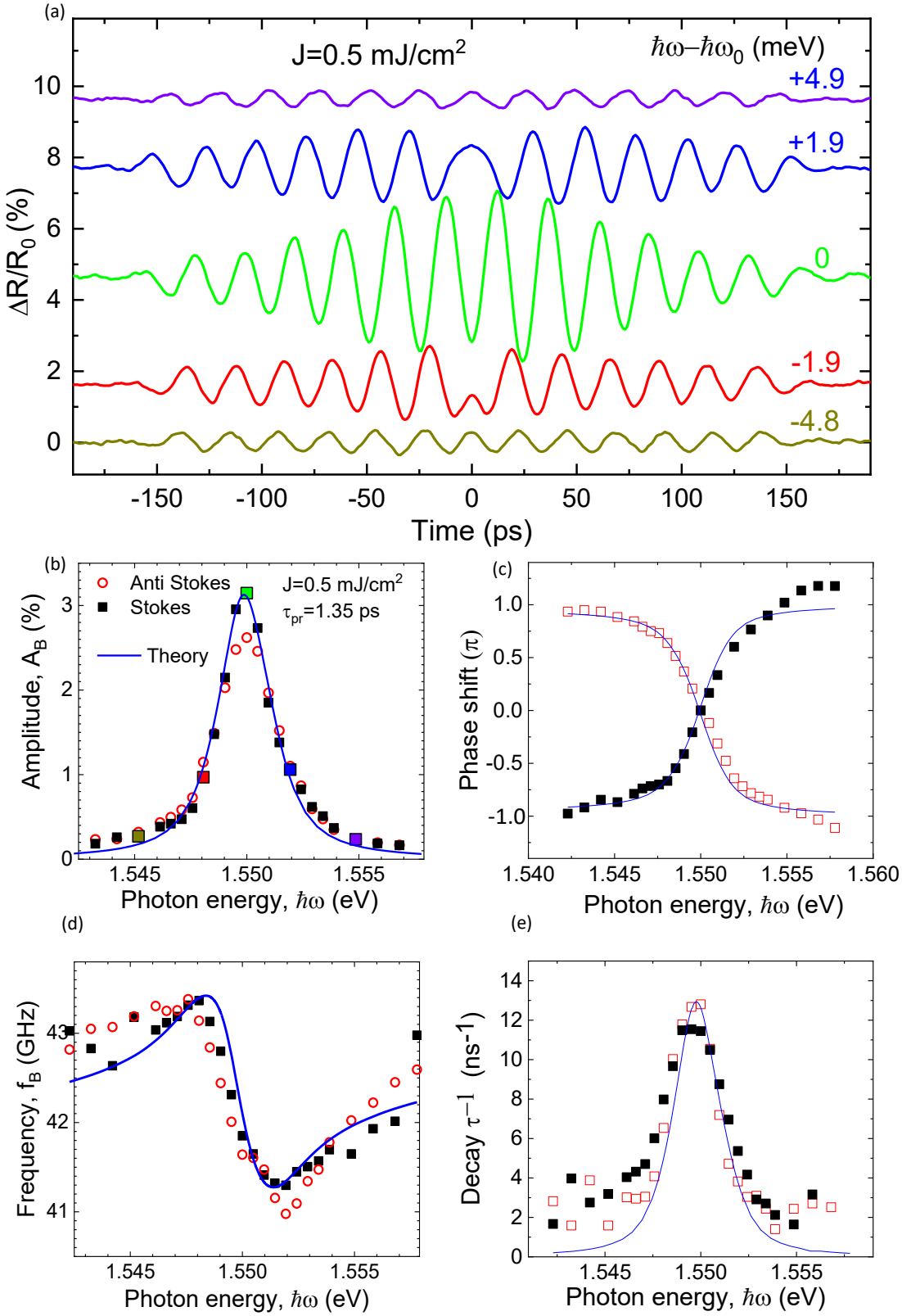

Fig. 3.8 (a) Exemplary TDBS signals in vicinity of exciton resonance. (b) spectral dependence of amplitude A_B of TDBS signal with distinction of Stokes (black) and anti-Stokes (red) dependences (c) phase dependence (d) frequency dependence (e) decay dependence.

3.4.1 Photo-elastic parameter in vicinity of exciton resonance

For a qualitative description of observed phenomena our partners, Prof. Vitalii Gusev from Le Mans University, and Dr. Serhii Kukhtaruk, from V.E. Lashkaryov Institute of Semiconductor Physics from Kiev, developed a theoretical model. The simplified model assumes that the probe beam spectral width is infinitely small, and the amplitude of the signal can be estimated from the following equation:

$$\frac{\Delta R(t)}{R_0} = 2\mathrm{Re}\left[i \frac{1 - r_{01}^2}{r_{01}} \frac{dk_1}{d\eta} \int_0^\infty \eta(z,t) e^{2ik_1 z} dz \right] \tag{3.6}$$

where $k_1 = 2\pi\tilde{n}/\lambda$, $\tilde{n}$ and λ are probe wavevector, the complex refractive index in the SL and the wavelength of the probe light in vacuum, respectively, $r_{01} = (1 - \tilde{n})/(1 + \tilde{n})$ and $\eta(z,t) = \eta(z \pm vt)$ is the spatial-temporal profile of the strain pulse propagating along *z* in the SL. The integral is the coupling function between strain and the probe. The crucial parameter which governs the sensitivity of detection is $\frac{dk_1}{d\eta}$ which the in case of phonon-induced shift smaller than the resonance width can be described in the following way:

$$\frac{dk_1}{d\eta} = \frac{1}{2} \frac{k_1}{\varepsilon_{\mathrm{eff}}} \frac{\Xi}{\hbar} \frac{d\varepsilon_{\mathrm{eff}}}{d\omega_0} \tag{3.7}$$

where $\Xi = -10\mathrm{eV}$ is deformation potential for excitons in GaAs (*70*) and $\varepsilon_{\mathrm{eff}}$ is an effective dielectric constant, which in presence of exciton resonance can be described as follows:

$$\varepsilon_{\mathrm{eff}}(\omega) = \varepsilon_b \left[1 + \frac{\omega_{\mathrm{LT}}}{\omega_0 - \omega - i\Gamma} \right] \tag{3.8}$$

where $\varepsilon_b = 11.8$ is the background dielectric constant, $\omega_0 = 1.55$ eV is the resonant frequency and $\omega_{\mathrm{LT}} = 0.13\ \mathrm{meV}$ and $\Gamma = 0.7\ \mathrm{meV}$ are the longitudinal transverse splitting and non-radiative decay of the polaritons respectively. From the above equations, one can model the complex refractive index in the vicinity of the exciton resonance $\tilde{n} = n + i\kappa = \sqrt{\varepsilon_{\mathrm{eff}}}$ presented in Fig.3.9. Dependences of real part n and imaginary part κ of

refractive index and their derivatives, depicted in Fig.3.9, on the strain, provide a phenomenological explanation of the parameters of detected signals presented in Fig.3.8.

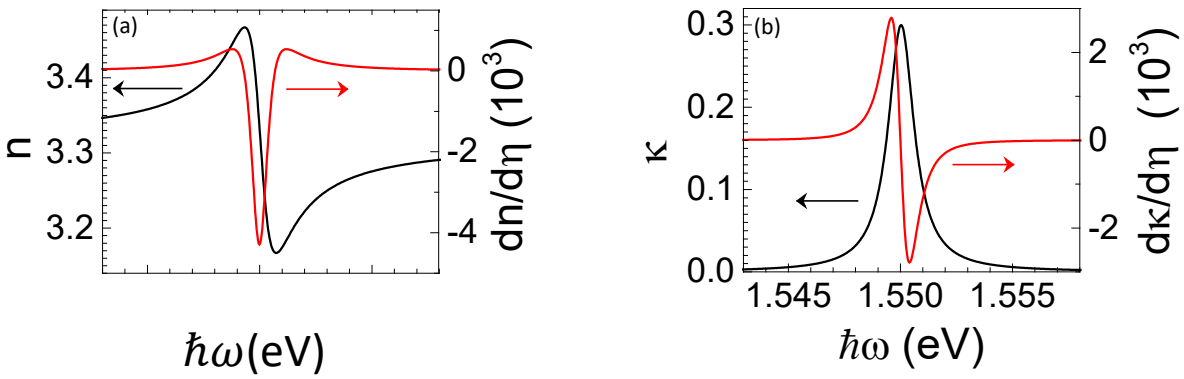

Fig. 3.9 Calculated spectral dependences of complex refractive index $\hat{n} = \sqrt{\varepsilon_{eff}}$ *and its derivatives. (a) real part (b) imaginary part.*

In our experiment the estimated maximal value of the linear photo-elastic parameter takes place in the exciton-polariton resonance is equal to:

$$p = -\frac{1}{\varepsilon^2}\frac{\partial \varepsilon}{\partial \eta} = -\frac{1}{\varepsilon_{GaAs}}\frac{\Xi}{\hbar}\frac{\omega_{LT}}{\Gamma^2} \cong -3 \cdot 10^2 \qquad (3.9)$$

leading to giant sensitivity in the detection of coherent acoustic phonons via monitoring of the phonon-induced transient permittivity variations by TDBS signals.

3.4.2 Phonon density calculations

When detecting changes in reflectivity $\Delta R/R_0$ with the probe pulse we observe its interaction with phonons that fulfil the selection rule. In this experiment, we detect phonons with Brillouin frequency $f_B = 42$ GHz. It is possible to calculate how many phonons is detected by calculating the spectral density of phonons $\widetilde{N}$. To do that, firstly one has to calculate the total energy of the pulse detected by the probe beam focused to the spot of diameter $D = 50\ \mu\text{m}$. Elastic energy can be described by the following formula:

$$U = \frac{1}{2} C_{11} \iiint \eta^2(z) dz dx dy \tag{3.10}$$

where $C_{11} = 119$ GPa is a longitudinal elastic module of GaAs(*71*). With the assumption that energy is distributed evenly over the detection area $A = \pi \left(\frac{D}{2}\right)^2$ the formula can be rewritten:

$$U = \frac{1}{2} A C_{11} \int \eta^2(z) dz = 8 \cdot 10^{-15} J \tag{3.11}$$

Subsequently, a Fourier transform of the temporal profile of an excited bipolar strain pulse has to be performed and the power of the frequency distribution has to be normalized to be equal to the total energy of the pulse U. Finally, in order to get a number of phonons per frequency and area one has to divide the result by the phonon energy (hf) and area of detection (μm):

$$\widetilde{N} = \frac{U}{\int df \int \eta(t)\, e^{-2i\pi f t} dt} \cdot \frac{1}{Ahf} \cdot \int \eta(t)\, e^{-2i\pi f t} dt \tag{3.12}$$

This gives us a number of phonons per particular frequency and area, the result of the calculation is presented in Fig.3.10. The range of detected phonons is governed by the size of SL and penetration depth of the probe at $f_B = 42$ GHz, which, for given SL and $\tau_B^{-1} = 12^{-1}$ns, is approx. 4GHz. This results in a number of detected phonons $\mathrm{N}_B \approx 10^4\ \mu\text{m}^{-2}$. Developed theory and calculation match experimental data for the amplitude of a strain pulse $\eta_0 = 3 \times 10^{-5}$, which corresponds to the pump fluence of $J = 0.5$ mJ/cm^2. In our studies, we also retrieved signals for excitation densities of $J = 0.1$ mJ/cm^2, which corresponds to $\mathrm{N}_B \approx 10^2\ \mu\text{m}^{-2}$ per pulse.

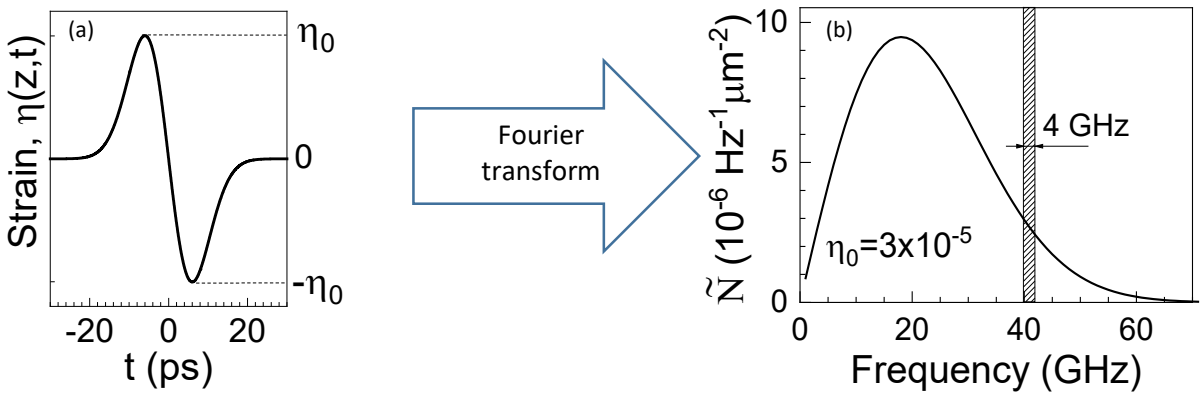

Fig. 3.10 a) Temporal profile of coherent wavepacket of phonons in a form of the strain pulse.

b) Calculated spectral density of phonons in the coherent wave packet.

3.4.3 High-density excitation

After spectral scan in the vicinity of the exciton-polariton resonance performed with pump fluence $J = 0.5\ \mathrm{mJ/cm^2}$, an analogical study was done with higher excitation densities up to $J = 3\ \mathrm{mJ/cm^2}$, which is at the limit of the linear regime for excitation of coherent phonons. Selected TDBS signals for $J = 2\ \mathrm{mJ/cm^2}$ and $J = 3\ \mathrm{mJ/cm^2}$ are presented in Fig.3.11a and b. In Fig.3.11c signal amplitude with frequency $f_B = 42$ GHz dependence on photon energy for various excitation power densities is presented. In both Fig.3.11a and b one can observe no reciprocity in the signal, its characteristics are different for anti-Stokes scattering, when phonons are propagating towards the surface (-150ps<t<0) and for Stokes, when they are propagating back towards the substrate (0<t<150ps).

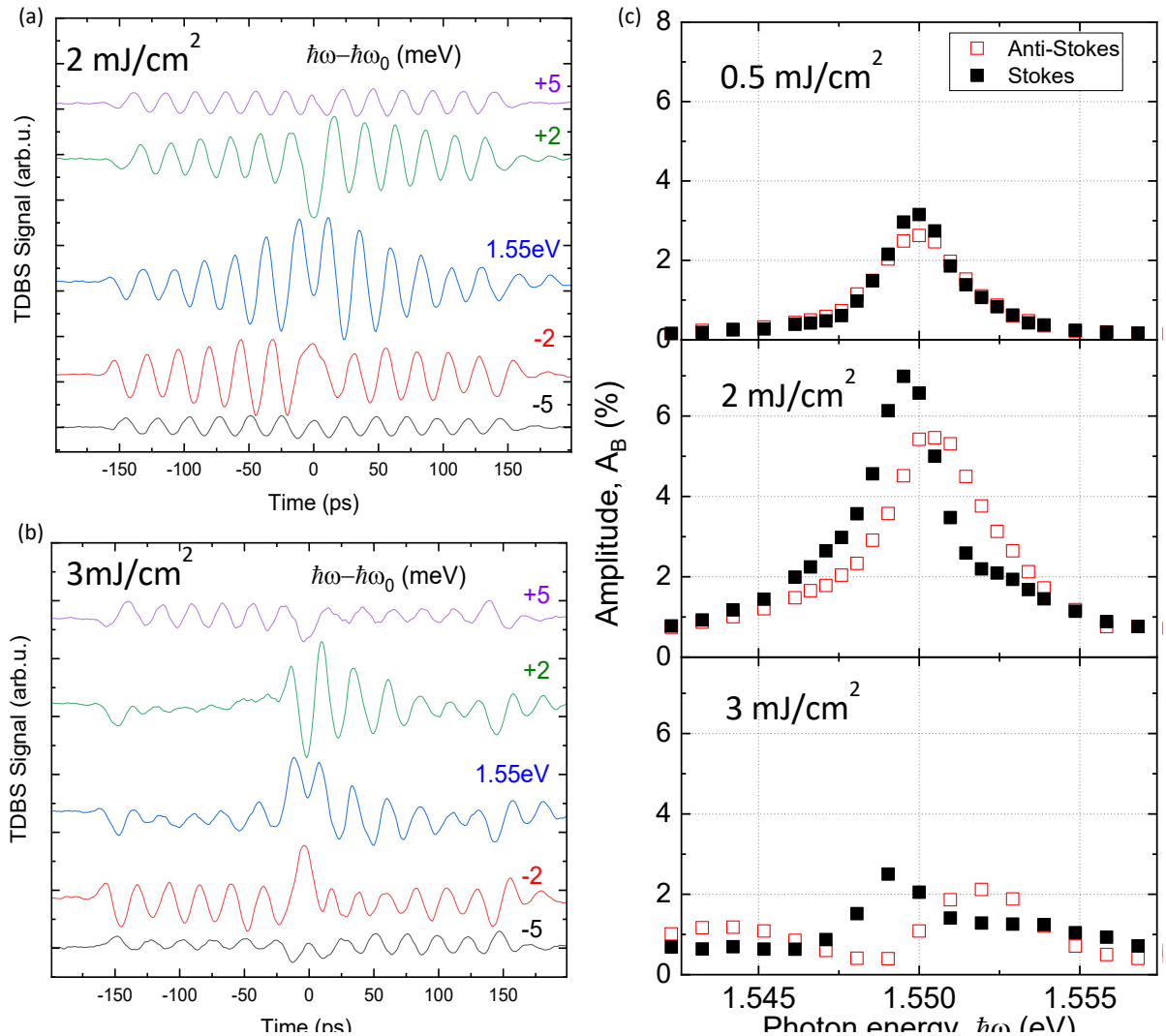

Fig. 3.11 (a) TDBS signals for excitation density J=2mJ/cm², (b) TDBS signals for excitation density J=3mJ/cm², (c) TDBS signals amplitude dependence on probe photon energy for Anti-Stokes and Stokes scattering.

While the amplitude of the TDBS signal is higher for excitation density $J = 2$ mJ/cm^2 than it is for 0.5 mJ/cm^2, it is already significantly smaller, almost diminishing for $J = 3\ \mathrm{mJ/cm^2}$, despite the fact it is still not a non-linear regime of phonon wave packet propagation. Therefore, the different mechanism has to be responsible for the decrease in the amplitude. When analyzing the whole amplitude spectral dependence presented in Fig.3.11c one can see not only the nonlinear behaviour of TDBS signal amplitude but also the peak of the maxima is shifted from the initial 1.55 eV. Blueshift is observed for phonons propagating towards the surface (Anti-Stokes) and redshift for phonons propagating back towards the substrate (Stokes).

Theoretical considerations presented in previous section are valid for small amplitudes of the coherent phonon wave packet, where the shift of the exciton-polariton resonance of the SL is significantly smaller than its width. In such case amplitude of the TDBS signal is proportional to the number of phonons N, strain pulse amplitude η_0 and excitation density J. Changes of signal parameters follow the real and imaginary part of the refractive index. For high amplitudes of the pump, however, exciton shift $\Delta\hbar\omega = \Xi\eta_0$ induced by strain is comparable with the width of exciton-polariton resonance Γ. In such case $\Delta\varepsilon$ cannot be considered constant and the reflectivity equation cannot be written in the form of Eq.4.21 providing a proportional response, instead $\Delta\varepsilon$ becomes dependent on time and coordinate and has to be included in the integral:

$$\frac{\Delta R}{R_0} = -\left(\frac{1-r_{01}^2}{r_{01}}\right) k_1 Re\left[i \frac{\omega_{LT}}{[\omega_0 - \omega - i\Gamma]} \int_0^\infty dz \frac{\omega_d \eta(z,t)}{[\omega_0 - \omega - i\Gamma + \omega_d \eta(z,t)]} e^{2ik_1 z} \right] \tag{4.23}$$

Qualitatively, for increasing high strain amplitudes, the sensitivity function broadens and then shifts away from $\hbar\omega_0$. The compressive part shifts it in one direction and the tensile part in the opposite. Effectively, the dependence $A_B(J)$ presented in Fig.3.12a measured at $\hbar\omega = \hbar\omega_0$ decreases for fluencies higher than $J = 2$ mJ/cm^2. What agrees with dependencies shown in Fig3.11c. There is no agreement however between experimental data presented in Fig.3.11c and theoretical considerations presented in Fig.3.12b for given amplitudes of strain η_0. Nevertheless, one can see a resemblance, while considering together data for Stokes and Anti-Stokes components. When a coherent phonon wave packet travels towards the surface (Anti-Stokes) we observe the blue shift, when it travels back towards the substrate (Stokes) we observe red shift. From this result, we can conclude that for higher strain amplitudes the incoming phonon wave packet is no longer a bipolar symmetric pulse, but it is asymmetric with a predominant compression component.

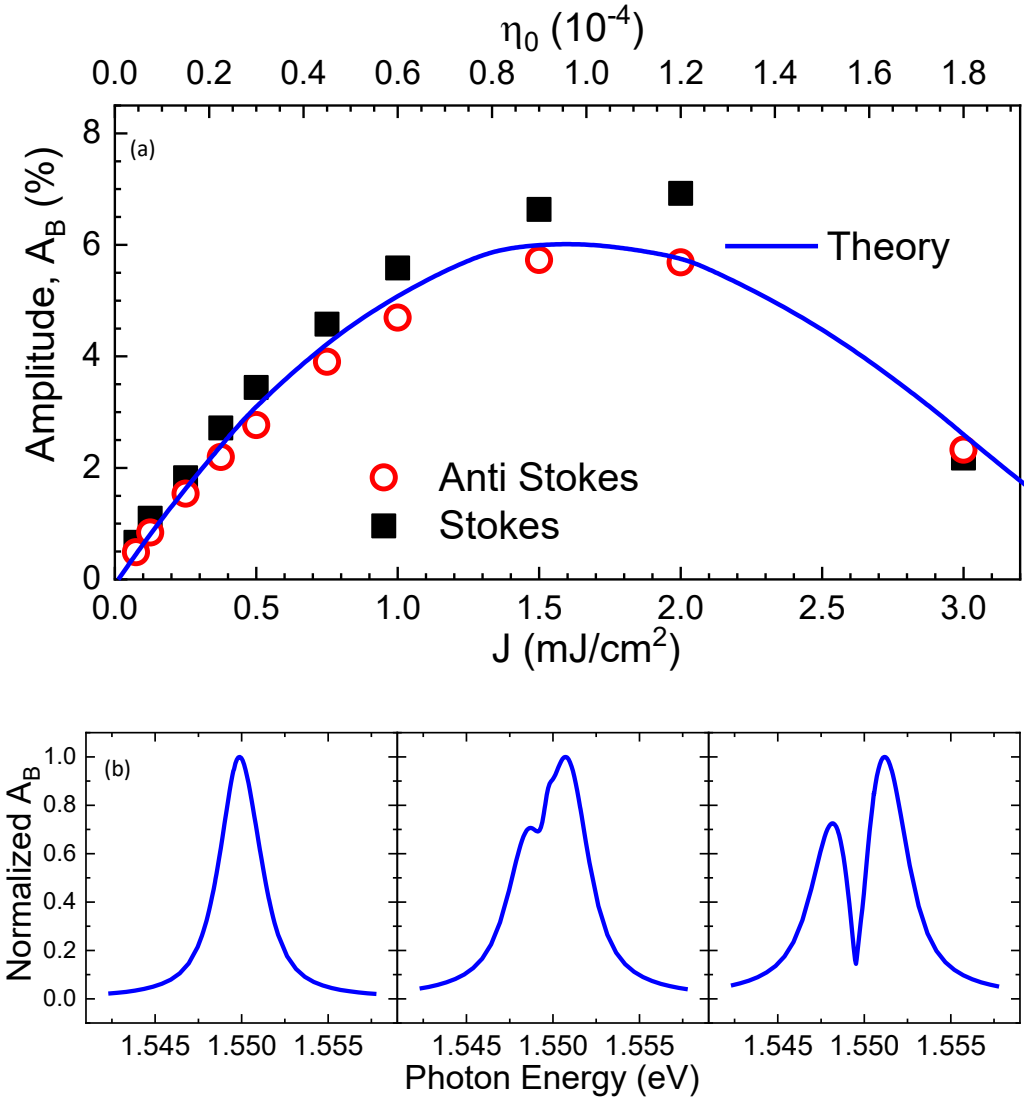

Fig. 3.12 (a) Dependence of the TDBS signal amplitude on the optical excitation density (experimental data, symbols) and the strain pulse amplitude (theoretical calculations, solid line). The experiential errors do not exceed the size of the symbols. (b) dependences of the TDBS signal amplitude on the probe photon energy for three values of J and η_0, respectively. The dependences are normalized to the values at the maxima.

3.5 Conclusions

In conclusion, the giant photo-elastic effect of exciton-polariton in GaAs/AlAs superlattice was presented, that was used for the detection of 42GHz phonons by time-domain Brillouin scattering. The strong dispersion of dielectric permittivity in the vicinity of the polariton resonance causes a pronounced and ultrafast response of optical properties to propagating phonon wave packet in a form of the strain pulse. With the help from our partners, a theoretical model was developed that accurately predicts qualitatively and quantitatively a change in optical reflectivity induced by the propagating phonons that fulfil the Brillouin condition. It is also demonstrated that the high density of phonon flux suppresses the signal amplitude.

The frequency range of detected phonons in presented scheme depends on the speed of sound in the superlattice and its dielectric constant function which defines refractive index for the probe energy as well as position of exciton-polariton resonance. Tailoring these parameters can be done by fine adjustment of superlattice widths of GaAs and AlAs layers or by using alterative materials for creating structures with entirely different position of exciton resonance, for example, II-IV semiconductors. Folded dispersion relation of phonons in periodic structures allows detecting multiple frequencies with the same lattice. In experiments presented in this thesis detection of phonons up to 0.5 THz is achieved.

Implementation of the giant photo-elastic effect of exciton-polariton paves the way for a new range of applications in the field of manipulation of extremely low fluxes of high-frequency phonons. The technique may be used for the detection of phonons emitted by nano-objects as well as for the nanoscopy field of sub-micron objects which demand delicate treatment- like biological tissues.

4

Resonant excitation of magnetization precession in Fe-Ga thin films

In this chapter GHz-frequency optical modulation of the heat is proposed that is transferred into magnons. Manipulation of high-frequency coherent magnons is a promising concept for nano-scale computing (*72*) to carry and process information, also on a quantum level (*73*). Typically, magnons are excited non-thermally by coupling microwave photons with the frequency matching magnetization precession (*36, 74-76*). In the scope of this chapter we exploit alternative approach based on ultrafast modulation of the magnetic anisotropy due to absorption of ultra-short optical pulses (*77, 78*). In ferromagnetic metals, the intrinsic magnon frequency depends on the external magnetic field and may be varied between ~1 and ~100 GHz (*79*), which is a range of modern telecommunications and computing operations. Matching the repetition rate of the optical pulses with the intrinsic frequency of the magnetically ordered system allows resonant magnon excitation with enhancement of the fundamental mode amplitude in a ferromagnetic thin film(*35*). Parameters of excited magnetization precession like its spectrum, lifetime, amplitude, and spatial distribution in the external magnetic field are defined by the properties of used material and the design of the nanostructure (*80*). For this work a thin films Iron-Gallium alloy ($Fe_{0.81}Ga_{0,19}$) was chosen as a harvester of optically induced heat. This metallic material with large net magnetization is prospective material in spintronics, among others, due to its narrow ferromagnetic resonance (*81*).

Initial measurements performed in our group allowed us to characterize the properties of chosen Galfenol thin films with thicknesses of 5 nm and 105 nm. The magnetization easy and hard axis are identified as well as the amplitude and frequency dependence of magnon modes on the orientation of the sample relative to the direction of the external magnetic field and its magnitude. In the established regime, the pump-probe experiments on resonant excitation of the magnetization precession was performed with a 10 GHz repetition rate laser in order to match the magnetization precession frequency and maximize magnetic system response.

4.1 Sample

In resonant excitation of magnetization precession experiments performed within the scope of this thesis, the thin films of Iron- Gallium alloy ($Fe_{0.81}Ga_{0,19}$) are used. This ferromagnetic material has cubic anisotropy, enhanced magnetostriction parameters(*82*), large net magnetic moment and saturation magnetization (*79*) as well as weak dumping. Due to these properties, it became an interesting topic of research in solid-state physics and applied science. Galfenol is body centered cubic symmetry crystal, with gallium atoms randomly substituted in the lattice (see Fig.2.10a). Below Curie temperature, being for GaFe above $T_c \approx 700°C$ (*83*), magnetic moments to align along the easy axis. For Galfenol easy axes lay along the main crystallographic directions, where the free energy density (Eq.2.22) has its minimum (Fig.2.10b). When considering thin films, additionally in plane uniaxial anisotropy is present. Finally, the shape anisotropy contributes to the overall anisotropy of the free energy density, taking the form of a sum of cubic, shape and uniaxial anisotropy discussed in Chapter 2.

In the scope of this thesis, two Galfenol films, one being 5nm thick and the second 105nm thick presented in Fig.4.1 are used. It was grown by magnetron sputtering on a (001) semi-insulating GaAs substrate and covered by a 2-nm Cr cap layer to prevent oxidation.

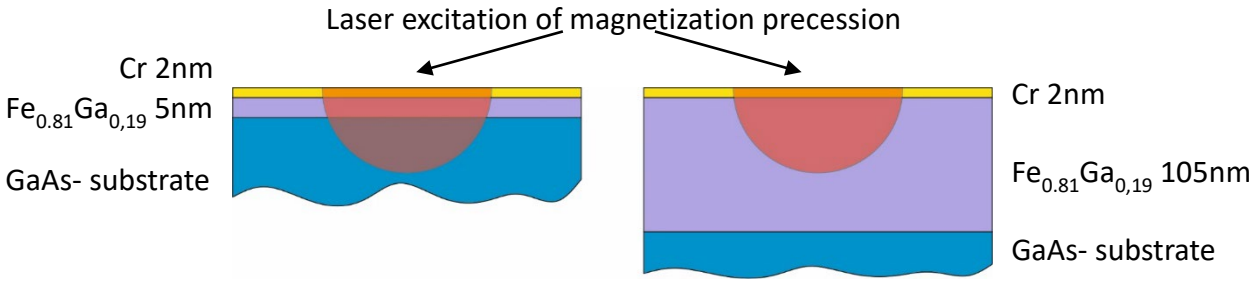

Fig. 4.1 Schematic of the samples used in performed experiments with magnetization precession excited by the laser.

Prior to studies on resonant magnetization precession, the preliminary experiments were run in our group in order to establish a regime for further studies (*28, 37*). Experiments were performed by means of the magneto-optical pump-probe technique with an ASOPS system with two 80MHz oscillators (pulse duration 150fs, wavelength ~800nm) locked with 800Hz offset frequency providing a time-resolved signal with a time window of 12.5ns. One of the goals of these studies was to achieve the highest amplitude of magnetization precession. Excitation of magnons was done via a temperature-related decrease in magnetization anisotropy field and therefore variation of the effective magnetic field B_{eff} which depends on the angle between the crystal structure of the film and the external magnetic field. Hence

measurements on the orientation angular dependence of the frequency and amplitude of the magnetization precession needed to be done. Data is presented in Fig.4.2. It shows that the highest amplitude is obtained for an angle $\varphi = \pi/8$ from [100] crystallographic direction. In Fig.4.2b one can observe 4-fold symmetry due to cubic crystalline anisotropy and slight uniaxial distortion resulting in tilting of the maxima towards $\varphi = \pm\pi/4$ angle. Further studies were performed under $\varphi = \pi/8$ angle.

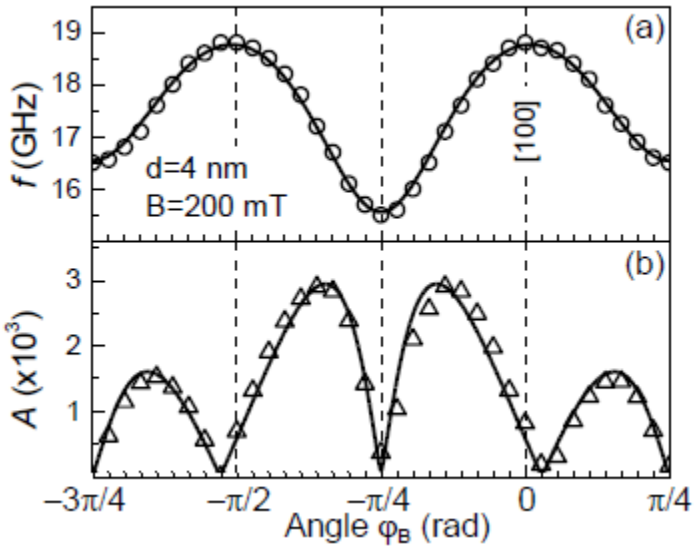

Fig. 4.2 Azimuthal dependences of the precession frequency (a), amplitude (b), in the 4-nm $Fe_{0.81}Ga_{0,19}$ layer in external magnetic field B=200mT. Symbols show the experimental data; solid lines are the calculated dependences.

In thin samples with thicknesses of a few nanometers under single pulse excitation, only ground magnon mode was excited due to uniform excitation by the pump pulse (*37*). Kerr rotation signal of 5nm thick sample magnetization precession in external field B =200mT is presented in Fig.4.3a and its Fourier spectrum in Fig4.3b. In a thick sample of 105nm, one can distinguish several modes being excited due to inhomogeneous excitation at the surface of the film. Data presented inf Fig4.3c show the time evolution of such signal. Fourier transform of the signal shown in Fig.4.3d is performed for two time windows one from the 0-4 ns and the second one in the time window 0.6-4.6 ns showing that the ground mode has the highest amplitude and the longest lifetime.

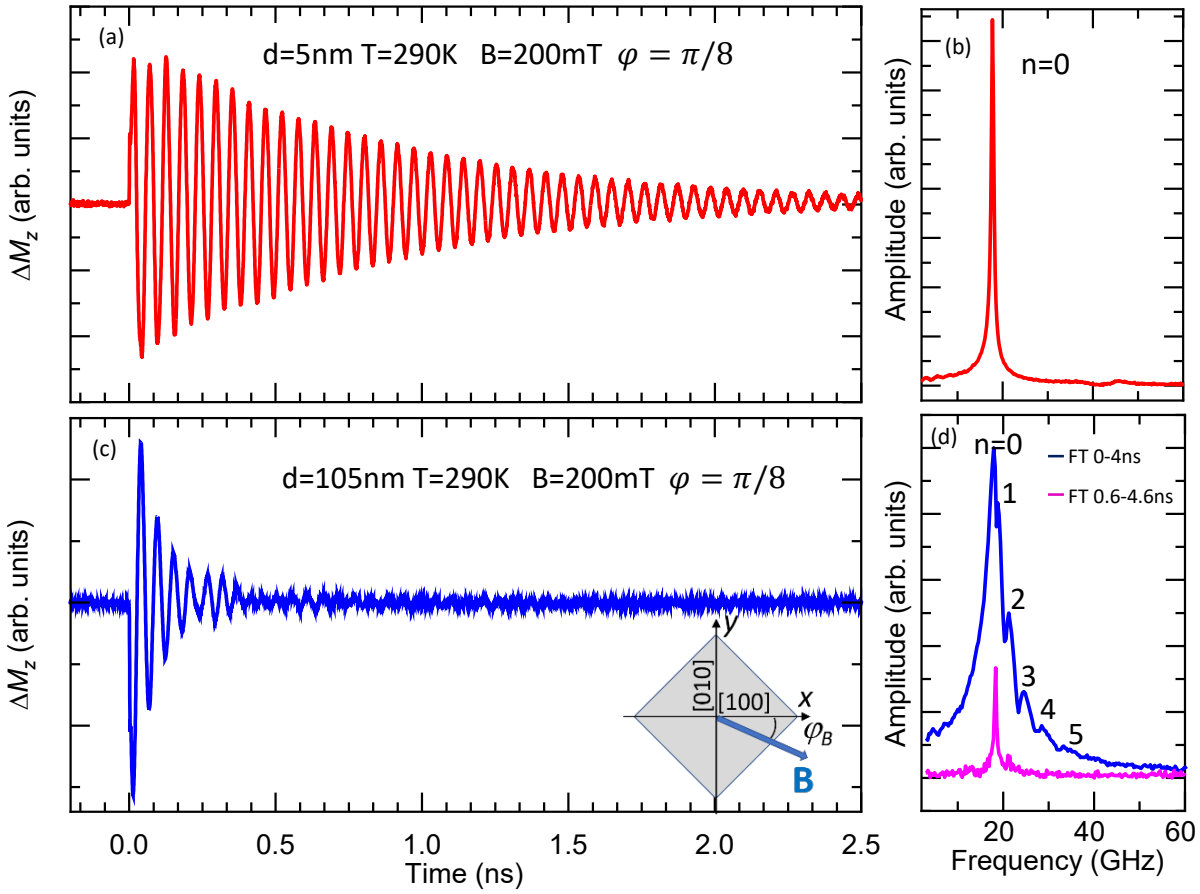

Fig. 4.3 Kerr rotation measurements performed at T=290K, B = 200 mT and φ=π/8. (a) Single-mode magnetization precession temporal evolution in 5nm thick sample (b) corresponding Fourier spectrum (c) Multi-mode magnetization precession temporal evolution in 105nm thick sample (d) Fourier spectra for two different time windows.

The Fourier transform of the signals obtained for several values of external magnetic field B are presented in Fig. 4.4a. The frequency of thermally excited magnetization precession in the studied sample is determined by the external magnetic field B and the magnon wave vector q and was discussed in Chapter 2. The dependences $f(B)$ of the fundamental magnon mode were calculated for $\phi_B = \frac{\pi}{8}$ and are presented in Fig. 4.4b for $\Delta T = 0\ K$ (blue curve) and $\Delta T = 200\ \mathrm{K}$ (red curve). The circles represent experimental values.

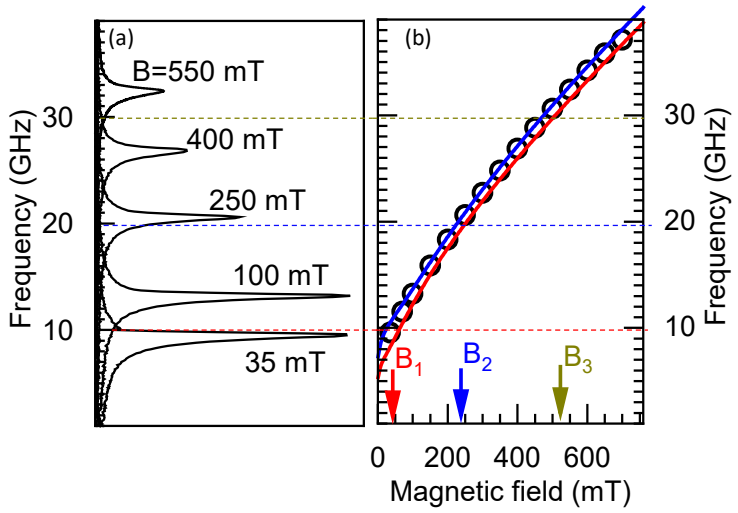

Fig. 4.4 (a) Fast Fourier transform spectra showing the fundamental magnon mode for several values of the magnetic field B. (b) The field dependence of fundamental magnon mode frequency, f(B) for the 5-nm thick $Fe_{0.81}Ga_{0.19}$ energy harvesting layer. Symbols show f(B) obtained by fast Fourier transformation of Kerr rotation signals measured in a single pulse pump-probe experiment. Solid lines are calculated with dependencies for ΔT=0 K (upper curve) and ΔT=200 K (lower curve). The dashed horizontal lines show the frequencies of the harmonics in the temperature modulation spectrum induced by the 10 GHz optical excitation. The vertical arrows indicate the expected resonances for the fundamental magnon mode at these harmonics.

These preceding measurements of high-frequency magnetization precession dependencies for two thicknesses of the samples, magnetic field and the angle relative to external magnetic field allowed us to set an experimental regime and continue studies on resonant magnetization precession in Galfenol samples with 10 GHz laser.

4.2 Experimental technique

The magneto-optical pump-probe experimental set-up is presented in Fig.4.5. In our experiment, Asynchronous Optical Sampling (ASOPS) with two resonators is used. As a probe laser, we use 1GHz GigaJet Twin Ti-Sapphire Oscillator by Laser Quantum with a maximum power of 700 mW and variable wavelength ranging from 750 nm to 850 nm. In our studies, wavelength $\lambda_{probe} = 760$ nm is used. For the pump, Taccor x10 with wavelength $\lambda_{pump} = 800nm$ is used, with repetition rate of 10 GHz and power up to 1 W. The pulse duration for both oscillators is around 50 fs. Lasers are synchronized electronically by TL-1000-ASOPS unit with the o ffset frequency of 2 kHz between probe as a maser laser and pump being a slave. The pump beam is guided through a neutral density filter (ND) for adjustment of the excitation density and through polarization optics and then it is focused with 15x Newport gold-coated reflective microscope objective (MO1) down to 8μm on the sample placed between the magnet poles providing uniform horizontal magnetic field. The probe beam is guided similarly to the pump, its power and polarization are adjusted by a set of lambda half-wave plate (λ/2) and a Glan prism (GP). A linearly polarized probe goes through another slot of the same microscope objective (MO1) and is focused to a slightly smaller spot than a pump ~6 μm. There are two detection schemes implemented in this experimental setup. Reflection geometry for detection Magneto-optic Kerr effect (MOKE) and transmission geometry for detection of Faraday rotation of probe signal. In both cases pump beams are blocked and additionally filtered by a short pass filter, ensuring that only probe is detected. The probe beam then is split at the Wollaston prism providing splitting of the polarization into two beams separately focused by lenses (L2, L3) on the detectors of balanced photoreceiver (BPR) manufactured by New Focus, model 2107. After differentiation, the signal is filtered by a variable bandpass filter ranging from DC to MHz range, then the signal is electronically amplified (GAIN) in gain ranging between 1 and 10000. All measurements in this thesis's scope were done at x1000 gain. Finally, the signal is synchronized with the trigger and digitalized by PCI express digitizer card manufactured by GaGe Applied Technologies, model Razor Express 14X2 CompuScope, integrated with ASOPS system by Laser Quantum.

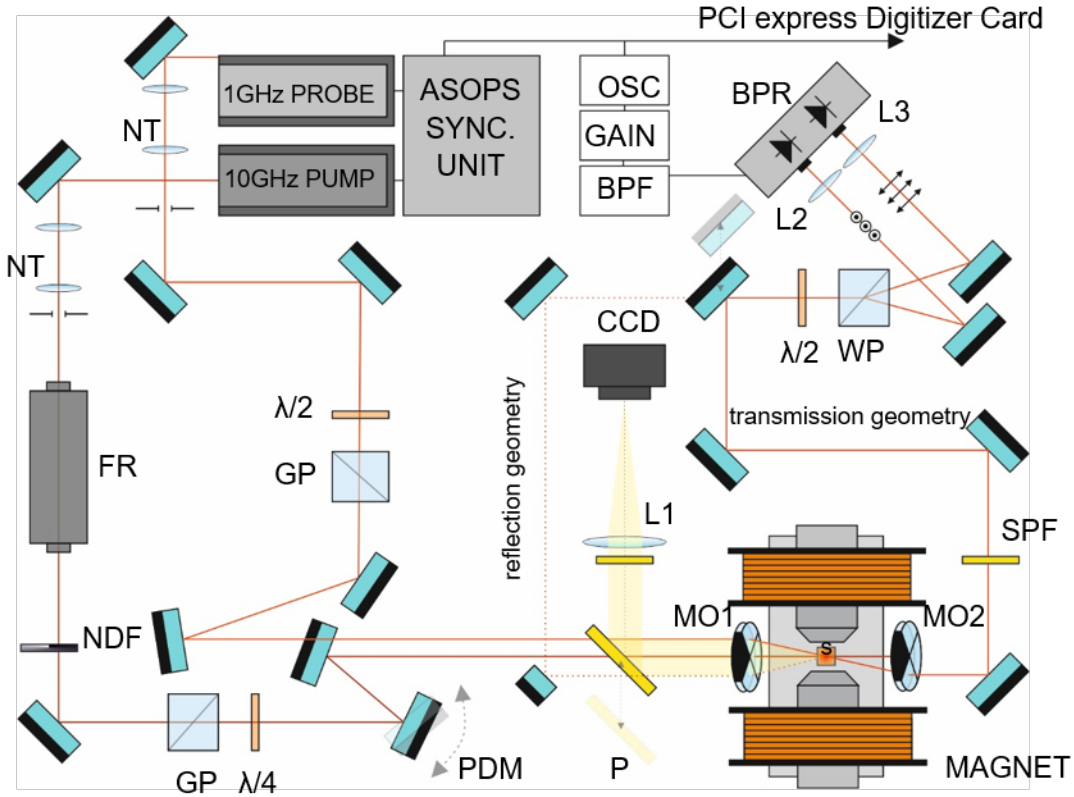

Fig. 4.6 Experimental set-up for excitation and detection of magnetization precession and propagation of spin waves realized in both, reflection and transmission geometry. NT-newton telescope for beam collimation, FR- Faraday rotator for filtering light reflected back towards the laser, NDF-neutral density filter for excitation density adjustment, polarization optics: GP- Glan prism, λ/2 - lambda half wave plate, λ/4 – lambda quarter wave plate, PDM- Piezo driven mirror for realizing displacement between pump and probe, P- pellicle and CCD- CCD camera for visualization, MO- microscope objective, SPF- Short pass filter for filtering, L- lens, WP-Wollaston prism for splitting horizontal and vertical polarization, BPR- balanced photo-detector, BPF- band pass electronic filter, OSC- oscilloscope.

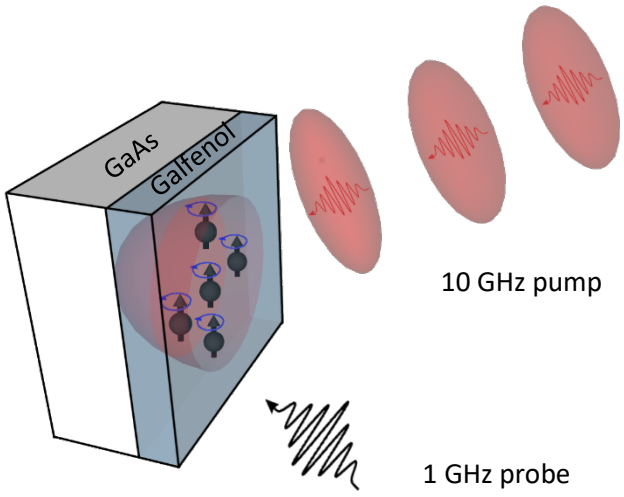

Fig. 4.5 Schematics of excitation and detection of magnetization precession Galfenol thin film of 5 nm. 10 GHz pump pulses excite uniform magnetization precession, which by the means of Kerr Rotation Angle measurements is detected.

4.3 Resonant excitation of magnetization precession in 5nm Galfenol film

Measurements of resonant excitation of magnetization precession were performed by measuring out of plane magnetization projection δm_z via Kerr rotation angle Θ of reflected probe beam from 5 nm thick $Fe_{0.81}Ga_{0,19}$ sample in the function of the magnetic field B.

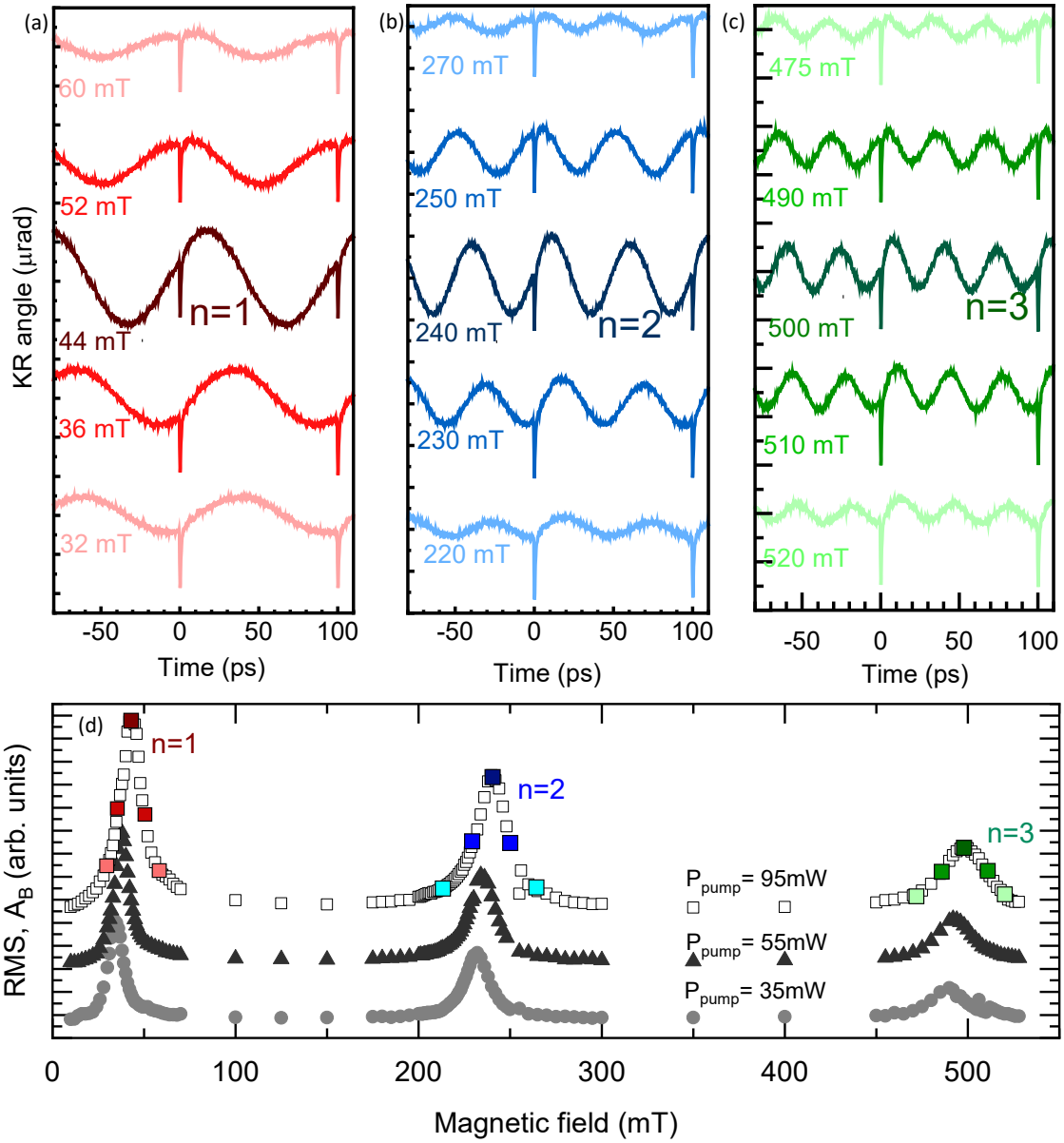

Fig. 4.7 (a),(b),(c) Kerr rotation signal in vicinity of magnetization precession resonance n=1,2,3 respectively (d) Measured magnetic field dependences of the root mean square (RMS) amplitude of the Kerr rotation signal, A_B , for three values of pump excitation power

Probe power $P_{probe} = 1\ mW$ was kept constant, signals were measured for pump powers P_{pump} varying in the range between 35 mW and 150 mW. Kerr rotation signals for $P_{pump} = 90\ mW$ are presented in Fig.4.7 a, b and c. Amplitude of Kerr rotation angle in the function of the magnetic field is presented in Fig. 4.7d. Times $t = 0$ ps and $t = 100$ ps are corresponding to the arrival time of the pump pulses, which are featured by peaks visible in the signal. The mechanism in this experiment utilizes periodic thermal modulation for exciting magnetization precession which can be treated as a harmonic oscillator with eigenfrequency f, tunable by magnetic field B. The signals measured in the vicinity of the first resonance (n=1) have a harmonic shape. It is possible to fit them with a sine function $\delta m_z = A_B \sin(\omega_1 + \varphi_B)$, where $\omega_1 = 2\pi f_1$, and A_B and φ_B are magnetic dependent amplitude and phase of the harmonic oscillations. One can see that the amplitude A_B reaches its maximum at $B = 44$ mT which corresponds to first resonance $f = 10$ GHz.

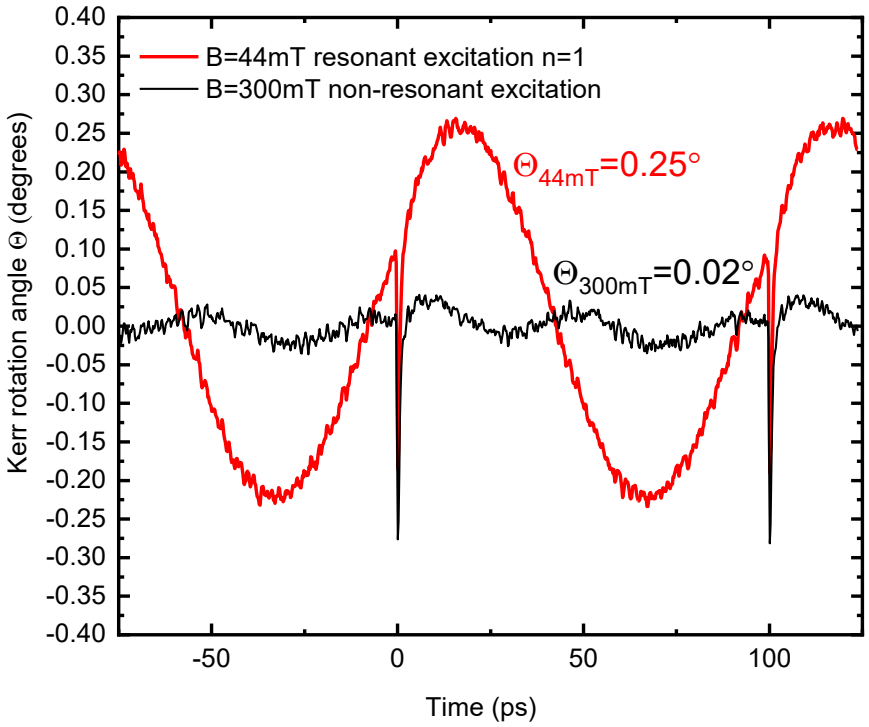

Fig. 4.8 Kerr rotation signal for resonant case $B = B_1 = 44mT$ and non-resonant case $B = 300mT$

Away from the resonance signal is periodic, but not harmonic, the amplitude is significantly smaller and the temporal shape is not possible to fit with a single sine function. In Fig.4.8 resonant signal at $B = B_1 = 44mT$ is compared with the signal obtained away from the resonance at $B = 300$ mT. It is seen that the

amplitude of the Kerr rotation angle in the resonant case is $\Theta_{44mT} = 0.25°$, which is a 12-fold increase compared with non-resonant excitation.

In the vicinity of the resonance the phase shifts from $\varphi_B = -\pi/2$ for $B < B_1$ to $\varphi_B = \pi/2$ for $B > B_1$, while at resonance $\varphi_B \approx 0$ (Fig.4.9b) Similar behaviour is observed in the vicinity of the second resonance $f_2 = 20\ GHz$ and the third resonance $f_2 = 30$ GHz . The amplitude of the oscillations at $B_2 = 250$ mT and $B_3 = 500$ mT are also local maxima (though smaller than for the first resonance). The phase and amplitude have similar field dependence to the first resonance.

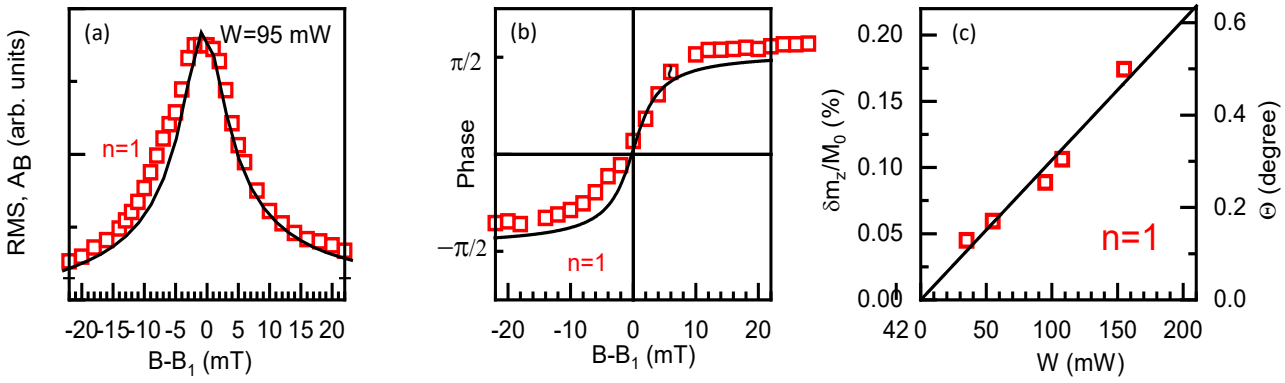

Fig. 4.9 Amplitude (a), and phase (b) of KR signal in vicinity of magnetic field related with 10 GHz magnetization precession frequency matching repetition rate of the laser. (c) KR amplitude dependence on the excitation pump power.

With the increase of pump power, one can see a linear increase of the amplitude of magnetization precession. This is seen in the dependence shown in Fig.4.9c. It is related to the increase of temperature fluctuations amplitude δT of the lattice induced by the pump. Additionally, the values of measured resonance fields B shift to slightly higher fields when pump power increases, which can be seen in Fig.4.7d. The explanation is that increase of background temperature ΔT induces a decrease of the magnon frequency and respectively increase of the magnetic field value required for the fulfilment of resonance conditions.

4.4 Periodic excitation of magnetization precession in 105 nm Galfenol film

Another set of measurements was performed on a 105 nm thick $Fe_{0.81}Ga_{0,19}$ sample with $P_{pump} = 140\ \mathrm{mW}$. Due to the small penetration depth of the pump in comparison to the size of the sample (see Fig.4.1) higher odd and even modes can be excited. This results in broadening of the magnon spectrum and a corresponding dephasing of the magnetization precession. It has a destructive effect on magnetization precession amplitude when in addition to fundamental modes, higher orders (n=1-5) are excited. The non-harmonic character of the thermally driven oscillations in the Kerr Rotation signal is seen in Fig.4.10a. The magnetic dependence presented in Fig.4.10b shows several broad peaks overlapping with each other. The maximum amplitude A_B of the oscillations is 15 times smaller than it is in the thin sample when only the fundamental mode is excited.

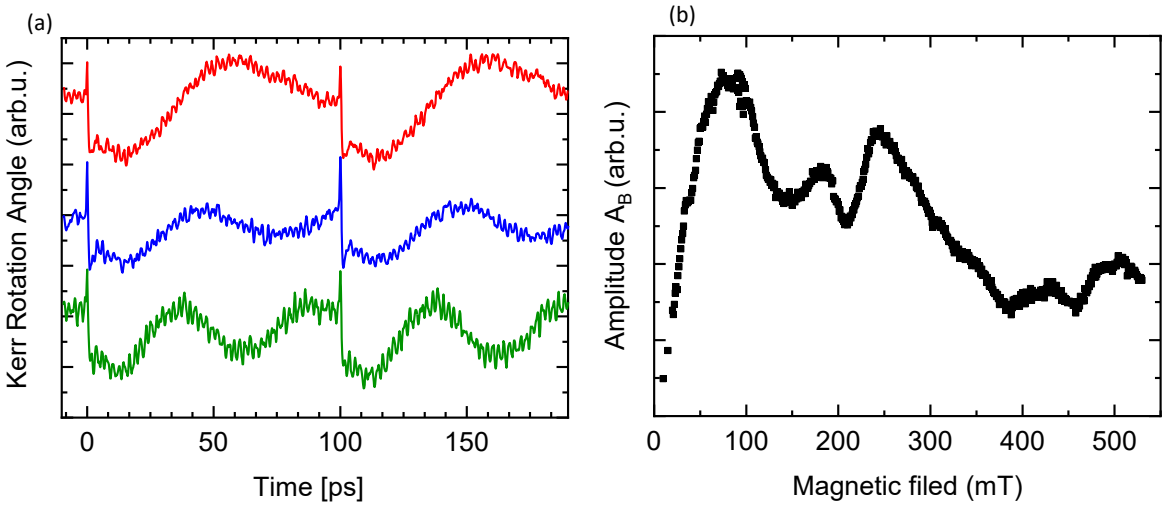

Fig. 4.10 (a) Kerr rotation signal for various values of magnetic field (from the top: red-76 mT, blue-175 mT, green-250 mT), (b) Amplitude of Kerr rotation signal in a function of the applied external magnetic field

4.5 Theory

4.5.1 Galfenol parameters of free energy density

In performed experiments on 5 nm thick sample, the main mechanism responsible for magnetization precession is thermal modulation of the magnetic anisotropy parameters (*28*). In presented analysis based on previous experiments, we do not take into account other mechanisms like thermal strain or the effect of thermal gradients inside the ferromagnetic film which can induce ac-spin transfer. In discussed experiment, the temperature gradient is estimated to be about 4%. Due to uniform in-plane magnetization in examined film, this transfer does not produce a torque on the magnetization, hence we can neglect it (*84-86*). The impact of the thermal modulation of the magnetocrystalline anisotropy is also confirmed by the measurements of magnetization precession amplitude dependence on the direction of the external magnetic field presented in Fig.4.2, which demonstrates a four-fold in-plane symmetry with modest uniaxial contribution, which corresponds to the magnetocrystalline anisotropy of $Fe_{0.81}Ga_{0,19}$ film. The magnetization precession is induced by temperature modulation that changes B_{eff} through temperature-dependent parameters of free energy density F_M: M_0, K_1 and K_u discussed in Chapter 2. In the temperature range of our studies, their dependence is linear (*82*) and it is a sum of its room temperature value and thermal coefficient $\beta_X = \frac{\partial X}{\partial \mathrm{T}}$: $X = X^{RT} + \beta_X(T - T_0)$, where *X* =$M_0$, K_1, K_u. The room temperature values of the parameters $M_0^{RT} = 1.95$ T, $K_1^{RT} = 20$ mT, $K_u^{RT} = 9$ mT, and temperature coefficients $\beta_M = -0.97$ mT/K, $\beta_{K1} = -0.046$ mT/K, $\beta_{Ku} = -0.025$ mT/K, can be obtained by fitting experimental data obtained from single-shot excitation experiments. Fitting experimentally obtained frequency and amplitude dependence on angle between the external magnetic field and crystallographic orientation of the sample presented in Fig.4.2 as well as frequency dependence on magnetic field presented in Fig.4.4 allow to extract room temperature values for the abovementioned parameters(*28, 37*). Gilbert damping α_0 can be obtained from the decay time of oscillatory signal of magnetization modes.

4.5.2 Higher order modes excitation

Due to the finite laser spot size, the thermal modulation gives rise to magnons with non-zero in-plane wave vectors, $q_{||}$ and with finite tangential wave vector $q_{\perp}$. The range of in-plane magnons excited by the laser can be obtained from the Fourier transform of the Gaussian distribution of the laser intensity. Therefore, one gets $0 \leq q_{||} \leq \frac{4}{r}$, where r is the laser spot radius. In our case with $r = 8.5$ μm the upper

limit is $q_{||} \leq 4700\,\mathrm{cm}^{-1}$. This range corresponds to magneto-static spin waves with a nearly flat dispersion relation determined by the magnetic dipole-dipole interaction. In the case of a thin ferromagnetic film of thickness h, where $\frac{q_{||}\mathrm{h}}{2\pi} \ll 1$ it can be written in a simplified form as (*54*):

$$f_{q_{||}} = f + \frac{\gamma_0}{2\pi} v q_{||} h \tag{4.1}$$

Where h is film thickness, v is the dispersion coefficient determined by the main parameters of the ferromagnet: M_0, K_1 and K_u. For the studied Galfenol layer its value at room temperature is $v \approx 3.8\,\mathrm{T}$ (*54*) and in our experiment, the frequencies of the thermally driven magnons with finite in-plane wave vector do not exceed 270 MHz (*87, 88*). This value is significantly smaller than the spectral width of the fundamental mode of magnetization precession (0.5 GHz) determined by its decay time. Thus, the thermally driven magnons with finite in-plane wave vectors may be considered degenerate.

The spectrum of magnons with finite tangential wave vector, $q_\perp$, is quantized due to spatial confinement along the layer normal: $q_{\perp,n} = \frac{\pi n}{h}$, where *n*=1,2,3… In a film with nanometer thickness, the corresponding dispersion is determined by the exchange interaction and in a simplified form can be expressed as:

$$f_n = f + \frac{\gamma_0}{2\pi} \varrho D q_{\perp,n}^2 \tag{4.2}$$

where ϱ is a field dependent coefficient approaching 1 with increasing B (*54*) and D is the spin stiffness constant. In the analyzed Galfenol layer with $h = 5\,\mathrm{nm}$, as a consequence of the large penetration depth of the laser pulse in comparison with the layer thickness, the thermal distribution along the normal to the layer is uniform. Therefore, the odd magnon modes (*n*=1,3,5) cannot be excited. In such a case, the lowest higher-order mode, which can be generated by thermal modulation, corresponds to *n*=2. For the Galfenol spin stiffness $D = 1.5 \times 10 - 17\,\mathrm{Tm}^2$ (*54*), the frequency of this mode exceeds the ground mode frequency by more than 500 GHz. Due to the very small amplitude of such high-frequency harmonics in the thermal spectrum (see Fig.4.11b), this mode and other higher-order even modes are not excited. Thus, in the studied layer of 5 nm thickness, the fundamental magnon mode is solely driven by the modulated heat. In the film with 105 nm thickness, due to the small penetration depth of light, we observe excitation of higher modes.

4.5.3 Modelling of heat transport for periodically pulsed optical excitation

For a qualitative description of observed phenomena our partners, Prof. Vitalii Gusev from Le Mans University, Dr. Serhii Kukhtaruk, and Dr. Tetiana Linnik from V.E. Lashkaryov Institute of Semiconductor Physics from Kiev, developed the one-dimensional two-temperature model for the lattice heating temperatures of the film, T_f, and the substrate, T_s:

$$c_f \frac{\partial T_f}{\partial t} - \kappa_f \frac{\partial^2 T_f}{\partial z^2} = F_p A_f g(t) \frac{dS}{dz} \tag{4.3}$$

$$c_s \frac{\partial T_s}{\partial t} - \kappa_s \frac{\partial^2 T_s}{\partial z^2} = F_p A_s g(t) \frac{dS}{dz} \tag{4.4}$$

where c_j, κ_j, and A_j are the heat capacity, thermal conductivity, and fraction of absorbed optical energy relative to the incident excitation energy (further referred to as absorption coefficients), respectively ($j = f, s$). The pump laser pulse fluence $F_p = 2W/(f_0 \pi r^2)$, where W is the average laser power, $f_0 = 10$ GHz is the laser repetition rate, and r is the radius of the pump spot defined by $1/e^2$ of the intensity. The function, $g(t) = \frac{2}{\tau_p}\sqrt{\frac{2}{\pi}} \sum_{n=1}^{\infty} \exp\left(-2\frac{\left(t-\frac{n-1}{f_0}\right)^2}{\tau_p^2}\right)$, describes the temporal evolution of the laser pulses with duration, τ_p, and repetition rate, f_0.

The example of the average lattice heating temperature of the film $\bar{T}_f = \int_0^h \frac{T_f dz}{h}$ for $W = 95$ mW, $r = 8.5$ μm is shown in Fig.4.11a. One can see that the temperature oscillates with the excitation frequency $f = 10$ GHz around a slowly increasing background. The calculations show that in the discussed one-dimensional (1D) heat transport problem the background temperature does not reach a stationary value but, diverges with time. However, as one sees in Fig.4.11b, the amplitude of thermal oscillations, δT, converges very quickly. It is due to the three-dimensional nature of heat diffusion in our sample, which finds its equilibrium with pump heating at some stationary background temperature ΔT to estimate it, our partners have solved analytically the stationary 3D heat equation for T_s.

Taking into account that the optical excitation energy is absorbed in a layer with a thickness much less than the radius of excitation at the surface, we may assume that the thermal source is located at the interface (*z*=0). Then the equation and boundary condition may be written as:

$$\left(\frac{\partial^2}{\partial x^2} + \frac{\partial^2}{\partial y^2} + \frac{\partial^2}{\partial z^2}\right) T_s = 0 \tag{4.5}$$

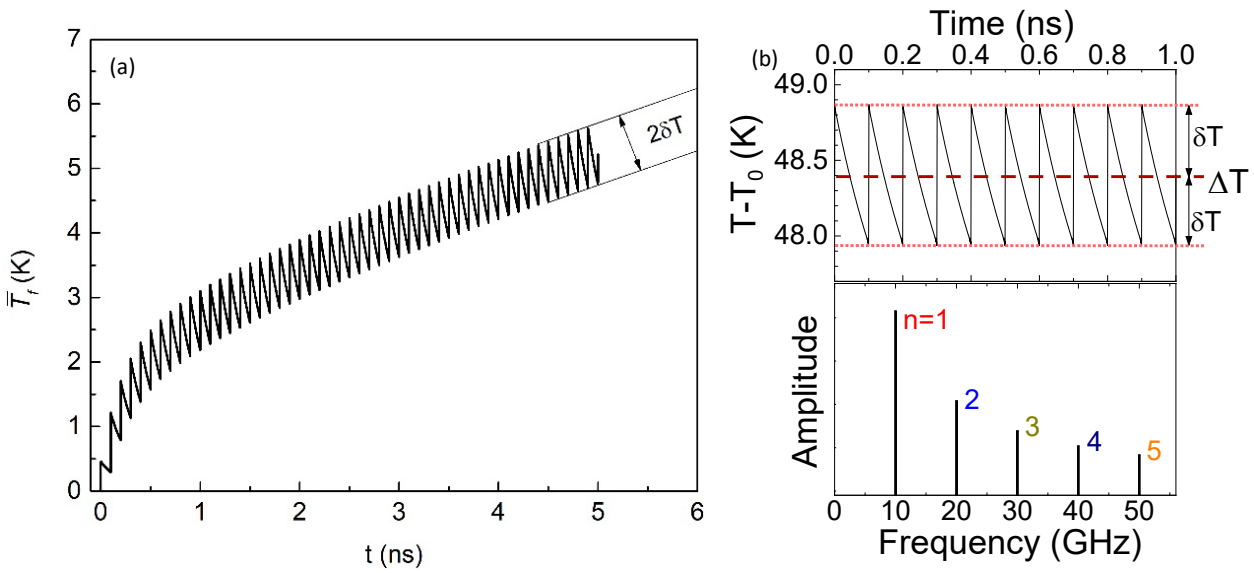

Fig. 4.11(a) The temporal evolution of the average temperature $T_f(t)$ for periodic laser pulse excitation with average power W=95 mW incident on the FeGa film with a thickness h=5nm deposited on the GaAs substrate. (b) Calculated temporal evolution of the $Fe_{0.81}Ga_{0.19}$ lattice temperature induced by the 10 GHz optical excitation of the $Fe_{0.81}Ga_{0.19}$/GaAs heterostructure at the pump excitation power W=95 mW (upper panel) and its Fourier spectrum (lower panel).

and

$$\kappa_s \frac{\partial T_s}{\partial z}|_{z=0} = (A_f + A_s)\, I\, exp\left(-2\frac{x^2+y^2}{r^2}\right) \tag{4.6}$$

here I is the laser intensity which is related to the laser power by

$$W = I \iint_{-\infty}^{\infty} exp\left(-2\frac{x^2+y^2}{r^2}\right) dxdy = I\frac{\pi r^2}{2}. \tag{4.7}$$

The analytical solution of these equations at *z*=0 and at the center of the laser beam (*x*=*y*=0) reads

$$\Delta T = \frac{(A_f + A_s)W}{\sqrt{2\pi}\kappa_s r} \tag{4.8}$$

For optical excitation of the film (absorption length smaller in the metal than in the substrate) we have $T_f > T_s$ because of the boundary resistance. Estimations show however that the jump of temperature at the interface is ten times smaller than the T_s Thus, the effect of the temperature jump can be neglected. We also derive the background temperature Δ*T* from the measured dependences of the resonance fields of B_1, B_2 and B_3 on excitation pump power W. For this, we take the derivatives *dB/dW* from the

experimental data in Fig. 4.7d and compare them with the calculated theoretical derivatives dB/dT . As a result, we get the values for *dT/dW=(dB/dW)/(dB/dT)* for the three resonant frequencies 10, 20 and 30 GHz. The results are presented in Table 4.1.

Table 4.1 Theoretical values for resonant magnetic field for various excitation powers (top), derivatives of resonant magnetic field on excitation powers and temperatures and temperature on power (middle) and comparison between calculated values of background temperature raise and values obtained from the experiments (bottom).

Power (mW)	Resonant Fields (mT)		
	10 GHz	**20 GHz**	**30 GHz**
35	34	232	490
55	38	234	492
95	42	240	498

derivatives	**10 GHz**	**20 GHz**	**30 GHz**
dB/dW (mT/mW)	0.13	0.13	0.13
dB/dT (mT/K)	0.19	0.13	0.16
dT/dW (K/mW)	0.7	0.9	0.7

Power (mW)	ΔT (K)	
	Calculated	**Extracted from experiment**
35	18	28±2
55	28	44±3
95	48	77±5

The average value for $\frac{dT}{dW} = 810 \pm 50$ K/W. The estimated temperature rises $\Delta T = (dT/dW)W$ for the three values of W are presented in Table 4.1 and compared with the theoretical values. The difference between the values calculated and extracted from the experiments is less than 40%. This difference may be due to additional heating by the probe which is not included in the theoretical calculations.

4.6 Conclusions

In conclusion, the resonant excitation of magnetization precession with 10GHz laser modulated heat is demonstrated. The amplitude of the fundamental mode oscillation was enhanced by order of magnitude when the intrinsic frequency of the system was tailored to match the excitation frequency. The resonant behaviour was also observed for higher harmonics of the excitation- 20 GHz and 30 GHz. The theoretical model developed with our partners estimates that temperature fluctuations are on the level of ~0.1 K, while the whole system remains stable and maintains studied properties independently on background temperature.

From practical point of view, it is crucial to achieve high efficiency of energy transformation from optically modulated heat to magnons. The efficiency is determined by the ratio of magnetization precession angle Θ to injected power W to the system. In our experiment, the efficiency is approx. $\Theta/_W = 2.5°/\mathrm{W}$, which is only one order of magnitude less than achieved in conventional microwave devices (*89*) and similar to efficiency when utilizing surface acoustic waves for spin pumping(*90*). Up to maximum power used in scope of this thesis, the magnetization precession remained harmonic with no sign of non-linearity affecting transformation efficiency. There is present temperature-induced nonlinearity which shifts the resonant frequency of the system depending on the background temperature. However, it remains rather insignificant; for instance, at second resonance (n=2) the 20% change in background temperature resulted only in 3% change in amplitude of magnetization precession. Thus, such a concept can be considered stable in wide range of temperatures.

There is a room for further improvement of the conversion of optical pulse energy to coherent magnons by choosing different parameters of the structure and materials, for optical excitation, shorter penetration length and smaller heat capacities of the ferromagnetic layer increase modulated temperature amplitude and in consequence the $\Theta/_W$ efficiency. Modulated temperature to the background temperature ratio increases with the decrease of layer thickness and thermo-conductivity of the substrate. It is possible to implement multilayer structure which would support escape of background heat and confine high-frequency temperature oscillations in vicinity of the ferromagnetic thin film. The excitation of magnons up to 30 GHz is demonstrated in this work, however it is possible to modulate temperature and magnetization precession in the metals even with higher sub-THz frequencies (*37, 90*).

In performed experiments the precession angle is approx.. $\Theta = 0.25°$ and generated ac-induction at level of ~1 mT which is large enough for prospective spintronics applications: detection of spin currents by spin pumping (*90, 91*); manipulating single spin states of NV- centers in nanodiamonds by microwave magnetic fields (*92*); excitation of propagating spin waves in magnonic devices (*93*). Therefore, concept of resonant excitation by heat can be considered as a prospective method for sub-THz magnon modulation in ferromagnetic layers, which also can be achieved by optical means.

5

The miniaturization of pump-probe experimental technique by implementing semiconductor Mode-Locked Laser Diodes (MLLD)

Motivation for miniaturization of various devices, including experimental set-ups is quite straightforward, smaller means lighter, cheaper, less resource consuming, more energy-efficient, portable, and easier to integrate. Miniaturization often paves the way for new applications, wider use, and further development in new directions. It is no different in the case of optical set-ups for generation, detection, and manipulation of collective excitations like phonons and magnons. The great limitation in finding applications for such excitation and detection schemes, and their integration outside the optical laboratory is the laser system necessary for their operation. The state of art lasers which are suitable for control of collective excitations are highly complex systems with extensive dimensions and high prices. The most important parameters of such lasers which limit their applicability are wavelength, power, divergence, duration of the pulse, and repetition rate of the light source. However, recent developments in the semiconductor laser field have allowed it to reach characteristics comparable with its bulky and complex counterparts (*11, 12*). Up-to-date passively mode-locked laser diodes (MLLD) provide pulses below 1 ps, high repetition rates in the GHz regime (*13*), and average powers up to 200 mW (*14*) as well as a wide range of wavelengths, which is sufficient for the generation and detection of high-frequency collective excitations. It is of interest to the community to develop a portable set-up based on the semiconductor lasers with the elements integrated on a photonic chip (*94*), which would be suitable for its outside lab applications. In present chapter, the first step is taken toward such a device by using miniaturized 16 GHz repetition rate MLLD to obtain the generation and detection of a coherent phonon wave packet in a form of a strain pulse in an Al transducer.

5.1 Semiconductor Lasers

The physical principle responsible for the laser action was established in already in 1917 by Albert Einstein, in his work On the Quantum Theory of Radiation, in which he set the concept of probability coefficients for absorption, spontaneous emission, and stimulated emission of electromagnetic radiation. It was confirmed years later and led to the development of the first working solid-state laser in 1960 based on Ruby crystal. Three years later first semiconductor laser operation was achieved, but it was operational only in cryogenic conditions- therefore, not very useful for applications. Further development in the field has provided a wide range of lasers with various parameters and applications. To achieve stimulated emission to surpass other undesired mechanisms- absorption and spontaneous emission, the system has to have population inversion, where more electrons are at the excited state than at the ground state. In order to achieve that, various mechanisms are used, it is called pumping of the laser. It can be done optically (like in the widely used pulsed Ti: Sapphire lasers) or it can be done electrically like it is commonly done in semiconductor lasers presented in this part of a thesis.

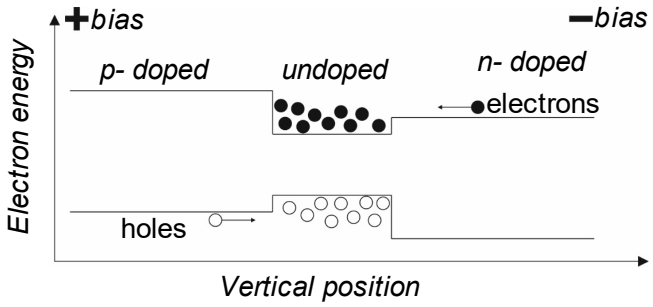

Fig. 5.1 Double heterojunction of semiconductor laser

In this type of laser, energy levels are created thanks to the energy gap between the valence band and conduction band of the semiconductor. Early-stage semiconductor lasers were simply achieving inversion by creating a p-n junction, which is a stack of positively and negatively doped material, resulting in the overpopulation of the electrons on the negative side of the interface. In equilibrium, however, charge carriers recombine spontaneously in this region and there is no population inversion in the active area. To achieve that, a forward bias is applied which constantly drives electrons towards the junction. This process in a single heterojunction is unfortunately very inefficient, due to the low recombination probability of electrons further from the junction. To increase the probability of stimulated emission, a potential well is needed, creating double heterojunction (Fig.5.1). Over the years of progress in a field,

methods of growing precise semiconductor nanostructures were developed and this allowed room temperature operation of the semiconductor lasers, the structure that was initially used and still is a popular solution was GaAs quantum well sandwiched between n-doped and p-doped AlGaAs structures. Such spatial confinement together with electrical pumping allow efficient laser operation. Semiconductor lasers are nowadays the most produced type of laser finding applications in various industries like communication, optical data storage, metrology, spectroscopy etc. For manipulation of high-frequency collective oscillations like phonons it is beneficial to obtain pulsed laser operation with matching repetition rate, which recently became possible by developing passively mode-locked laser diodes.

5.1.1 Passive mode-locking

Mode-locking is the process that results in the periodic pulsed operation of the laser. Phases of the longitudinal modes of the laser can be synchronized. For a sufficient amount of the synchronized modes, they achieve periodic constructive interference. Laser supports amplification of particular frequencies which fulfil condition $n\lambda/2 = L$ where L is the length of the cavity and n is an integer. To perform stimulated emission these longitudinal modes ought to have energy within the gain spectrum of the active medium. Depending on the length of the gain medium and spacing between the longitudinal modes it is possible to launch laser pulses with specific pulse duration and repetition rate. To achieve mode-locking one can utilize active modulation of the gain or the losses of the laser or it can be done passively. In passive mode-locking, modulation of the losses can be achieved by the addition of a saturable absorber. The advantage is that it can be made of the same material as the gain medium and the properties of the section can be tailored by its size and biasing conditions. The forward bias of gain section provides gain and the reverse bias of the saturable absorber modulates the losses. When a sufficient amount of light is absorbed, it saturates and becomes transparent for the rest of the pulse. When light travels through the gain section, the front of the pulse gets amplified and the carriers are depleted for the trailing part causing resonant shaping of the pulse. Proper tailoring of gain and saturation sections creates a narrow window of positive gain leading to pulsed emission.

5.2 Passively mode-locked laser device (MLLD) with 16GHz repetition rate

Here we present semiconductor laser device with parameters suitable for excitation and detection of high frequency coherent excitations. It was fabricated at Glasgow University by the metal organic chemical vapor deposition method (MOCVD). The active medium is based on two 4.4 nm quantum wells (QW) of $In_{0.18}Ga_{0,82}As$ separated by a 9 nm thick barrier of $Al_{0.2}Ga_{0.8}As$. Gain medium emits wavelengths around 930 nm and it is sandwiched between graded-index AlGaAs layers for optical confinement. The active medium is grown between p-doped and n-doped claddings, which together with forward bias provide electron population inversion. The bottom n-doped cladding contains an additional far-field reduction layer (F.F.R) that broadens the transverse mode of the laser in the vertical direction, decreasing divergence of the laser as well as optical power density, allowing stable operation with a higher power. The parameters of the structure and the layer sequence are presented in Table 5.1.

Layer Type	Materials	Thicknesses μm	Dopants cm^{-3}
p-doped			Zinc
CAP layer	$GaAs$	0.1	$10^{19}÷10^{20}$
Matching	$Al_{0.05}Ga_{0.95}As$	0.12	$10^{18}÷5*10^{18}$
p-cladding	$Al_{0.32}Ga_{0.68}As$	1.7	10^{18}
p-cladding	$Al_{0.32}Ga_{0.68}As$	0.2	$5*10^{17}÷10^{18}$
active			none
Graded Index	$Al_{0.2}Ga_{0.8}As$- $Al_{0.32}Ga_{0.68}As$	0.12	-
QW	$In_{0.12}Ga_{0.88}As$	0.0044	-
Barrier	$Al_{0.2}Ga_{0.8}As$	0.009	-
QW	$In_{0.12}Ga_{0.88}As$	0.0044	-
Graded Index	$Al_{0.27}Ga_{0.73}As$-$Al_{0.2}Ga_{0.8}As$	0.07	-
n-doped			Silicon
n-cladding	$Al_{0.3}Ga_{0.7}As$- $Al_{0.27}Ga_{0.73}As$	0.03	10^{17}
n-cladding	$Al_{0.32}Ga_{0.68}As$- $Al_{0.27}Ga_{0.73}As$	0.02	$5*10^{17}÷10^{17}$
n-cladding	$Al_{0.32}Ga_{0.68}As$	0.75	$5*10^{17}$
F.F.R layer	$Al_{0.29}Ga_{0.71}As$- $Al_{0.32}Ga_{0.68}As$	0.35	$5*10^{17}$
F.F.R layer	$Al_{0.32}Ga_{0.68}As$- $Al_{0.29}Ga_{0.71}As$	0.35	$5*10^{17}$
n-cladding	$Al_{0.32}Ga_{0.68}As$	1.6	$7*10^{17}$
Matching	$Al_{0.05}Ga_{0.95}As$- $Al_{0.32}Ga_{0.68}As$	0.2	$10^{18}÷7*10^{17}$
Substrate	GaAs	645	Silicon

Table 5.1 Epitaxial layer structure of the AlGaAs-based wafer.

The optical waveguide is shaped by optical lithography and reactive ion etching with $SiCl_4$ gas. The width of the single ridge waveguide is ~2.5 µm and the depth of etching is approx. 2.1 µm ensuring single transverse mode operation. A total cavity is 2.6 mm long resulting in a 62 ps pulse round trip with a 16 GHz repetition rate in mode-locking conditions. The saturable absorber part is separated from the active medium by an etched grove and has a length of approx. ~100µm providing with the pulse duration below 1 ps. The bar consists of 20 laser devices of identical design etched one next to another. The gold contacts were evaporated on top of the devices to ensure proper voltage bias conditions. The cross-section of a single laser ridge is presented in Fig.5.2a and the combined laser bar in Fig.5.2b.

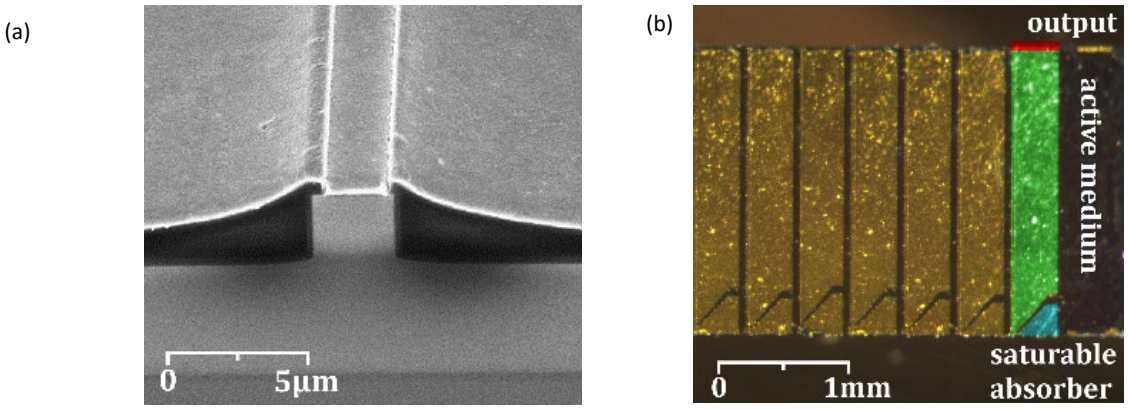

Fig. 5.2 Mode-locked semiconductor laser: (a) cross-section of the laser; (b) optical image of the laser bars

In order to make lasers operational, it was necessary to provide voltage bias, which was realized by two power supplies connected with the device via contact needles. Cooling of the bar was realized by the Peltier element removing heat to the copper radiator. An achromatic lens with a focal length of 3 mm was placed on a 3-axis translator in front of the laser output providing collimation of the beam. The schematic of technical realization is presented in Fig.5.3.

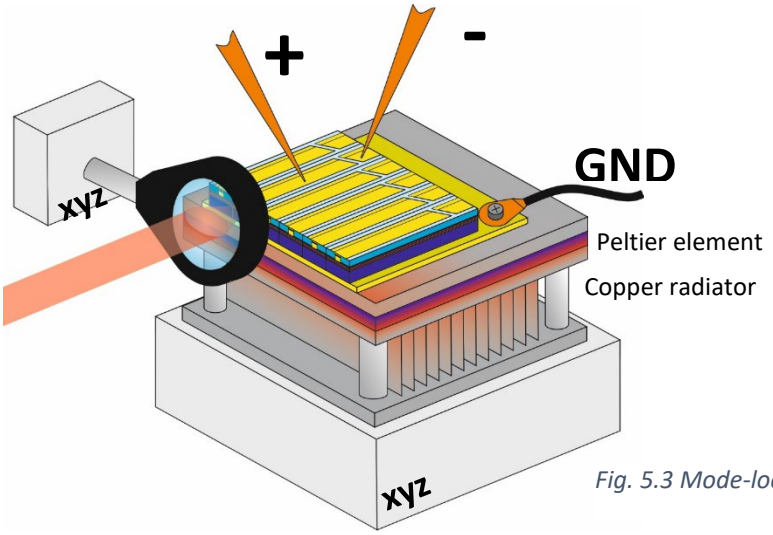

Fig. 5.3 Mode-locked semiconductor laser technical realization

Spectral characteristics for various saturable absorber bias values were measured by a fiber spectrometer AVANTES. For further measurements, 1.5 V bias was chosen to obtain stable pulsed operation and maximise the output power of the laser. For gain medium current-voltage and output power characteristics were measured by Si-diode, maximum average output power achieved in pulsed regime was 50 mW and used in further measurements. Both characteristics are presented in Fig.5.4.

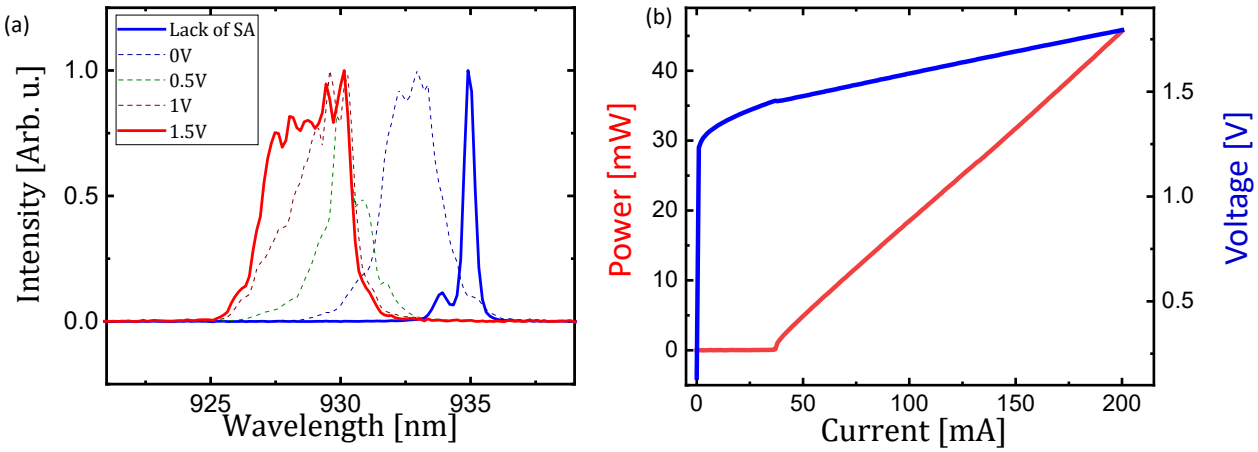

Fig. 5.4 Mode-locked semiconductor laser: (a) emission spectra of the laser for various biases applied to the absorber. (b) current-voltage and output power characteristics of the laser with zero bias on the absorber.

5.3 Excitation and detection of a coherent phonons wave packet in a metal transducer with a semiconductor laser diode.

The pump-probe experimental set-up for excitation of a coherent phonon wave packet in a form of a strain pulse and detection of its echo in Al 100nm thin film is presented in Fig.5.5. Phonons are excited via absorption of the pump laser and detected by measuring reflectivity change $\Delta R(t)$ of the surface of the transducer in a way that was described in Chapter 2. The collimated laser beam is split into pump and probe paths. The pump beam is modulated by a mechanical chopper with the frequency of 10 kHz and the probe beam is delayed by the shaker device with the time delay range of 50 ps. Both beams are focused to a spot of 5 µm by a Newport reflective microscope with 15x magnification on a transducer. The average pump power in front of the sample is 15 mW corresponding to pulse energy density equal ~5 µJ/cm^2. Probe beam average power is kept below 1 mW to avoid self-modulation. The reflected pump beam is subsequently blocked and the probe is collected by the same microscope objective and focused on the silicon photo-diode for reflectivity modulation detection $\Delta R(t)$. The signal is detected via Lock-in Amplifier with 3 ms integration time and accumulated in the time domain by oscilloscope card.

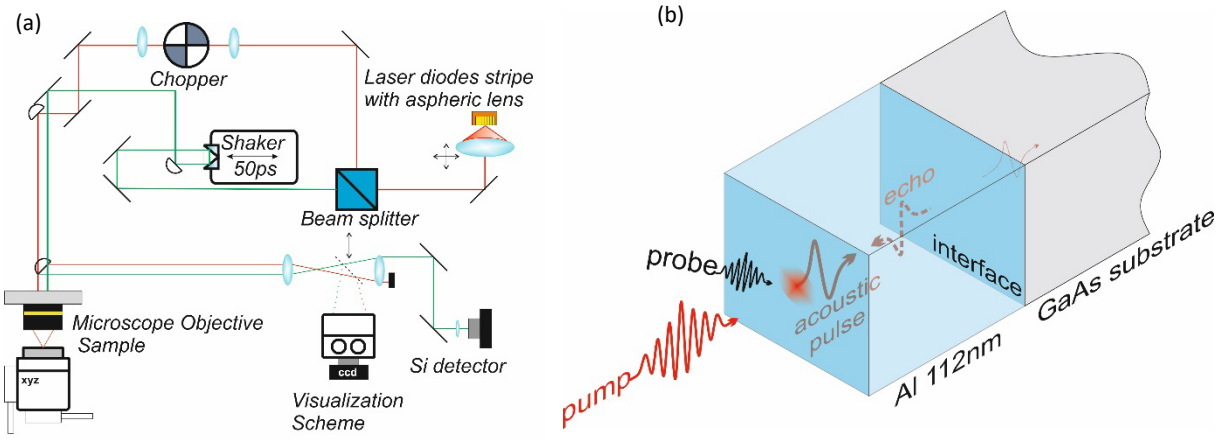

Fig. 5.5 Experimental setup for picosecond ultrasonic experiments: (a) experimental set-up; (b) scheme demonstrating the generation and detection of the echo strain pulse in the Al film.

Additionally, visualizing scheme with a microscope and movable mirror is added for precise overlap of pump and probe. The whole set-up dimensions are smaller than 80x80cm providing a significant step towards miniaturization.

Fig.5.6a shows the measured relative reflectivity signal in a function of time $\Delta R/R(t)$. At time $t = 0$, the pump pulse excites coherent phonon wave packet. A strong response observed in time up to 15 ps after

pulse arrival is typical for ultrafast pump-probe experiments and is related to the electronic response at the surface, rapid lattice heating, and stress accompanying the process. Due to the complex nature of system rapid response, it is hard to distinguish the strength of particular contributions. At the time $t = 36\ ps$ one can see the reflectivity response to the first echo of the strain pulse propagating back to the surface of the sample reflected from the interface with GaAs substrate. It corresponds with the time $t_0 = {}^{2d}/_{s} = 35$ ps of the strain round trip with the speed of sound s =6420m/s in the Aluminium sample with thickness $d = 112$ nm. The reflection ratio R of the phonon wave packet under normal incidence from the Al/GaAs interface depends on acoustic impedances of both materials $Z = \rho s$, where ρ is the density of the material.

$$R = \frac{Z_{GaAs} - Z_{Al}}{Z_{GaAs} + Z_{Al}} \tag{5.1}$$

By substituting values for Z into Eq.5.1 we obtain a reflection ratio of $R = 0.2$ with no change in the phase (no change of sign) of the reflected pulse.

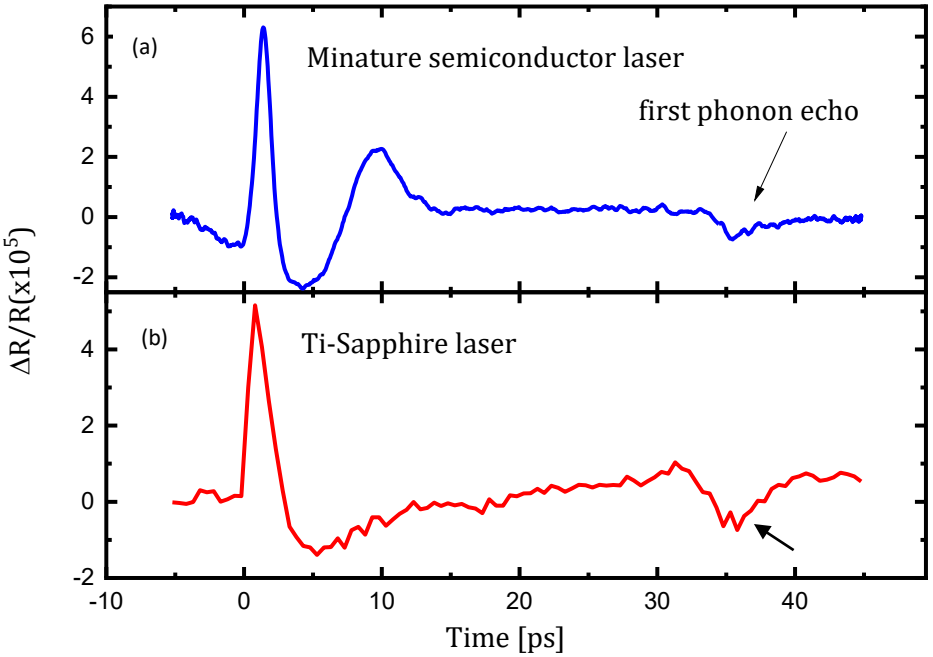

Fig. 5.6 Picosecond ultrasonic signals: (a) measured with the mode-locked semiconductor laser with repetition rate 16 GHz; (b) measured with 80 MHz commercial Ti-sapphire lasers (95).

Therefore, the amplitude of the echo should be equal to 0.2 of the amplitude of the initial pulse. It is not possible however to compare it with the initial thermo-elastic response due to the response of the hot electrons at $t = 0$. The signal obtained with a semiconductor MLLD presented in Fig.5.6a. For comparison,

the pump-probe experiment was performed on the same sample with a Ti-sapphire laser with 82 MHz repetition rate, the wavelength of 900 nm, and 150 fs pulse duration, presented in Fig.5.6b. The differences in the signal up to $t = 20$ ps are arising due to the different parameters of the pump pulse. Despite the lower excitation energy density and longer pulse duration of the MLLD pump, the characteristic features of the phonon echo signal and its time of arrival are very much comparable to the one obtained with the Ti-Sapphire laser proving that MLLD is viable alternative for generation and detection of phonons.

5.4 Outlook for further miniaturization

Our experiments show a significant step towards the miniaturization of experimental set-ups for the optical excitation and detection of high frequency collective excitations by implementing semiconductor passively mode-locked laser diode. There is room for improvement, especially since semiconductor lasers with the pulsed operation are still under development. Semiconductor lasers' high repetition rates in the GHz range are matching with frequencies discussed in this thesis phonons and magnons, moreover they have the advantage of faster signal acquisition and a better signal-to-noise ratio than conventional lasers in the MHz range. This solution however is not free from disadvantages. The system has less time to go back to equilibrium and the time window is limited by a short period between pulse arrivals. Additionally, currently achieved pulse durations are Δt~1 ps and providing with frequency limit of 1 THz and lower detection resolution than complex laser systems with pulse durations going down to Δt~50 fs. Another challenge is the time jitter of the pulsed operation and energy per pulse carried by a single pulse. These challenges push forward further development of semiconductor devices characteristics. Decreasing time jitter can be done possibly by implementing external cavity. One of the possibilities of increasing the output power of the laser lies in the application of a tapered shape of the gain medium waveguide. Tapered solution with an opening angle of a few degrees. The width of tapered output is usually an order of magnitude larger than typical ridge waveguide output, providing lower power density on the facet. This allows achieving higher output powers without the risk of catastrophic mirror damage. Another way to improve MLLD operation is the utilization of quantum dots (QD) instead of quantum wells (QW). They offer several advantages like a broad gain spectrum, a low linewidth enhancement factor, and faster dynamics with low saturation energies.

At Wurzburg University, our partners have manufactured by molecular beam epitaxy method (MBE) laser structure based on AlGaInAs quantum dots, emitting at ~920nm. The active QD were placed in a 250 nm thick graded-index heterostructure of AlGaAs (GRINSCH), and AlGaAs cladding. In Table 5.2 the structure of the device is presented. The ridge saturable absorber and tapered waveguide were achieved by electron-beam lithography and reactive ion etching. The total length of the device is 2.25mm and the absorber length ranges from 50 µm to 400 µm. In order to observe mode-locking the measurement on a microwave spectrum analyser was done. The RF signal, presented in Fig.5.7, shows a narrow line cantered at 18.045 GHz which corresponds with the length of the cavity. Maximum average power obtained with tapered laser reached 100 mW.

Layer Type	Materials			Thickness µm	Dopant
Top Cladding					Beryllium
CAP layer	GaAs			0.25	
p-cladding	$Al_{0.40}Ga_{0.60}As$			1.5	
Active Medium					none
GRINSH	GaAs/AlGaAs	SSL,	$Al_{0.18}Ga_{0.82}As$	0.25	-
Barrier	GaAs			0.003	-
SK QD 4.9ML	$Al_{0.15}Ga_{0.23}In_{0.62}As$			-	-
Barrier	GaAs			0.003	-
GRINSH	GaAs/AlGaAs	SSL,	$Al_{0.18}Ga_{0.82}As$	0.25	-
Bottom Cladding					Silicon
n-cladding	$Al_{0.40}Ga_{0.60}As$			1.5	
Substrate	GaAs			-	Silicon

Table 5.2 The epitaxial layer structure of the QD-based wafer.

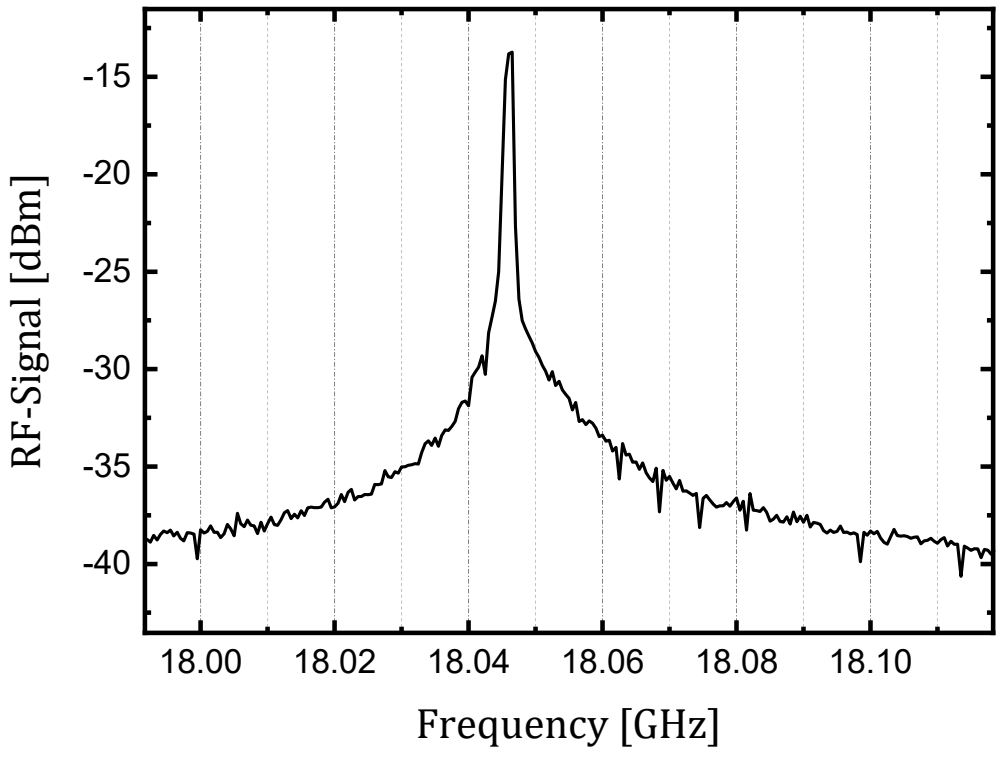

Fig. 5.7 Microwave spectrum of the mode-locked quantum dot laser.

Further miniaturization of pump-probe experiments with semiconductor lasers requires integration of the laser device with micro-optics, cooling, and electronic bias, which can be realized i.e. by butterfly laser mounts. Another bulky element of such set-up is the mechanical delay-line which can be replaced by the implementation of frequency synchronization of two lasers by Asynchronous Optical Sampling (ASOPS) (*96*) – the technique presented in Chapter 2 and used for excitation and detection of coherent magnons in Chapter 4. Frequency modulation of the signal for improved detection realized in this thesis by a mechanical chopper can be done fully electronically by modulation of laser emission and synchronized detection.

In conclusion a functional pump-probe setup based on the semiconductor mode-locked laser diodes (MLLD) was demonstrated. A table-top size of the whole scheme capable of exciting and detecting coherent phonon wave packet echo in Al film comparable with complex optical bulk Ti-sapphire laser systems was achieved. The experiments show the prospective of designing and developing portable pump probe setups integrated on a chip for various application including in-field applications.

6

Conclusions

In the scope of this thesis, I present all-optical excitation and detection of the high-frequency collective excitations, namely phonons and magnons. Measurements were performed by pump-probe experimental technique, providing time-resolved information about the dynamics of the systems under study. I also show the prospective way of miniaturization of such optical set-ups, by implementing semiconductor mode-locked laser diodes.

For excitation and detection of a propagating coherent phonon wave packet, a standard pump-probe set-up was used with a mechanical delay line to obtain the time-resolved signals. A pump pulse excites a broad spectrum of longitudinal acoustic phonons with frequencies up to 0.5 THz by ultra-fast heating of the Al transducer deposited on the back of the sample, the detailed explanation of the excitation mechanism is presented in Chapter 2. After being generated, the strain pulse propagates through the GaAs substrate and reaches the GaAs/AlAs superlattice (SL) at the front of the sample, where it gets detected by the probe pulse. In Chapter 3, a novel approach to the Time Domain Brillouin Scattering (TDBS) detection method is presented. The giant photo-elastic effect of SL exciton-polaritons is exploited for the enhancement of the TDBS signal. While probing in the transparent sample one detects only a specific part of the propagating phonons spectrum with the frequency that fulfills the Brillouin scattering selection criterion, and in our case, it is $f_B \approx 42$ GHz. In the experimental work, firstly the probe pulse with a central wavelength $\lambda_{pr} = 800$ nm and with the spectrum that fully covers the SL exciton resonance ($\hbar\omega_0 = 1.55$ eV) was used. The linear excitation and detection regime were established, which gave a control and understanding of the relationship between the signal characteristics and excitation density. Subsequently, the probe pulse spectrum was narrowed below the width of exciton resonance to extract the influence of the giant photo-elasticity of exciton-polaritons on the parameters of the signal. Varying the probe wavelength in the vicinity of the resonance provided probe energy dependent characteristics of the TDBS signal. Signals frequency f_B and decay rate τ_B^{-1} dependence followed the real and imaginary part of the complex refractive index of the exciton resonance. Amplitude A_B dependence followed the derivative of the real part of the refractive index having its maximum at the resonance which is in agreement with the theoretical model developed in cooperation with our partners. The amplitude of TDBS at the exciton-polariton resonance has a magnitude of 10^{-2} for the strain pulse amplitude $\eta_0 = 10^{-5}$. Photo-elastic parameter of exciton-polariton in our studies is three orders of magnitude higher than the parameter obtained from standard TDBS when probing away from the resonance. These results prove that giant photo-elasticity of exciton-polariton provides extremely high sensitivity to propagating phonons, which with modern detection schemes can reach the level of 'quantum sensitivity'. The number

of detected phonons N_B is determined by their spectral density around the Brillouin frequency for the particular spatial-temporal profile of a generated phonon wave packet $\eta(z,t)$. The experiments show signals which correspond to a finite number of detected phonons $N_B = 100\ \mu\mathrm{m}^{-2}$. With a slightly improved signal-to-noise ratio of the experimental set-up it is possible to detect single quanta of phonons. The discovery of the giant photo-elasticity effect in the present work paves a way for manipulating phonons on the quantum level and for widely varying applications in phononics with extremely low-density phonon fluxes.

Excitation and detection of high-frequency coherent magnons in the thin ferromagnetic films were done by means of the Asynchronous Optical Sampling pump-probe method using two synchronized Titanium sapphire lasers. The thin Galfenol film was placed in an external magnetic field at room temperature. Magnons were generated by absorption of the pump pulse which via heating of the film, changes its magnetic anisotropy, which results in a change of the effective magnetic field acting on the magnetic spin system. Due to a change of the effective magnetic field, the spins start to precess around a new direction. The coherent response of the magnetization was detected by probe pulse exploiting the Surface Magneto-Optical Kerr Effect (SMOKE), sensitive to changes in the out-of-plane magnetization component. A detailed description of these methods is given in Chapter 2. Preliminary measurements performed in our group were focused on the characterization of Galfenol thin films with thicknesses of 105 nm and 5 nm. These involved studies of Kerr Rotation (KR) signal parameters dependent on the orientation of the sample in the external magnetic field as well as on its strength. The highest amplitude of the magnetization precession is obtained for the tilt angle of $\varphi = \pi/8$ between the external magnetic field and the [1,0,0] film crystallographic direction. It is the intrinsic property of the material and it is governed by the magnetic anisotropy geometry of the sample. The frequency of the magnetization precession is proportional to the gyromagnetic parameter of the material and the strength of the external magnetic field, in the case of studied samples, it is in the GHz range. Single-shot excitation of magnetization precession in a 105 nm thick sample revealed several magnetization precession modes with various frequencies generated by heating limited to the surface of the sample, on the other hand in the 5 nm thick sample only the fundamental magnon mode was excited. It is due to the uniform heating of such sample; which thickness is below the absorption length of the material. In Chapter 4 the results of these initial measurements are presented as well as original work on resonant excitation of magnetization precession. This approach involves periodic excitation of the system before it comes back to equilibrium. The 10 GHz repetition rate laser is used and obtained signals for the external magnetic field values ranging from 0 to

500 mT. KR signals' amplitude is growing as the magnetization precession frequency dependent on the magnetic field approaches the repetition rate of the pump laser. When the frequency of the fundamental mode matches exactly the repetition rate of the laser we obtain resonant excitation of the 10 GHz uniform magnetization precession with amplitude enhanced 12 times when compared with non-resonant excitation. A similar effect is observed when the external magnetic field is tuned in the way that magnon frequency matches 20 GHz and 30 GHz which corresponds to higher harmonics of the excitation repetition rate. In a thick 105 nm sample where excitation happens only on the surface of the film, multiple modes are excited and it is not possible to address resonantly only a particular one. A periodic signal is observed but it is not harmonic and there is no significant enhancement, which is in agreement with the theoretical model of temperature modulation of the sample and its influence on the magnetic system. The concept of resonant heat transfer and its optical generation can be considered as a prospective method of magnon modulation in ferromagnetic layers deposited on commonly used semiconductors.

In Chapter 5 the first step toward miniaturization of the pump-probe optical set-up is presented by implementing a passively mode-locked laser diode MLLD with a central wavelength of 930 nm, the repetition rate of 16 GHz, 1 ps pulse duration, and above 50 mW of average power. The pump-probe set-up with a mechanical delay line was designed for the detection of a coherent phonon wave packet echo in a 112 nm Al transducer. Phonons are generated by absorption of the pump pulse heat. The pulse propagates towards the substrate, gets reflected at the interface between the transducer and the substrate, and comes back towards the surface where it was generated. There, it gets detected by the probe pulse by sensing the reflectivity change at the surface induced by the strain. The obtained time-domain signal is comparable with the signal obtained by a standard solid-state laser. It is shown that semiconductor lasers are capable of performing pump-probe experiments exploiting high-frequency collective excitations, this paves the way for the development of tabletop and out-of-lab applications.

To conclude, the thesis focuses on gaining more control over the optical generation and detection of high-frequency collective excitations which are in the spotlight of modern solid-state physics. Exploiting intrinsic properties of the materials and tailoring nanostructures allowed us to take advantage of the resonant phenomena to enhance the excitation of coherent magnons and the detection of coherent phonons. I also propose a way to bring the light source to the microscale that can lead to the implementation of these techniques in real-life applications.

Bibliography

1. C. Thomsen, J. Strait, Z. Vardeny, H. J. Maris, J. Tauc, J. J. Hauser, Coherent Phonon Generation and Detection by Picosecond Light Pulses. *Phys. Rev. Lett.* **53**, 989-992 (1984).
2. O. Matsuda, M. C. Larciprete, R. Li Voti, O. B. Wright, Fundamentals of picosecond laser ultrasonics. *Ultrasonics* **56**, 3-20 (2015).
3. T. Saito, O. Matsuda, O. B. Wright, Picosecond acoustic phonon pulse generation in nickel and chromium. *Physical Review B* **67**, (2003).
4. S. Volz, J. Ordonez-Miranda, A. Shchepetov, M. Prunnila, J. Ahopelto, T. Pezeril, G. Vaudel, V. Gusev, P. Ruello, E. M. Weig, M. Schubert, M. Hettich, M. Grossman, T. Dekorsy, F. Alzina, B. Graczykowski, E. Chavez-Angel, J. Sebastian Reparaz, M. R. Wagner, C. M. Sotomayor-Torres, S. Xiong, S. Neogi, D. Donadio, Nanophononics: state of the art and perspectives. *Eur. Phys. J. B* **89**, (2016).
5. A. G. Gurevich, G. A. Melkov, Magnetization Oscillations and Waves *CRC Press*.
6. A. V. Kimel, G. V. Astakhov, G. M. Schott, A. Kirilyuk, D. R. Yakovlev, G. Karczewski, W. Ossau, G. Schmidt, L. W. Molenkamp, T. Rasing, Picosecond Dynamics of the Photoinduced Spin Polarization in Epitaxial (Ga,Mn)As Films. *Phys. Rev. Lett.* **92**, 237203 (2004).
7. G. Ju, A. V. Nurmikko, R. F. C. Farrow, R. F. Marks, M. J. Carey, B. A. Gurney, Ultrafast optical modulation of an exchange biased ferromagnetic/antiferromagnetic bilayer. *Physical Review B* **58**, R11857-R11860 (1998).
8. J. Hohlfeld, E. Matthias, R. Knorren, K. H. Bennemann, Nonequilibrium Magnetization Dynamics of Nickel. *Phys. Rev. Lett.* **78**, 4861-4864 (1997).
9. E. Beaurepaire, J. C. Merle, A. Daunois, J. Y. Bigot, Ultrafast Spin Dynamics in Ferromagnetic Nickel. *Phys. Rev. Lett.* **76**, 4250-4253 (1996).
10. A. Kirilyuk, A. V. Kimel, T. Rasing, Ultrafast optical manipulation of magnetic order. *Rev. Mod. Phys.* **82**, 2731-2784 (2010).
11. P. M. Stolarz, V. Pusino, J. Akbar, G. Mezosi, H. Lianping, A. C. Coleman, J. H. Marsh, A. E. Kelly, M. Sorel, High-Power and Low-Noise Mode-Locking Operation of Al-Quaternary Laser Diodes. *IEEE Journal of Selected Topics in Quantum Electronics* **21**, 10-16 (2015).
12. L. Hou, M. Haji, J. H. Marsh, A. C. Bryce, 10 GHz AlGaInAs/InP 1.55 μm passively mode-locked laser with low divergence angle and timing jitter. *Opt. Express* **19**, B75-B80 (2011).
13. J. H. Marsh, L. Hou, Mode-Locked Laser Diodes and Their Monolithic Integration. *IEEE Journal of Selected Topics in Quantum Electronics* **23**, 1-11 (2017).
14. F. R. Ahmad, F. Rana, Passively Mode-Locked High-Power (210 mW) Semiconductor Lasers at 1.55-μm Wavelength. *IEEE Photonics Technology Letters* **20**, 190-192 (2008).
15. J. Shah, *Ultrafast Spectroscopy of Semiconductors* (Solid-State Sciences 115, Springer Science+Business Media, New York, 1996).
16. A. Bartels, R. Cerna, C. Kistner, A. Thoma, F. Hudert, C. Janke, T. Dekorsy, Ultrafast time-domain spectroscopy based on high-speed asynchronous optical sampling. *Rev. Sci. Instrum.* **78**, 035107 (2007).
17. F. Perez-Cota, R. J. Smith, H. M. Elsheikha, M. Clark, New insights into the mechanical properties of Acanthamoeba castellanii cysts as revealed by phonon microscopy. *Biomed Opt Express* **10**, 2399-2408 (2019).

18. M. Gerken, T. Dekorsy, N. K. Dhar, F. Hudert, R. Cerna, A. K. Dutta, M. S. Islam, H. Schäfer, C. Janke, A. Bartels, K. Köhler, S. Braun, M. Wiemer, S. Mantl, Coherent acoustic phonons in nanostructures investigated by asynchronous optical sampling. **6393**, 63930H (2006).
19. L. Antonucci, X. Solinas, A. Bonvalet, M. Joffre, Asynchronous optical sampling with arbitrary detuning between laser repetition rates. *Opt Express* **20**, 17928-17937 (2012).
20. C. Li, N. Krauss, G. Schafer, L. Ebner, O. Kliebisch, J. Schmidt, S. Winnerl, M. Hettich, T. Dekorsy, High-speed asynchronous optical sampling based on GHz Yb:KYW oscillators. *Opt Express* **25**, 9204-9212 (2017).
21. H. Zhang, B. Su, X. Yang, Y. Wu, J. He, C. Zhang, D. R. Jones, Asynchronous optical sampling data-acquisition trigger-signal derived from pulse coherence coincidence. *Rev. Sci. Instrum.* **89**, 113108 (2018).
22. C. Thomsen, H. T. Grahn, H. J. Maris, J. Tauc, Surface generation and detection of phonons by picosecond light pulses. *Phys. Rev. B* **34**, 4129-4138 (1986).
23. C. Thomsen, H. T. Grahn, H. J. Maris, J. Tauc, Picosecond interferometric technique for study of phonons in the Brillouin frequency range. *Opt. Commun.* **60**, 55-58 (1986).
24. O. B. Wright, V. E. Gusev, Ultrafast generation of acoustic waves in copper. *IEEE TRANSACTIONS ON ULTRASONICS, FERROELECTRICS, AND FREQUENCY CONTROL* **42**, 331-338 (1995).
25. G. Tas, H. J. Maris, Electron diffusion in metals studied by picosecond ultrasonics. *Phys Rev B Condens Matter* **49**, 15046-15054 (1994).
26. V. E. Gusev, P. Ruello, Advances in applications of time-domain Brillouin scattering for nanoscale imaging. *Applied Physics Reviews* **5**, 031101 (2018).
27. H. N. Lin, R. J. Stoner, H. J. Maris, J. Tauc, Phonon attenuation and velocity measurements in transparent materials by picosecond acoustic interferometry. *J. Appl. Phys.* **69**, 3816-3822 (1991).
28. V. N. Kats, T. L. Linnik, A. S. Salasyuk, A. W. Rushforth, M. Wang, P. Wadley, A. V. Akimov, S. A. Cavill, V. Holy, A. M. Kalashnikova, A. V. Scherbakov, Ultrafast changes of magnetic anisotropy driven by laser-generated coherent and noncoherent phonons in metallic films. *Physical Review B* **93**, (2016).
29. C. Baker, W. Hease, D. T. Nguyen, A. Andronico, S. Ducci, G. Leo, I. Favero, Photoelastic coupling in gallium arsenide optomechanical disk resonators. *Opt Express* **22**, 14072-14086 (2014).
30. P. Tiberto, E. Barati, M. Cinal, D. M. Edwards, A. Umerski, M. Affronte, F. Casoli, C. de Julián Fernández, G. Gubbiotti, C. Marquina, F. Pratt, M. Solzi, S. Tacchi, P. Vavassori, Calculation of Gilbert damping in ferromagnetic films. *EPJ Web of Conferences* **40**, 18003 (2013).
31. D. L. M. N. S. Almeida, Eddy currents and spin excitations in conducting ferromagnetic films *Phys Rev B Condens Matter* **53**, (1996).
32. D. E. Parkes, S. A. Cavill, A. T. Hindmarch, P. Wadley, F. McGee, C. R. Staddon, K. W. Edmonds, R. P. Campion, B. L. Gallagher, A. W. Rushforth, Non-volatile voltage control of magnetization and magnetic domain walls in magnetostrictive epitaxial thin films. *Appl. Phys. Lett.* **101**, 072402 (2012).
33. A. Enicnas-Oropesa, F. N. V. Dau, Origin of magnetic anisotropy in thin films deposited on step-bunched substrates. *Journal of Magnetism adn Magnetic Materials* **256** 301–305 (2003).
34. Y. Fan, H. B. Zhao, G. Lüpke, A. T. Hanbicki, C. H. Li, B. T. Jonker, Anisotropic exchange coupling and stress-induced uniaxial magnetic anisotropy in Fe/GaAs(001). *Physical Review B* **85**, (2012).
35. M. Kobecki, A. V. Scherbakov, T. L. Linnik, S. M. Kukhtaruk, V. E. Gusev, D. P. Pattnaik, I. A. Akimov, A. W. Rushforth, A. V. Akimov, M. Bayer, Resonant thermal energy transfer to magnons in a ferromagnetic nanolayer. *Nat Commun* **11**, 4130 (2020).
36. Z. Frait, H. MacFaden, Ferromagnetic Resonance in Metals. Frequency Dependence. *Phys. Rev.* **139**, A1173-A1181 (1965).

37. A. V. Scherbakov, A. P. Danilov, F. Godejohann, T. L. Linnik, B. A. Glavin, L. A. Shelukhin, D. P. Pattnaik, M. Wang, A. W. Rushforth, D. R. Yakovlev, A. V. Akimov, M. Bayer, Optical Excitation of Single- and Multimode Magnetization Precession in Fe-Ga Nanolayers. *Physical Review Applied* **11**, (2019).
38. M. Fähnle, Review of Ultrafast Demagnetization After Femtosecond Laser Pulses: A Complex Interaction of Light with Quantum Matter. *American Journal of Modern Physics* **7**, 68 (2018).
39. S. Pan, F. Ganss, S. Panda, G. Sellge, C. Banerjee, J. Sinha, O. Hellwig, A. Barman, Mechanism of femtosecond laser induced ultrafast demagnetization in ultrathin film magnetic multilayers. *Journal of Materials Science* **57**, 6212-6222 (2022).
40. M. Hennecke, D. Schick, T. Sidiropoulos, F. Willems, A. Heilmann, M. Bock, L. Ehrentraut, D. Engel, P. Hessing, B. Pfau, M. Schmidbauer, A. Furchner, M. Schnuerer, C. von Korff Schmising, S. Eisebitt, Ultrafast element- and depth-resolved magnetization dynamics probed by transverse magneto-optical Kerr effect spectroscopy in the soft x-ray range. *Physical Review Research* **4**, (2022).
41. Y. Chu, P. Kharel, T. Yoon, L. Frunzio, P. T. Rakich, R. J. Schoelkopf, Creation and control of multi-phonon Fock states in a bulk acoustic-wave resonator. *Nature* **563**, 666-670 (2018).
42. L. R. Sletten, B. A. Moores, J. J. Viennot, K. W. Lehnert, Resolving Phonon Fock States in a Multimode Cavity with a Double-Slit Qubit. *Phys. Rev. X* **9**, 021056 (2019).
43. G. Enzian, J. J. Price, L. Freisem, J. Nunn, J. Janousek, B. C. Buchler, P. K. Lam, M. R. Vanner, Single-Phonon Addition and Subtraction to a Mechanical Thermal State. *Phys. Rev. Lett.* **126**, 033601 (2021).
44. A. Noguchi, R. Yamazaki, Y. Tabuchi, Y. Nakamura, Qubit-Assisted Transduction for a Detection of Surface Acoustic Waves near the Quantum Limit. *Phys. Rev. Lett.* **119**, 180505 (2017).
45. J. D. Cohen, S. M. Meenehan, G. S. MacCabe, S. Groblacher, A. H. Safavi-Naeini, F. Marsili, M. D. Shaw, O. Painter, Phonon counting and intensity interferometry of a nanomechanical resonator. *Nature* **520**, 522-525 (2015).
46. A. D. O'Connell, M. Hofheinz, M. Ansmann, R. C. Bialczak, M. Lenander, E. Lucero, M. Neeley, D. Sank, H. Wang, M. Weides, J. Wenner, J. M. Martinis, A. N. Cleland, Quantum ground state and single-phonon control of a mechanical resonator. *Nature* **464**, 697-703 (2010).
47. W. Chen, Y. Lu, H. J. Maris, G. Xiao, Picosecond ultrasonic study of localized phonon surface modes in Al/Ag superlattices. *Phys. Rev. B* **50**, 14506-14515 (1994).
48. A. Huynh, N. D. Lanzillotti-Kimura, B. Jusserand, B. Perrin, A. Fainstein, M. F. Pascual-Winter, E. Peronne, A. Lemaître, Subterahertz Phonon Dynamics in Acoustic Nanocavities. *Phys. Rev. Lett.* **97**, 115502 (2006).
49. N. D. Lanzillotti-Kimura, A. Fainstein, A. Huynh, B. Perrin, B. Jusserand, A. Miard, A. Lemaître, Coherent Generation of Acoustic Phonons in an Optical Microcavity. *Phys. Rev. Lett.* **99**, 217405 (2007).
50. A. Fainstein, N. D. Lanzillotti-Kimura, B. Jusserand, B. Perrin, Strong Optical-Mechanical Coupling in a Vertical GaAs/AlAs Microcavity for Subterahertz Phonons and Near-Infrared Light. *Phys. Rev. Lett.* **110**, 037403 (2013).
51. S. Anguiano, A. E. Bruchhausen, B. Jusserand, I. Favero, F. R. Lamberti, L. Lanco, I. Sagnes, A. Lemaître, N. D. Lanzillotti-Kimura, P. Senellart, A. Fainstein, Micropillar Resonators for Optomechanics in the Extremely High 19--95-GHz Frequency Range. *Phys. Rev. Lett.* **118**, 263901 (2017).
52. M. J. A. Schuetz, E. M. Kessler, G. Giedke, L. M. K. Vandersypen, M. D. Lukin, J. I. Cirac, Universal Quantum Transducers Based on Surface Acoustic Waves. *Phys. Rev. X* **5**, (2015).
53. M. A. Lemonde, S. Meesala, A. Sipahigil, M. J. A. Schuetz, M. D. Lukin, M. Loncar, P. Rabl, Phonon Networks with Silicon-Vacancy Centers in Diamond Waveguides. *Phys. Rev. Lett.* **120**, 213603 (2018).

54. M. V. Gustafsson, T. Aref, A. F. Kockum, M. K. Ekström, G. Johansson, P. Delsing, Propagating phonons coupled to an artificial atom. *Science* **346**, 207-211 (2014).
55. B. Jusserand, A. N. Poddubny, A. V. Poshakinskiy, A. Fainstein, A. Lemaitre, Polariton Resonances for Ultrastrong Coupling Cavity Optomechanics in GaAs/AlAs Multiple Quantum Wells. *Phys. Rev. Lett.* **115**, 267402 (2015).
56. A. N. Poddubny, A. V. Poshakinskiy, B. Jusserand, A. Lemaître, Resonant Brillouin scattering of excitonic polaritons in multiple-quantum-well structures. *Physical Review B* **89**, 235313 (2014).
57. A. Bartels, T. Dekorsy, H. Kurz, K. Köhler, Coherent Zone-Folded Longitudinal Acoustic Phonons in Semiconductor Superlattices: Excitation and Detection. *Phys. Rev. Lett.* **82**, 1044-1047 (1999).
58. M. Kobecki, A. V. Scherbakov, S. M. Kukhtaruk, D. D. Yaremkevich, T. Henksmeier, A. Trapp, D. Reuter, V. E. Gusev, A. V. Akimov, M. Bayer, Giant Photoelasticity of Polaritons for Detection of Coherent Phonons in a Superlattice with Quantum Sensitivity. *Phys. Rev. Lett.* **128**, 157401 (2022).
59. I. Vurgaftman, J. R. Meyer, L. R. Ram-Mohan, Band parameters for III–V compound semiconductors and their alloys. *J. Appl. Phys.* **89**, 5815-5875 (2001).
60. M. D. Sturge, Optical Absorption of Gallium Arsenide between 0.6 and 2.75 eV. *Phys. Rev.* **127**, 768-773 (1962).
61. M. D. Dio, M. Lomascolo, A. Passaseo, C. Gerardi, C. Giannini, A. Quirini, L. Tapfer, Structural and optical studies of InxGa12xAs/GaAs multiple quantum wells. *J. Appl. Phys.* **80**, 482-489 (1996).
62. L. W. Molenkamp, R. Eppenga, G. W. t Hooft, P. Dawson, C. T. Foxon, K. J. Moore, Determination of valence-band effective-mass anisotropy in GaAs quantum wells by optical spectroscopy. *Phys Rev B Condens Matter* **38**, 4314-4317 (1988).
63. O. B. Wright, Thickness and sound velocity measurement in thin transparent films with laser picosecond acoustics. *J. Appl. Phys.* **71**, 1617-1629 (1992).
64. H. C. Casey, D. D. Sell, K. W. Wecht, Concentration dependence of the absorption coefficient forn−andp−type GaAs between 1.3 and 1.6 eV. *J. Appl. Phys.* **46**, 250-257 (1975).
65. A. Huynh, B. Perrin, N. D. Lanzillotti-Kimura, B. Jusserand, A. Fainstein, A. Lemaître, Subterahertz monochromatic acoustic wave propagation using semiconductor superlattices as transducers. *Phys. Rev. B* **78**, 233302 (2008).
66. A. V. Akimov, A. V. Scherbakov, P. J. S. v. Capel, J. I. Dijkhuis, T. Berstermann, D. R. Yakovlev, M. Bayer, Acoustic solitons in semiconductor nanostructures. *Journal of Physics: Conference Series* **92**, 012002 (2007).
67. A. V. Scherbakov, P. J. van Capel, A. V. Akimov, J. I. Dijkhuis, D. R. Yakovlev, T. Berstermann, M. Bayer, Chirping of an optical transition by an ultrafast acoustic soliton train in a semiconductor quantum well. *Phys. Rev. Lett.* **99**, 057402 (2007).
68. G. R. Hayes, J. L. Staehli, U. Oesterle, B. Deveaud, R. T. Phillips, C. Ciuti, Suppression of Exciton-Polariton Light Absorption in Multiple Quantum Well Bragg Structures. *Phys. Rev. Lett.* **83**, 2837-2840 (1999).
69. A. V. Scherbakov, M. Bombeck, J. V. Jager, A. S. Salasyuk, T. L. Linnik, V. E. Gusev, D. R. Yakovlev, A. V. Akimov, M. Bayer, Picosecond opto-acoustic interferometry and polarimetry in high-index GaAs. *Opt Express* **21**, 16473-16485 (2013).
70. F. H. Pollak, M. Cardona, Piezo-Electroreflectance in Ge, GaAs, and Si. *Phys. Rev.* **172**, 816-837 (1968).
71. T. B. Bateman, H. J. McSkimin, J. M. Whelan, Elastic Moduli of Single-Crystal Gallium Arsenide. *J. Appl. Phys.* **30**, 544-545 (1959).
72. A. V. Chumak, V. I. Vasyuchka, A. A. Serga, B. Hillebrands, Magnon spintronics. *Nat. Phys.* **11**, 453-461 (2015).
73. Y. Li, T. Polakovic, Y. L. Wang, J. Xu, S. Lendinez, Z. Zhang, J. Ding, T. Khaire, H. Saglam, R. Divan, J. Pearson, W. K. Kwok, Z. Xiao, V. Novosad, A. Hoffmann, W. Zhang, Strong Coupling between

Magnons and Microwave Photons in On-Chip Ferromagnet-Superconductor Thin-Film Devices. *Phys. Rev. Lett.* **123**, 107701 (2019).
74. M. Harder, B. M. Yao, Y. S. Gui, C. M. Hu, Coherent and dissipative cavity magnonics. *J. Appl. Phys.* **129**, 201101 (2021).
75. J. Liu, F. Feringa, B. Flebus, L. J. Cornelissen, J. C. Leutenantsmeyer, R. A. Duine, B. J. van Wees, Microwave control of thermal-magnon spin transport. *Physical Review B* **99**, (2019).
76. I. A. Golovchanskiy, N. N. Abramov, V. S. Stolyarov, M. Weides, V. V. Ryazanov, A. A. Golubov, A. V. Ustinov, M. Y. Kupriyanov, Ultrastrong photon-to-magnon coupling in multilayered heterostructures involving superconducting coherence via ferromagnetic layers. *Science Advances* **7**, eabe8638 (2021).
77. M. Van Kampen, C. Jozsa, J. T. Kohlhepp, P. LeClair, L. Lagae, W. J. De Jonge, B. Koopmans, All-optical probe of coherent spin waves. *Phys. Rev. Lett.* **88**, 227201 (2002).
78. M. Vomir, L. H. Andrade, L. Guidoni, E. Beaurepaire, J. Y. Bigot, Real space trajectory of the ultrafast magnetization dynamics in ferromagnetic metals. *Phys. Rev. Lett.* **94**, 237601 (2005).
79. J. B. Restorff, M. Wun-Fogle, K. B. Hathaway, A. E. Clark, T. A. Lograsso, G. Petculescu, Tetragonal magnetostriction and magnetoelastic coupling in Fe-Al, Fe-Ga, Fe-Ge, Fe-Si, Fe-Ga-Al, and Fe-Ga-Ge alloys. *J. Appl. Phys.* **111**, 023905 (2012).
80. A. Barman, J. Sinha, "Spin Dynamics and Damping in Ferromagnetic Thin Films and Nanostructures" (Springer International Publishing AG 2018), pp. 86.
81. B. K. Kuanr, R. E. Camley, Z. Celinski, A. McClure, Y. Idzerda, Single crystal Fe1−xGax thin films for monolithic microwave devices. *J. Appl. Phys.* **115**, 17C112 (2014).
82. A. E. Clark, M. Wun-Fogle, J. B. Restorff, K. W. Dennis, T. A. Lograsso, R. W. McCallum, Temperature dependence of the magnetic anisotropy and magnetostriction of Fe100−xGax (x=8.6, 16.6, 28.5). *J. Appl. Phys.* **97**, 10M316 (2005).
83. T. Ma, J. Gou, S. Hu, X. Liu, C. Wu, S. Ren, H. Zhao, A. Xiao, C. Jiang, X. Ren, M. Yan, Highly thermal-stable ferromagnetism by a natural composite. *Nat Commun* **8**, 13937 (2017).
84. I. Razdolski, A. Alekhin, N. Ilin, J. P. Meyburg, V. Roddatis, D. Diesing, U. Bovensiepen, A. Melnikov, Nanoscale interface confinement of ultrafast spin transfer torque driving non-uniform spin dynamics. *Nat Commun* **8**, 15007 (2017).
85. A. Melnikov, I. Razdolski, T. O. Wehling, E. T. Papaioannou, V. Roddatis, P. Fumagalli, O. Aktsipetrov, A. I. Lichtenstein, U. Bovensiepen, Ultrafast transport of laser-excited spin-polarized carriers in Au/Fe/MgO(001). *Phys. Rev. Lett.* **107**, 076601 (2011).
86. J. Kimling, G. M. Choi, J. T. Brangham, T. Matalla-Wagner, T. Huebner, T. Kuschel, F. Yang, D. G. Cahill, Picosecond Spin Seebeck Effect. *Phys. Rev. Lett.* **118**, 057201 (2017).
87. N. E. Khokhlov, P. I. Gerevenkov, L. A. Shelukhin, A. V. Azovtsev, N. A. Pertsev, M. Wang, A. W. Rushforth, A. V. Scherbakov, A. M. Kalashnikova, Optical Excitation of Propagating Magnetostatic Waves in an Epitaxial Galfenol Film by Ultrafast Magnetic Anisotropy Change. *Physical Review Applied* **12**, (2019).
88. A. Kamimaki, S. Iihama, Y. Sasaki, Y. Ando, S. Mizukami, Reciprocal excitation of propagating spin waves by a laser pulse and their reciprocal mapping in magnetic metal films. *Physical Review B* **96**, (2017).
89. S. Gupta, R. Medwal, D. Kodama, K. Kondou, Y. Otani, Y. Fukuma, Important role of magnetization precession angle measurement in inverse spin Hall effect induced by spin pumping. *Appl. Phys. Lett.* **110**, 022404 (2017).
90. M. Weiler, H. Huebl, F. S. Goerg, F. D. Czeschka, R. Gross, S. T. Goennenwein, Spin pumping with coherent elastic waves. *Phys. Rev. Lett.* **108**, 176601 (2012).

91. K. Ando, S. Takahashi, J. Ieda, Y. Kajiwara, H. Nakayama, T. Yoshino, K. Harii, Y. Fujikawa, M. Matsuo, S. Maekawa, E. Saitoh, Inverse spin-Hall effect induced by spin pumping in metallic system. *J. Appl. Phys.* **109**, 103913 (2011).
92. G. D. Fuchs, V. V. Dobrovitski, R. Hanson, A. Batra, C. D. Weis, T. Schenkel, D. D. Awschalom, Excited-state spectroscopy using single spin manipulation in diamond. *Phys. Rev. Lett.* **101**, 117601 (2008).
93. V. E. Demidov, S. Urazhdin, R. Liu, B. Divinskiy, A. Telegin, S. O. Demokritov, Excitation of coherent propagating spin waves by pure spin currents. *Nat Commun* **7**, 10446 (2016).
94. K. Van Gasse, S. Uvin, V. Moskalenko, S. Latkowski, G. Roelkens, E. Bente, B. kuyken, Recent Advances in the Photonic Integration of Mode-Locked Laser Diodes. *IEEE Photonics Technology Letters* **31**, 1870-1873 (2019).
95. M. Kobecki, G. Tandoi, E. Di Gaetano, M. Sorel, A. V. Scherbakov, T. Czerniuk, C. Schneider, M. Kamp, S. Hofling, A. V. Akimov, M. Bayer, Picosecond ultrasonics with miniaturized semiconductor lasers. *Ultrasonics* **106**, 106150 (2020).
96. A. Bartels, F. Hudert, C. Janke, T. Dekorsy, K. Köhler, Femtosecond time-resolved optical pump-probe spectroscopy at kilohertz-scan-rates over nanosecond-time-delays without mechanical delay line. *Appl. Phys. Lett.* **88**, 041117 (2006).

Acknowledgements

I would like to thank Prof. Manfred Bayer, Dr. Alexey Scherbakov, Prof. Ilya Akimov, and Prof. Andrey Akimov who were the driving force of the research conducted during my work at E2 as a Ph.D. candidate. I am grateful to Prof. Vitalii Gusev, Dr. Serhii Kukhtaruk, and Dr. Tetiana Linnik, without whom, an understanding and accurate description of observed physical phenomena would be impossible. I would also like to thank the groups of Prof. Andrew Rushforth, Prof. Sven Hofling, Prof. Mark Sorel, and Prof. Dirk Reuter for preparing excellent samples. Finally, I am thankful to my family and friends for their everlasting support. I would like to dedicate this work to my daughter Anna and her mother Ola.

Scientific Contributions

Publications:

M. Kobecki, G. Tandoi, E. Di Gaetano, M. Sorel, A. V. Scherbakov, T. Czerniuk, C. Schneider, M. Kamp, S. Hofling, A. V. Akimov, M. Bayer, Picosecond ultrasonics with miniaturized semiconductor lasers. *Ultrasonics* **106**, 106150 (2020).

M. Kobecki, A. V. Scherbakov, T. L. Linnik, S. M. Kukhtaruk, V. E. Gusev, D. P. Pattnaik, I. A. Akimov, A. W. Rushforth, A. V. Akimov, M. Bayer, Resonant thermal energy transfer to magnons in a ferromagnetic nanolayer. *Nat Commun* **11**, 4130 (2020).

M. Kobecki, A. V. Scherbakov, S. M. Kukhtaruk, D. D. Yaremkevich, T. Henksmeier, A. Trapp, D. Reuter, V. E. Gusev, A. V. Akimov, M. Bayer, Giant Photoelasticity of Polaritons for Detection of Coherent Phonons in a Superlattice with Quantum Sensitivity. *Phys. Rev. Lett.* **128**, 157401 (2022).

Talks and Conferences:

7th Son Et Lumiere school 2019 in Les Houches, France: Poster: 'Generation and detection of strain pulses with passively mode-locked semiconductor laser diode'

4th Ultrafast Magnetism Conference 2019 in York, UK: Poster: 'Resonant optical driving of magnetization precession in metal ferromagnetic nanolayers'

OPON2020 Workshop in Warsaw, Poland: Oral presentation: 'Miniaturized lasers for picosecond ultrasonics'

ICPPP21 Conference in Bled, Slovenia: Oral presentation: 'Giant photoelasticity of the superlattice polaritons for laser ultrasonics'

Transregional Collaborative Research Center TRR 142 'Kick-off' Workshop : Oral presentation: 'Giant photo-elasticity of exciton-polaritons in a short-period GaAs/AlAs superlattice
for detection of coherent phonons'

Jaszowiec Conference 2019: Poster 'Generation and Detection of Strain Pulses with Passively Mode Locked Semiconductor Laser Diode.'

List of Figures